Investigation of Photovoltaic Device Operation under Varying Spectral Conditions

by

Thomas R. Betts

Doctoral Thesis

Submitted in partial fulfilment of the requirements

for the award of

Doctor of Philosophy of Loughborough University

September 2004

Abstract

A unique system for the synchronous measurement of photovoltaic module electrical parameters and solar spectral irradiance is described. Data quality control is addressed in depth and the practices followed to ensure integrity for the ensuing analysis are explained.

Irradiance spectra have been characterised with a single-number descriptor, the average photon energy. Unlike previous spectral characterisation work, the figure employed here is independent of artificially imposed references, such as the spectral response of a solar cell. This has allowed it to be used in a full analysis of spectral variation in the UK, with comparison made to a second site of significantly different climate.

This simple characterisation has also allowed spectral irradiance measurements to be included for the first time in a thorough investigation of the effects of different environmental factors on photovoltaic device performance in real operating conditions. Discussion is entered on each of the main influences on key device parameters and concludes with a quantification of the principal effects on electrical energy generation.

The development of an enhanced spectral irradiance model is described, which can simulate solar spectra under non-ideal weather conditions, as experienced by many locations. In validation against measured data, it is proved a convenient solution to the problem of poor availability of spectral irradiance data for use in photovoltaic performance modelling.

The inclusion of spectral effects into photovoltaic device modelling is undertaken and shown to significantly improve existing modelling approaches. Finally, improvements are identified and suggestions made to further the work.

Acknowledgements

I would like to recognise the contribution made to this work by Chris Jardine of ECI, who first suggested using the average photon energy for spectral characterisation and with whom I had many useful discussions on outdoor measurements.

My appreciation also goes to Chris Gueymard for our discussions of spectral irradiance measurement and modelling and support with using his excellent SMARTS code.

The construction of the outdoor measurement system would not have been completed without all the diligent wiring work of Axel Mueller and Tobias Helf. Thanks also to Daniela Sauter, for her contribution to the database management tools.

I am very grateful for the repeated support offered by Steve Ransome of BP Solar in my applications for travel grants, allowing me several opportunities to attend major conferences.

Also my appreciation to Professor Yamaguchi and the members of his laboratory at TTI for welcoming me to join them for a research visit and in particular Ned, who contributed a great deal of moral support during the writing-up of this thesis.

A large thank you goes to my official supervisor, David Infield and all the staff, students and visitors to CREST, who have made it a stimulating, rewarding and supportive workplace over the course of my studies. This applies especially to Ralph Gottschalg, who has demonstrated an inspiring managerial philosophy throughout and even claimed to have enjoyed proofreading my thesis.

Finally, I thank my partner May for her encouragement and for looking after me during the final stages of writing, my parents for their unquestioning support and my sister for showing me it was possible, giving me a wealth of advice and keeping me calm.

Contents

1 Introduction

There are currently two principal quantities in use to characterise the output of photovoltaic systems. The first is the power rating, given by the efficiency of the PV modules and the total area of these used in the system. The second is the energy yield, the actual electrical energy generated by the system in a given period of time. While PV modules are priced on the basis of their power rating, electricity consumers and suppliers buy and sell in units of energy. These are linked by the performance ratio, the ratio of actual energy yield to the theoretical generation based on the power rating and incident solar irradiation. The performance ratio is never unity, arising from that fact that the efficiency of any PV device is not a constant.

The efficiency of a device is strongly dependent upon the operating conditions under which it is evaluated. This has been understood for a long time and led to the standardisation of conditions for reporting laboratory-measured cell efficiencies, Standard Test Conditions (STC)[†]. This set of conditions provides common benchmarking for PV devices and is not only a research tool, but it is also the STC efficiency that is used to set the price of commercial modules in the marketplace.

However, most installed PV systems will rarely encounter conditions close to this standard. The STC irradiance is close to the maximum of that experienced in realistic operation, which instead varies with daily, annual and weather-based patterns. When it is encountered, it provides a heat source that raises the module temperature to well over the STC value. With the exception of tracking systems, the solar angle of incidence naturally changes on a daily and annual basis and is rarely normal to the plane of array. The irradiance spectrum also varies with solar position, as bulk attenuation in the atmosphere is highly wavelength-dependent and the path length changes with solar elevation. There is an additional dependence on the weather as cloud cover acts to further skew the spectrum. The extent of variation in realistic operating conditions and how far removed they are from STC is specific to the system location, but the data of Table 1.1 gives an idea of how rarely STC are met in a genuine operating environment.

[†] Standard Test Conditions: device temperature 25˚C, irradiance 1000Wm^{-2}, spectrum ISO9845-1 (air mass 1.5 global), normal incidence.

Condition	Percentage of Time Satisfied
Module Temperature (25 ±2) ºC	8.8%
Irradiance (1000 ±50) Wm^{-2}	2.9%
Spectrum AM1.5G ±0.1 eV	1.2%
Temperature AND Irradiance	0.1%
Temperature AND Irradiance AND Spectrum	0.0%

Table 1.1: Disparity between Standard Test Conditions and outdoor conditions at Loughborough

The sensitivity of different PV device electrical parameters to the various environmental influences of these conditions depends on the technology (device material and structure) and the production quality. The key property of a PV material regarding photocurrent generation is the spectral response (SR_λ), related to the external quantum efficiency (QE_λ) through:

$$SR_\lambda = \frac{q\lambda}{hc} \times QE_\lambda \tag{1.1}$$

where h, c, q and λ are Planck's constant, the speed of light in a vacuum, the electronic charge and the wavelength of incident light, respectively. The external quantum efficiency is a function of wavelength and is defined as the probability that a photon of energy hc/λ will be converted to supply an electron to the cell terminal.

The spectral response is determined by the band gap, cell thickness and transport in the material. The degree to which the spectral response and the incident irradiance spectrum coincide varies as the spectrum changes and gives rise to a spectral effect on the device current and efficiency.

Advanced multi-junction device structures, with stacks of series-connected junctions one atop the other, present a complex combination of the spectral response of each sub-cell, leading to some interesting additional spectral effects for such technologies. The series connection imposes a limitation on the total current output of the device, which is held down close to that of the weakest generating sub-cell. As the spectrum of incident light changes, the current generation of each sub-cell varies leading to changes in which

one acts as the limiter. The result is effectively a non-constant spectral response, one which is difficult to optimise for operation in realistic outdoor conditions.

Improved understanding of how the operating environment affects the efficiency of a PV system is important for two main reasons. The first is that the efficiency achieved under different conditions over a set period of time determines the energy yield of the system for that period. Over longer periods (annual), this severely influences the economics of grid-connected systems. Over shorter timescales (monthly), this determines the energy storage requirements and costs for stand-alone systems. The second is that a full understanding of device performance over a range of conditions offers the opportunity to improve device design by optimisation for energy generation. A proposed change from power rating to a combined power and energy rating standard for PV modules will create the incentive for manufacturers to follow this course as pricing mechanisms change.

The principal difficulty of attaining this understanding of PV response to different environmental influences is the separation of the various effects, as the influences tend to be correlated with one another. Also, there are only rare outdoor measurement sets which include spectral irradiance information, hence this influence in particular is not well understood.

This thesis presents the first long-term analysis of PV device outdoor performance with concurrent spectral irradiance measurements. As such, the opportunity is taken to focus on the spectral effect, which is assessed for four different PV technologies using measurements of real modules in operation.

The tools used for data collection and description are introduced in chapter 2. Firstly, the development work and realisation of the upgraded outdoor PV measurement system at the Centre for Renewable Energy Technology (CREST) is presented. Data storage and quality control are critical issues for outdoor testing and the methods employed regarding these aspects are also discussed in this chapter. With regard to PV performance, a major obstacle to study of the spectrum has been lack of a simple descriptive parameterisation. A single-value solution is suggested here and its use demonstrated in an analysis of the spectral environment of the UK.

An investigation of the different environmental effects on selected modules is undertaken in chapter 3. A discussion of published methods for carrying out such work precedes a detailed analysis of the CREST measurement data. The influence of each environmental factor on the electrical parameters of the different modules is assessed and the relative impacts evaluated. Finally, a calculation is made of the spectral effect on the annual energy yield of each module operating in Loughborough.

The general lack of measured spectral irradiance data has led to the development of various atmospheric transmission models. In chapter 4, one of these models intended for use in clear-sky conditions has been extended empirically to include cloud effects. A description of the existing models, the new development work and performance testing against spectral measurements are given.

Chapter 5 draws on the analysis and spectral irradiance modelling work to present two approaches for modelling the spectral effect on PV device performance. One method requires detailed information about the modules being simulated, but potentially offers high accuracy. The other is an empirical approach requiring full characterisation of a module at one site, before being generally applicable to the module installed at any location. A simplified spectral model is applied with the latter method.

Finally, conclusions and recommendations on different aspects of spectral irradiance influence on PV device performance draw the thesis to a close.

2 Outdoor Measurement of Spectral Irradiance and Photovoltaic Devices

While monitoring equipment for installed PV systems may be described as standardised, such systems generally log only a few parameters for the benefit of the installer or consumer. These parameters are typically d.c. and a.c. energy and operating voltages. Outdoor systems for PV research, measuring full current-voltage characteristics, module temperatures and meteorological parameters may contain off-the-shelf components, but cost usually imposes a condition whereby the system as a whole is custom built.

This is the case at CREST, so this opening chapter introduces the measurement system used in the course of this work, with a description of the hardware and control software, largely developed by the author to improve the existing system. Data availability and processing are fundamental to analysis of long-term datasets and these are discussed in the mid-section, including an appraisal of the error sources associated with the outdoor system. This is followed by a discussion of spectral irradiance variation, starting with the options for a characterisation methodology before the presentation of an analysis of the spectral irradiance measurements taken for this work.

2.1 Outdoor Measurement System

The CREST rooftop-mounted PV module monitoring system was originally commissioned in May 1998 [1]. In September 2002 the system was upgraded substantially, with the test module capacity increased from 20 to 50 channels, recalibration for all instruments and development of improved control/logging software. The author's principal contribution was in calibration, software development and installation of the new system components.

Figure 2.1: Rooftop elements of the CREST outdoor measurement system

The system comprises three parts: a microprocessor-controlled multiplexing unit on the roof (behind the modules in Figure 2.1), to which up to 50 PV test devices are connected; a mini meteorology station of two pyranometers and an air temperature sensor (foreground); and a spectroradiometer (bottom right).

Each input to the multiplexer is fed sequentially to a Keithley 2420 source-measure unit housed inside the laboratory. This is used to measure full current-voltage (I-V) traces and to perform the resistance measurement for the PT100 sensors monitoring the back temperature of each test module. The Keithley unit is connected for control and data transfer to a PC via an IEEE 488 bus. The PC also houses an Advantech PCL813B multi channel analogue-to-digital converter (ADC) board, which is used for sampling the meteorological data. Signals from two Kipp & Zonen CM11 thermopile pyranometers, one mounted in the horizontal and one in plane-of-array, and a radiation-shielded PT100 air temperature sensor are boosted and conditioned electronically on the

roof before read-in on the ADC board. Finally, the spectroradiometer is connected to the PC through a COM port. The spectroradiometer is a scanning monochromator type with a silicon detector to measure solar spectral irradiance from 300-1040nm and a second, indium-gallium-arsenide (InGaAs) detector to extend the range to 1700nm. Measurements are taken in 10nm steps, requiring 141 individual samples per scan. Combined with the detector switchover and scan speed, this leads to a complete spectrum measurement time of approximately 2 minutes, giving rise to measurement stability issues which are addressed in the following section.

Data collection is managed by in-house software running on the PC. The environmental (meteorological) data are sampled and logged every 10 seconds, the spectral irradiance, I-V curves and module temperatures are measured every 10 minutes, with measurements of each module temporally bracketed by additional thermopile readings, to assess stability of the conditions. The spectroradiometer runs on its own software resident on the same PC, hence the spectral irradiance data are intercepted by the central system control application before all of the data is compressed and added to storage. A schematic of the complete system is shown in Figure 2.2.

Additional meteorological inputs, not yet measured at CREST, are required for some of the modelling approaches covered in later chapters of this thesis. In these cases, data from the Loughborough University Meteorological Station (LUMetS) are used [2]. This is a fully instrumented station, meeting all the requirements of the UK Met Office network, with the exception of high-level windspeed measurement, not relevant for this work. Its campus location is less than 500m from the CREST outdoor test rig and such spatial displacement is not of great concern for the parameters in question (air pressure and relative humidity as hourly averages). The LUMetS horizontal irradiance and air temperature readings are correlated with those at CREST to ensure synchronicity between the two sites.

Data from both systems are stored in a common database (Borland Interbase), which also acts as the core of the data analysis work. The compressed measurement data files are transferred manually between machines. Although the logging machine is networked and this process could be automated, it has proved useful to have an element of human interaction which allows a first-hand check of the state of system operation and early identification of problems.

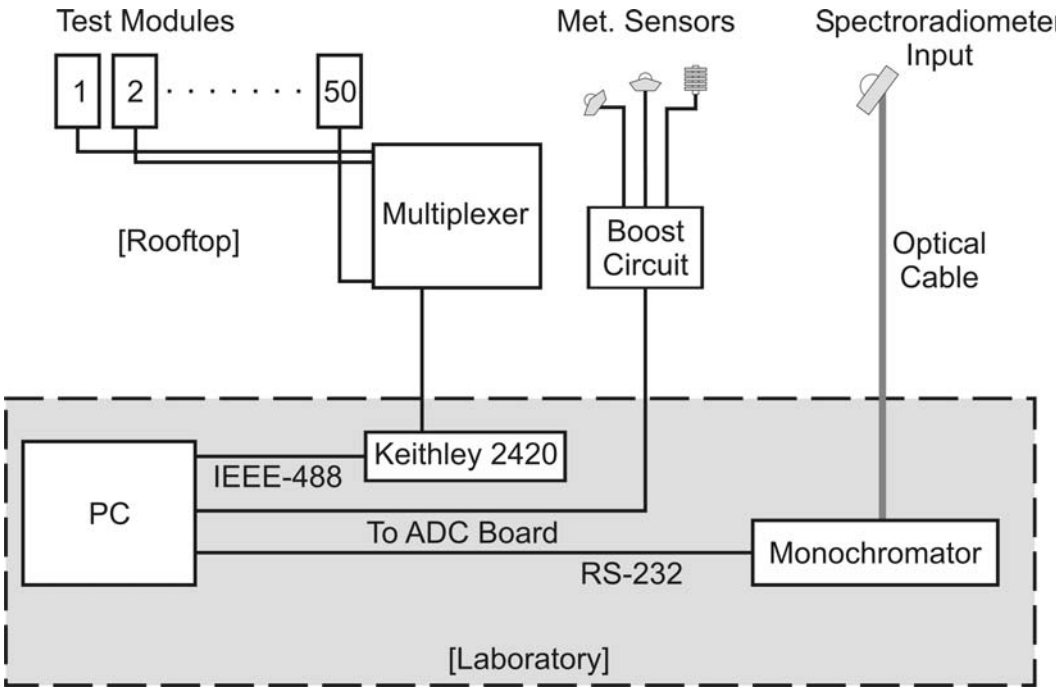

Figure 2.2: Schematic of the CREST PV module outdoor testing arrangement

2.2 Data Processing

2.2.1 Data Availability

As with any logging system, that running at CREST has suffered from the occasional failure, leading to loss of data availability. However, this does not necessarily result in a total data loss: since each of the monochromator, multiplexer, and meteorological instrumentation has its own power supply, it is unusual for all elements to fail simultaneously, bar total power outage or a problem with the control PC.

However, analysis of the influence of the spectrum on the test modules requires concurrent spectral irradiance and device data as an absolute minimum. The latter must incorporate the measurements of device temperature since this also induces performance effects, which need to be isolated to accurately gauge those due to the spectrum. Ideally, there should be a matching set of data from the thermopiles, which supplies information on the stability of the weather conditions and hence the I-V and spectrum measurements, which take a finite time to perform. Figure 2.3 summarises the data availability over the lifetime of the CREST outdoor system.

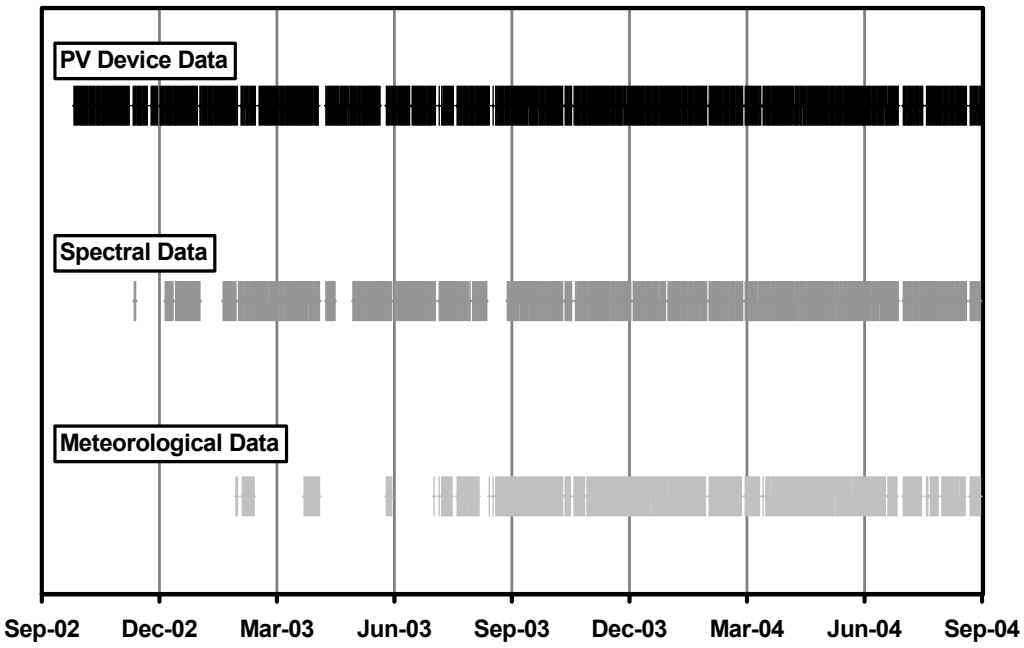

Figure 2.3: Plot of long-term data continuity

2.2.2 Data Quality

Having established the data availability for the given application, there are yet several deleterious influences to consider, which act to reduce the quality of the recorded data set. These correspond to non-fatal faults in the measurement system and situations exceeding the design limitations of the system.

The faults experienced have been largely due to erosion of the operational integrity of the individual system components (such as electrical faults in signal wiring and calibration drift of instruments) and timing mismatch errors, where it has often been ambiguous whether or not the data file timestamps have been adjusted for local daylight saving and other problems relating to the system clock. These have arisen from: the fact the logging PC is networked, so falls partially under the control of the university IT administration; the inclusion of older CREST data and LUMetS data, measured on other stations with unknown timing set-ups; and the necessary use of certain control applications (such as for the spectroradiometer), which are not open source and hence lack some flexibility. These problems have been tackled through comparative tests of file creation and modification timestamps and parsing of the data filenames (which include date-time information).

The primary issues concerning the limitations of the system are also problems of timing. With the 2 minutes needed to scan the spectrum, a significant proportion of spectral measurements are corrupted by significantly changing levels of global irradiance during acquisition. Such changes are not recognised by the monochromator, which will continue to measure regardless, resulting in a measurement file that, to the system, appears to be sound. In addition, since the PV modules are tested sequentially, the electrical measurements are not necessarily simultaneous with the spectrum measurement. Some channels are still being measured even after the spectroradiometer scan has been completed, necessitating further checks on the stability of conditions between the two events.

Missing, fallacious, or otherwise flawed data clearly need to be excluded from consideration in the analysis routines to avoid misleading results. Identification of these bad data is not straightforward, since there is such a range of reasonable values expected, depending on the environmental conditions and material properties of specific devices.

Various tests have been developed and are applied as the recorded data are taken from the measurement PC for addition to the database. The simplest of these tests relate to the single-value measured parameters with well defined ranges such as the irradiance measured with the thermopile pyranometers, the air temperature, the PV module temperature, short-circuit current and open-circuit voltage. In these cases, values can be ruled out on the basis of a priori physical knowledge, for example that irradiance values recorded greater than the top-of-atmosphere solar constant are clearly incorrect. The criteria used for these tests have been selected to exclude extreme, unphysical values while retaining those in the boundaries where there can be no clear judgement. The aim of this approach is to preserve as large a dataset as possible for analysis, but ensuring the results are not excessively skewed by outliers. The criteria for the single-valued parameters are summarised in Table 2.1.

Parameter	Lowest Accepted Value	Highest Accepted Value
Thermopile Irradiance (10s data)	0 Wm^{-2}	1300 Wm^{-2}
Air Temperature (Loughborough)	-20˚C	50˚C
Irradiance (taken with I-V data)	0 Wm^{-2}	1300 Wm^{-2}
Module Temperature	-20˚C	100˚C

Table 2.1: Exclusion criteria used in simple data quality checks

The more complex data require a more involved approach. For instance, each measurement of the spectrum yields an array of 141 individual narrowband irradiance measurements. Integrating the spectrum for a broadband irradiance and applying simple filters as above is not enough since it does not test the stability of the radiation environment during acquisition. Instead, three tests have been specifically designed for automated quality assessment of the spectral irradiance measurements.

The first looks at the measurement points bracketing the detector switchover from 1040nm to 1050nm. During the switchover, the shutter is closed, the grating position is reset and other components shifted to redirect the beam, and the gain is zeroed for the InGaAs detector before the shutter reopens. The complete procedure takes 30 seconds and is the longest pause in the acquisition. This region of the spectrum is also flat, making it possible to use the difference between these two measurements as a stability check. Ideally, this sort of check would be carried out continuously over the spectrum. However the many sharp absorption bands do not allow the extension of this discontinuity identification approach.

The second test is a development of the discontinuity method. Although the natural variation by wavelength is often very rapid, the spectrum can be divided into bands of a few hundred nm and the raw data within them averaged, effectively resulting in a very coarse version of the original measured spectrum. A few wide bands have thus been identified and their relative magnitudes quantified over a range of conditions to determine a rough characteristic shape. It is then possible to automate the band averaging and correlation to the identified shape within set tolerances to yield the "shape filter".

The third test uses the set of 10-second pyranometer measurements of global irradiance that correspond to the 2-minute scan time of each complete spectrum measurement to assess the stability of the conditions during the acquisition. By comparing sequential pyranometer measurements, it is possible to determine not only whether the irradiance was stable over the whole spectrum scan, but if not then also the time at which a change occurred (to the nearest 10 seconds). Given the observed progress through wavelengths vs. time shown in Figure 2.4, it is then known up to which wavelength the measurement is good for. This can be used to retain the maximum amount of data for the analyses where information on the total spectrum is not required (e.g. the spectral response-based modelling of short circuit current presented in the following chapters).

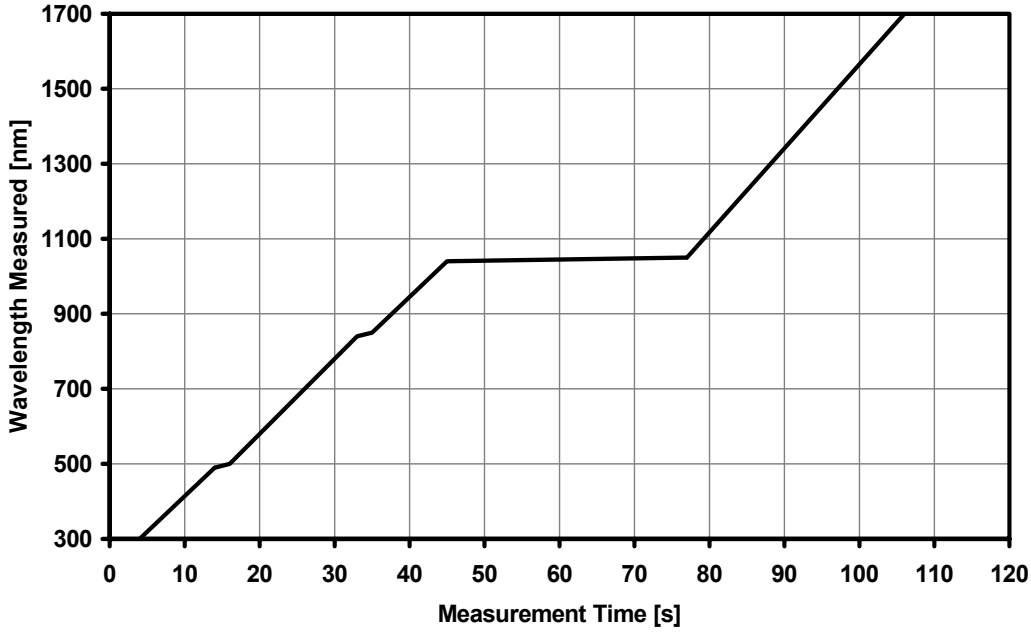

Figure 2.4: Plot of measured wavelength vs. time during spectrum acquisition

The switchover discontinuity filter is robust and the simplest of the three, yet gives only a limited amount of information. The shape filter performs well in the majority of cases, yet the sheer variety in naturally occurring spectra leaves it fallible. This is due to the optimisation of the tolerance boundaries – too strict and many good quality measurements will be discarded, too relaxed and the filter starts to pass erroneous data. The pyranometer-linked filter has proved the most useful and robust and is the preferred method. The major weakness is the requirement of having a concurrent set of environmental data. It can be seen from Figure 2.3 that this is not always so, hence all three filters are applied in practice.

It should be noted that no measured data are actually deleted or excluded from the database during any of the filtering processes. Rather, specially defined fields in the database tables are updated with a marker code for the quality of each dataset. Some of these markers convey simply whether the dataset has passed or failed a particular test, others relate to a confidence or quality level in the case of the more complicated tests. The decision on which data to exclude is made at the analysis stage and depends on the requirements for a particular analysis.

2.2.3 Error Analysis

This section presents the analysis of error sources in the CREST and LUMetS measurement systems and their propagation as far as storage in the database, on which all the analysis for this thesis is based. Propagation through further manipulation for specific analysis and modelling tasks is presented in the relevant chapters and will refer back to this section as the starting point.

Environmental Data

The global irradiance and the hemispherical irradiance falling on the plane-of-array (PoA) at CREST are each measured with a Kipp & Zonen CM11 thermopile pyranometer. One of the pyranometers (by rotation) is sent every two years to be calibrated by the manufacturer against a standard, itself calibrated at the World Radiation Centre in Switzerland. The remaining pyranometer is calibrated against the one sent off, on its return to CREST. The instruments are manually cleaned on an irregular basis, as and when research personnel venture onto the roof; in between, there is sufficient rain to adequately control build-up of dirt on the glass domes. The CM11 model is of ISO9060 secondary standard class: the response time (12s), linearity (±0.6%) and minimal thermal (±1%) and acceptance angle (<±3% at 80°) effects lead to a declared accuracy for hourly irradiance measurements of 3%.

The thermopiles give a very low voltage output (sensitivity ~5μV/Wm^{-2}) so are fed directly to a booster unit in a weatherproof casing on the roof. The boost circuits provide gain yielding an output of 0-5V (corresponding to 0-1400Wm^{-2}) through an industrial amplifier. The short cable runs and large input impedance of the amplifier (>$10^{10}\Omega$) lead to negligible signal corruption. The amplifier input has a maximum offset

error of ±250μV (±50Wm^{-2}) at 25˚C with an additional ±3μV/˚C (±0.6Wm^{-2}/˚C). The gain is accurate to ±0.5% (±5Wm^{-2} at 1000Wm^{-2}) at 25˚C with an additional ±100ppm/˚C (±0.1Wm^{-2}/˚C at 1000Wm^{-2}).

When the thermopiles are calibrated, the boost box is also brought down to the lab for calibration on site. This entails supplying test input voltages sourced from a Keithley SMU (capable of μV output) and measuring the amplified output with a digital multimeter. Inputs covering the full range of operation are applied to check linearity and correct any gain or offset drift.

The boosted signals are brought down from the roof via approximately 10m of cabling and connected to an analogue-to-digital converter (ADC) board in the system control PC. The resistance of the cabling is calculated as:

$$R_{cable} = \frac{\rho L}{A} \tag{2.1}$$

ρ is the resistivity of copper (taken as 1.75x10^{-8}Ωm at 30˚C), L is the cable length (10m) and A is the cross-sectional area of the cable (2.2mm^2), yielding a cable resistance of 0.8Ω. The high input impedance of the ADC ensures low currents (μA) and hence voltage drop on the cable is neglected.

The ADC is 12-bit, giving 4096 recognised input levels. For the 0-5V range, this gives a resolution of 1.22mV or 0.35Wm^{-2}.

During acquisition, each signal is sampled continuously for 500ms and averaged to minimise noise. Measurements are taken every 10s, the same order as the CM11 response time: hence during periods of high frequency of passing clouds the error of an individual pyranometer measurement is likely to exceed the stated hourly value. However, the raw data is not used directly in any analysis, but always averaged into periods of at least 10min. Given the number of raw measurements in each 10min value, the 3% figure for error in the pyranometer remains plausible. The largest source of error in the system is the offset on the boost input, which is subsequently magnified. Since it is not known how this varies over time, all pyranometer data undergo an offset correction based on the average zero offset of the nighttime measurements of the 24-

hour period in question. This effectively levels the input offset error at the average nighttime temperature for each day's measurements. This leaves a temperature-dependent offset error of the order $6Wm^{-2}$ (based on a daytime-nighttime air temperature difference of typically 10˚C). Combining this with the pyranometer and gain errors and neglecting those due to cable losses and ADC rounding error yields an overall maximum error less than ±5% for measurements exceeding $500Wm^{-2}$, rising to ±10% at $100Wm^{-2}$.

The PT100 sensor measuring ambient air temperature is a Vector Instruments T351-PX of accuracy ±(0.3˚C at 0˚C + 0.005˚C/˚C). A radiation shield limits heating due to direct solar irradiation to $2.3˚C/kWm^{-2}$ in still air. The drive circuit for the sensor is housed in the boost box and supplies a current stable to ±2%. The resulting terminal voltage range of 0-5V corresponds to the full measurement scale of –50 to +70˚C. Measured on the 12-bit ADC board, this gives a resolution of 0.03˚C. This channel is also measured continuously for 500ms and averaged to counteract noise. The 10s measurement frequency is overkill considering the rate-of-change of the air temperature, but is bundled with the pyranometer measurements for convenience. Since the sensor is mounted on the north side of the pyranometer mast it receives only low levels of direct solar radiation, yielding an overall maximum error <±2˚C over the range –15˚C to +35˚C.

The Loughborough University Meteorological Station (LUMetS) is a fully integrated system with a Campbell Scientific CR10X data logger at its core. Of the data collected, the work in this thesis makes use of the ambient air temperature, measured with a Campbell Scientific Type 107 thermistor (accurate to ±0.3˚C), surface pressure (Vaisala PTB101B, ±1.5mB), relative humidity (Campbell Scientific 50Y Probe, ±3% at 90%RH, ±6% for >90%RH) and global irradiance (Middleton EP109 pyranometer, ±3%). The data logger itself has a maximum error of ±0.5% on the analogue inputs. All data is sampled on a 10s basis and logged as hourly averages.

Spectral Data

The only elements of the spectroradiometer system on the rooftop are the integrating sphere and covering dome. The integrating sphere is specifically designed to accept radiation over 2π steradian and features an almost ideal cosine response. Since the system is calibrated in situ, optical losses in the cable and monochromator (Instruments

S.A. 270M) are accounted for. Losses related to degradation between calibrations are negligible. The calibration itself requires the erection of a light-tight enclosure on the roof, over the integrating sphere input. A secondary standard Tungsten-Halogen reference lamp (maintained by the supplier) is set up to a particular geometry in relation to the aperture, switched on and allowed to stabilise. Scans of the lamp spectrum are taken and a new calibration file is cast as necessary. At the inception of the current outdoor measurement system the monochromator underwent a service with the supplier (to check internal motors, cleanliness of the optics, etc.) before calibration. The calibration errors are wavelength-dependent and are summarised in Figure 2.5:

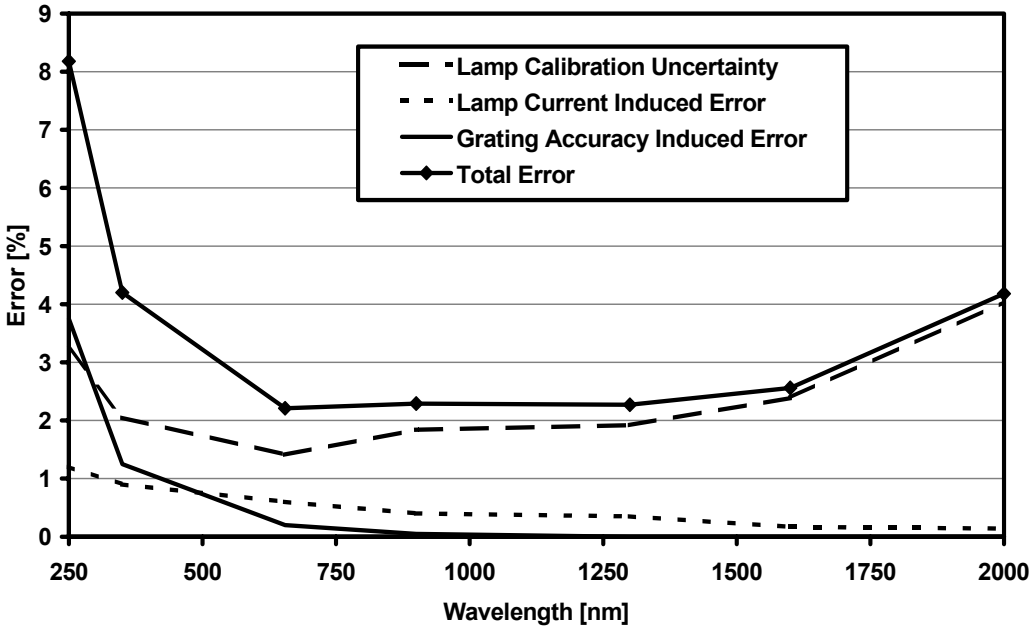

Figure 2.5: Calibration error in the spectroradiometer

Additional error in the measurement of the complete spectrum arises from changing sky conditions over the scan time: where this is excessive the data is marked as a bad set during the database filtering, but there is a tolerance for 5% irradiance variation as measured by the in-plane thermopile. Such variation acts to skew the measured spectrum, but since a change in either direction is as likely and spectra are rarely used on an individual basis, this error is reduced by the large quantity of data used in analysis.

Device Data

The I-V measurements of each module are taken by programming the Keithley SMU to sweep through set points in voltage source mode, from slightly reverse bias to slightly exceeding V_{OC}. The stated maximum error as a voltage supply is ±(0.02% + 2.4mV). The two parts of the error arise from op-amp offset voltages (temperature-dependent) in different parts of the source/measure circuits - those on the input side are amplified and produce the percentage (gain) error and the rest are not amplified and produce the 'fixed' (offset) error. Similarly, the Keithley unit measures the current response of the module during the voltage sweep with a maximum error of ±(0.07% + 570μA). Cable losses are negligible when using the four-wire sense method.

The module temperatures are monitored with PT100 sensors, fixed to the module backs with heat-conductive adhesive and insulated to the rear. The maximum error associated with the PT100 is ±0.3˚C. The Keithley unit is employed to make the resistance measurement, which it does with a maximum error of ±(0.08% + 0.03Ω) resulting in an overall module temperature measurement accuracy of ±0.7˚C over the range –10˚C to +100˚C.

Data derived from raw measurements

Parameters such as I_{SC}, V_{OC}, I_{MPP} and V_{MPP} are derived from the raw I-V curves through interpolation, since the voltage sweep of the Keithley measurement is programmed as a start, end and number of points, meaning there are not necessarily exact measurement points for these values. However, given the large number of data points (100), the process does not introduce significant additional error on top of those associated with the measurement procedure.

In the following work of this and later chapters, energy weighting is often applied to values as they are averaged (because at very low irradiance, parameters built on ratios can pivot rapidly and transfer a high error). This is performed by multiplying each individual measurement of the parameter to be averaged by the concurrent irradiance measurement and summing this product for the bin (e.g. of time, or module temperature, etc.) before dividing by the sum of irradiance in the same bin. Also later in the thesis, energy yield calculations and modelling will be performed. For both solar resource and PV electrical output, energy is calculated from measurements of power and the sampling interval, during which the power is assumed not to vary. This assumption

introduces a statistical error which should reduce through averaging over longer timescales. The longest interval between instantaneous measurements is 10 minutes and applies to spectral irradiance, PV device data and the I-V bracketing thermopile measurements. The magnitude of the error was established with pyranometer readings of the 10-second meteorological data. Measurements from the beginning of a 10-minute period were compared to the averaged measurements from the same period. On this 10-minute basis, the standard error is ~70Wm^{-2}. Averaging both the instantaneous and 10-minute average values on an hourly basis reduces this error to ~30Wm^{-2}, Figure 2.6:

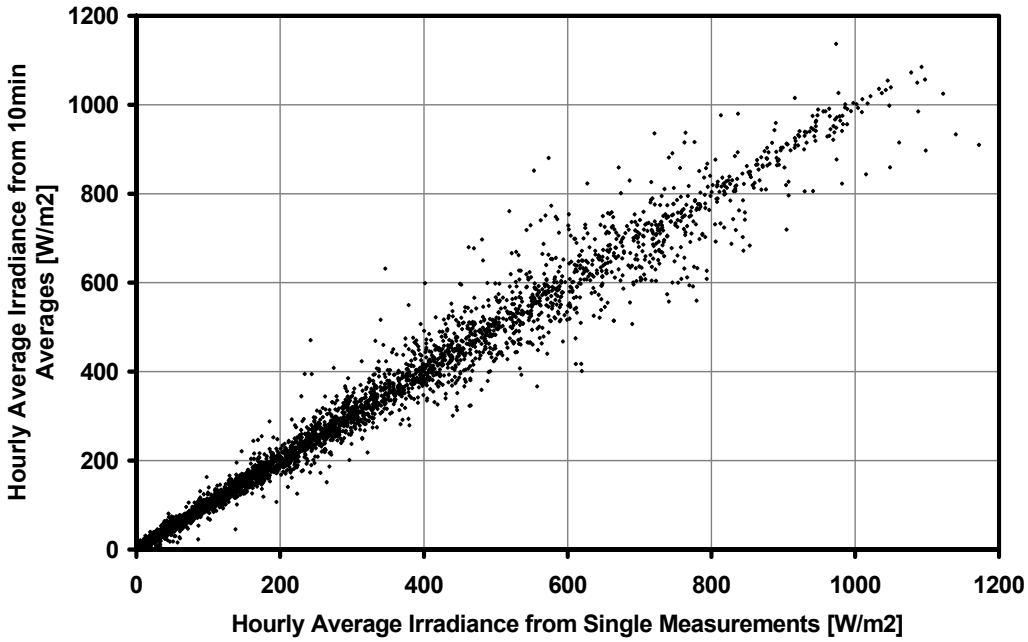

Figure 2.6: Hourly average irradiance calculated from single 10-minute values and 10-second values

On a daily scale, the error is reduced below the instantaneous instrumentation error for the irradiance measurement, Figure 2.7:

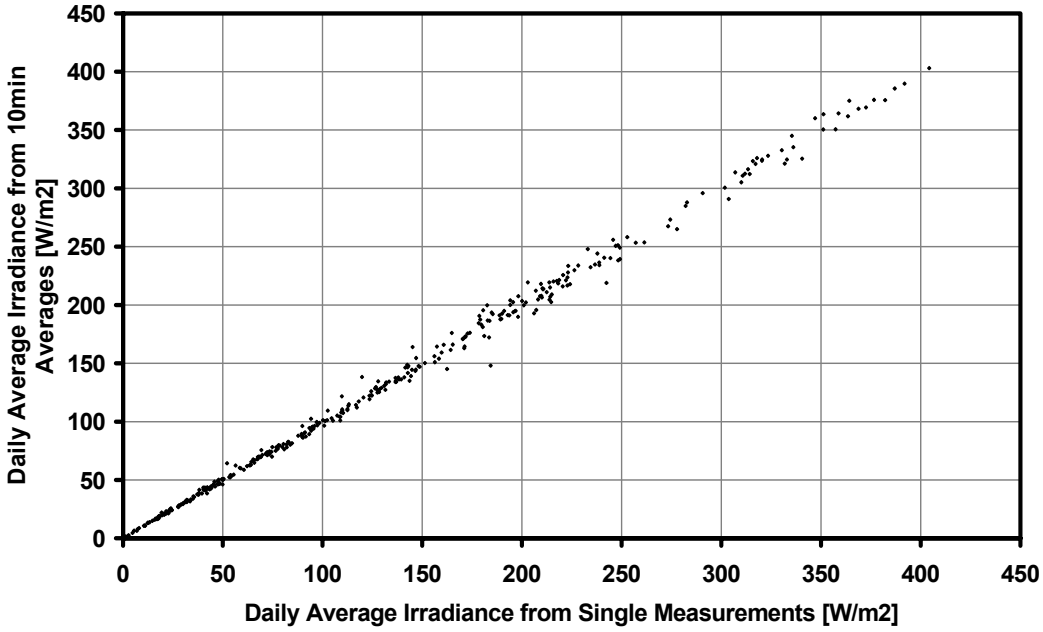

Figure 2.7: Daily average irradiance calculated from single 10-minute values and 10-second values

Most of the aggregated analysis in this thesis is on a monthly basis, where this induced error is negligible. It is important for some of the device modelling approaches in chapter 5, however, so will be considered again. The errors for the instantaneous measurement or calculation of the parameters discussed in this section are summarised in Table 2.2:

Parameter	Maximum Error
Irradiance (CREST)	±10% at 100Wm^{-2}, ±5% >500Wm^{-2}
Air Temperature (CREST)	±2˚C
Irradiance (LUMetS)	±3.5%
Air Temperature (LUMetS)	±0.5˚C
Air Pressure (LUMetS)	±6mB
Relative Humidity (LUMetS)	±3% at 90%RH, ±6% >90%RH
Spectral Irradiance	±5% (300-1700nm)
PV Module Temperature	±0.7˚C
PV Module Voltages (V_{OC}, V_{MPP})	±(0.02% + 2.4mV)
PV Module Currents (I_{SC}, I_{MPP})	±(0.07% + 570μA)
PV Module Maximum Power (P_{MPP})	±0.5%
PV Module Fill Factor (FF)	±1% (rel.)
PV Module Efficiency (η)	±11% at 100Wm^{-2}, ±6% >500Wm^{-2}

Table 2.2: Summary of final maximum error in each parameter

2.3 Spectral Irradiance Variation

2.3.1 Characterising the spectrum

Measured spectral irradiance data does not lend itself well to use in simple analysis or modelling approaches as it consists of an ensemble of measurements. Ideally, a spectral distribution would be summarised as a single parameter, which could then be used in much the same way as broadband irradiance and device temperature to isolate and quantify the different environmental effects acting on the PV device. The *colour temperature* associated with a blackbody radiator is an option that can reasonably represent the solar spectrum outside the Earth's atmosphere, but is unsuitable for terrestrial application because the various gas absorption bands and wavelength-dependent scattering prove too distorting. A few terrestrial spectral descriptors can be found in the existing literature, although not as many as might appear since often the same measure is used under different names by various groups.

One of the most established is the *calibration number* of NREL and it's variants [3]. The calibration number (CN) is based on the variation of the short-circuit current (I_{SC}) of a photovoltaic device and is defined as:

$$CN = A \times \frac{\int_a^b E_i(\lambda) SR(\lambda)\, d\lambda}{\int_a^b E_i(\lambda)\, d\lambda} = \frac{I_{SC}}{G} \tag{2.2}$$

where A is the active area of the device, SR its spectral response, G is the broadband (total) irradiance and E_i the spectral irradiance. For terrestrial applications the integration limits a and b are 300 and 4000 nm, respectively. The *normalised calibration number* describes the CN under an arbitrary spectrum relative to that under a reference spectrum (the same term *calibration number* is also sometimes used for this measure):

$$\overline{CN} = \frac{\int_a^b E_i(\lambda) SR(\lambda)\, d\lambda}{\int_a^b E_i(\lambda)\, d\lambda} \Bigg/ \frac{\int_a^b E_{REF}(\lambda) SR(\lambda)\, d\lambda}{\int_a^b E_{REF}(\lambda)\, d\lambda} \tag{2.3}$$

This removes the device area, but it remains a device-specific spectral characteristic through the spectral response. Typically, a crystalline silicon reference cell is used, limiting information of the spectrum to wavelengths under around 1100nm. Finally, any other influences on the photocurrent must be accounted for to provide true spectral information.

An alternative is to characterise spectra on the basis of ratios of integrated irradiance in different spectral bands:

$$R = \frac{\int_a^b E_i(\lambda)\, d\lambda}{\int_c^d E_i(\lambda)\, d\lambda} \tag{2.4}$$

where typically either b equals c and thus R is the ratio of 'blue' to 'red' about that wavelength, or c-d covers the total spectral range and then R becomes a measure of significance for the range a-b. However, in the former usage there is little consistency in the wavelength chosen as the boundary between blue and red bands. In the latter, the

range of interest, *a*-*b*, tends to be specific to the task in hand. In the case of PV research this is the extent of the spectral response of the device being studied and the resulting ratio has many synonyms, for example: *Photovoltaically Active Fraction* (PAF) [4], *Available Spectral Ratio* (ASR) [5], *Useful Fraction* (UF) [1]. The bands selected for crystalline materials are generally consistent (e.g.: 300-1100 nm for c-Si), but for amorphous, alloyed or compound materials there is variation reflecting the flexibility of the band-gap. This makes it unsuitable for a general spectrum descriptor, but the useful fraction does provide a convenient first order spectral correction to the broadband irradiance for performance analysis and will be revisited in this thesis.

The device-independent spectral characterisation used here is the *Average Photon Energy* (APE) and is derived only from spectral irradiance. The APE is calculated from measurements of spectral irradiance by dividing the integrated (broadband) irradiance by the integrated photon flux density, yielding the average energy per photon:

$$APE = \frac{\int_a^b E_i(\lambda)\, d\lambda}{q_e \int_a^b \Phi_i(\lambda)\, d\lambda} \tag{2.5}$$

where q_e is the electronic charge and $\Phi_l(\lambda)$ the spectral photon flux density. An average wavelength could as easily have been used, but the APE offers two minor advantages in that it correlates positively with spectral blueness that favours PV performance, and when expressed in electron-volts gives some feel of how a particular spectrum may affect devices whose band-gaps are also given in eV. It should be noted that the calculated APE value depends on the integration limits in equation (2.5). The effect this has is shown in Table 2.3 for the AM1.5G standard spectrum:

Wavelength Range (nm)	Average Photon Energy (eV)
300-4000	1.43
300-2500	1.48
300-1700	1.62
300-1100	1.86

Table 2.3: APE of the standard spectrum evaluated from different spectral integration limits

The best definition for the APE would be to use the full terrestrial spectrum (300-4000nm) as this gives the true APE value. However, instruments to measure this range are extremely rare, with none in use in long-term measurement regimes. The interval to 2500nm contains over 98% of the spectrum power (AM1.5G) and although there are still few of these instruments it is thought that measurements up to 1700nm could be extended to 2500nm with reasonable accuracy through modelling (a method to extend 300-1100nm silicon detector spectroradiometer measurements to 4000nm was developed at NREL some time ago [6]). It is preferred here, however, to use a figure based only on measurements. The system at CREST measures the spectral range 300-1700nm and unless stated otherwise the APE is calculated for this band throughout this thesis.

High values of average photon energy correspond to a blue-rich spectrum, whilst low values indicate a red spectrum. For reference, the standard AM1.5 global spectrum has an APE of 1.62 eV. Figure 2.8 shows examples across the range of the APE characteristic for spectra measured at Loughborough. The standard AM1.5G spectrum is also shown and all are normalised to the same broadband irradiance for comparison. The spectra shown are selected from one year's data excluding measurements below 200 Wm^{-2} broadband irradiance.

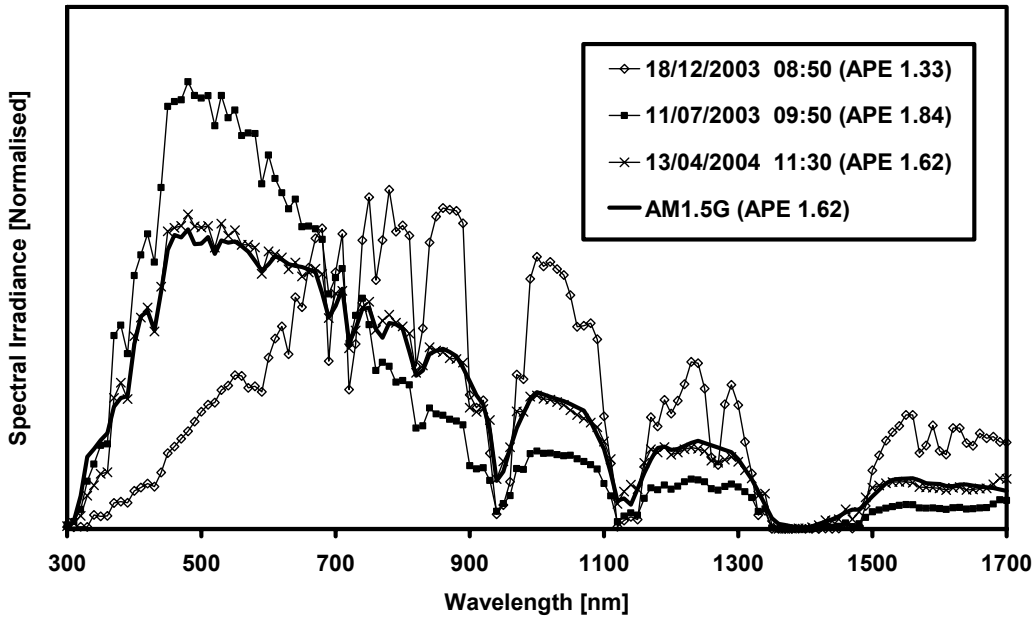

Figure 2.8: Example spectra showing the range of APE experienced at Loughborough

The disadvantage of the APE in terms of PV performance analysis is that it does not allow a direct feedback to the available useful irradiance as the Useful Fraction does. On the other hand, the UF is not appropriate for the comparison of the effects on different devices, as it includes device-specific information. However, there is a strong correlation between the average photon energy and the useful fraction, as shown for different PV technologies in Figure 2.9. Use will be made of this relationship and the useful fraction in chapter 5.

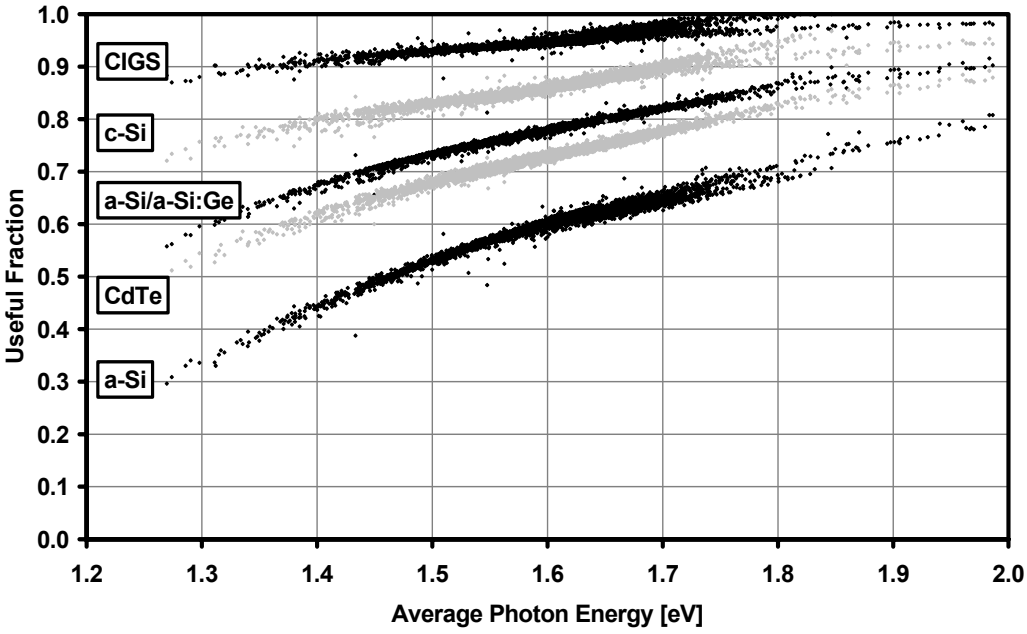

Figure 2.9: APE dependence of spectrally useful irradiance fraction for different PV technologies

2.3.2 Spectral Environment of the UK

There are a multitude of influences acting to determine the terrestrial solar irradiance spectrum at any one time. Firstly, there are bulk atmospheric effects dominated by path length (air mass) variation, with aerosol and water vapour content contributing to a lesser extent. Secondly, there is cloud cover, which acts to skew the spectrum in addition to its obvious impact on broadband irradiance. For the case of a fixed, inclined plane such as the vast majority of installed photovoltaic systems, there is also a slight effect due to the solar angle of incidence to the plane of array, as this sets the balance between the beam irradiance and the diffuse (with a much bluer spectrum, but also weaker overall power). The relative magnitudes of all these factors depend on the site since AM variation is a function of latitude; aerosol, water vapour and cloud levels are

due to the local climate; and the collector plane geometry is generally designed either for the latitude or the specific application.

In this section, long term spectral irradiance measurements conducted at CREST are analysed to assess the impact of these effects for the UK. As a reminder, the spectroradiometer is mounted in a plane inclined at 53° to the horizontal (latitude tilt) and faces a bearing 160°. The input comprises an integrating sphere with a domed aperture cover, resulting in an almost 2π str acceptance.

Figure 2.10 shows the variation of APE over the course of a (rare) clear day. Also shown are the broadband irradiance (spectroradiometer integrated output) and solar elevation and angle of incidence. The day depicted is from mid July 2003, although GMT is used for the time axis. At this time of year, the sun rises and sets behind the plane of array and high values of APE can be seen at these times, corresponding to the diffuse-only spectra. The spectrum then becomes rapidly redder as the solar disc impinges more on the measurement plane and the APE plummets.

Between 06:30 and 12:00, the APE is seen to increase again as the weak effect of variation in the solar angle of incidence (AoI) below 75° is overshadowed by the decreasing air mass and less blue light is scattered from the beam irradiance.

From GMT noon onwards, the APE demonstrates a slight positive trend. This could be attributed to the increasing AoI but also correlates with rising humidity during the afternoon. Since the water vapour absorption bands are clustered about the near infrared, increased atmospheric water vapour content acts to blue the spectrum.

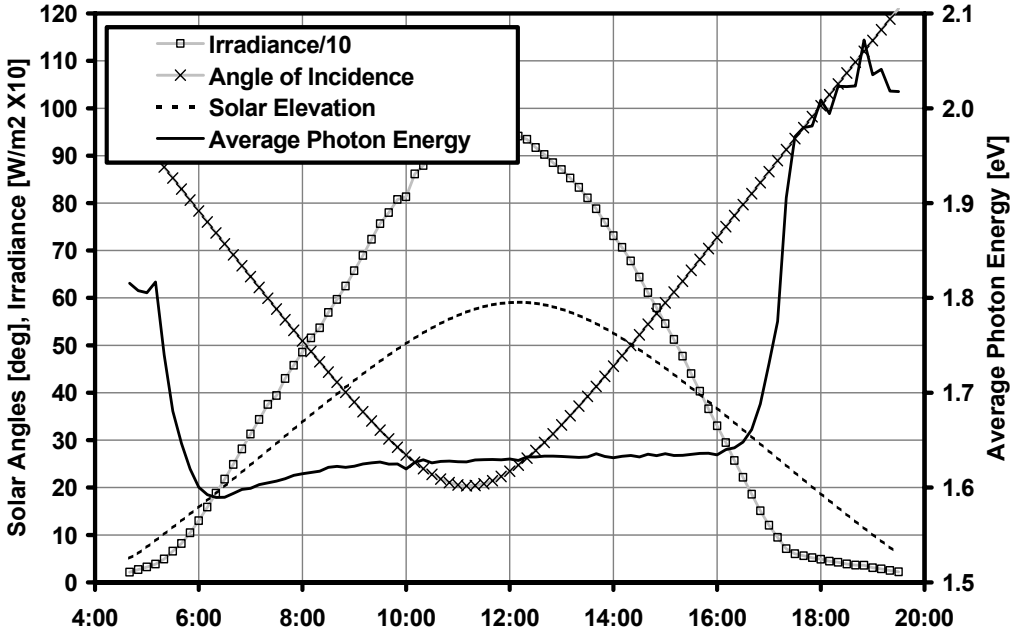

Figure 2.10: Spectral blueness variation – clear day study

Figure 2.11 shows the impact of clouds on the APE. Recalling that a spectral measurement takes approximately 2 minutes and that measurements are later filtered for irradiance stability over this time, it should be no surprise that a full set of reliable measurements does not exist for a cloudy day (barring completely overcast days). Actual measurements have been highlighted with point markers in the figure - lack of a measurement point implies rapidly fluctuating irradiance levels.

There is relatively clear half hour from noon (GMT), where it can be seen the APE is somewhat lower than in the previous example. This is due to seasonal variation in air mass. The previous example is a July day and this one a September day, where the sun rises later, sets earlier and does not rise so high at noon, leading to spectra which are redder on average. This average is overturned however in the presence of clouds. During the morning, the APE is seen to progressively decrease as the sky becomes clearer, in a reversal of the clear-sky case. The afternoon shows more abrupt changes in cloud cover, but the effect to skew the spectrum towards the blue is the same.

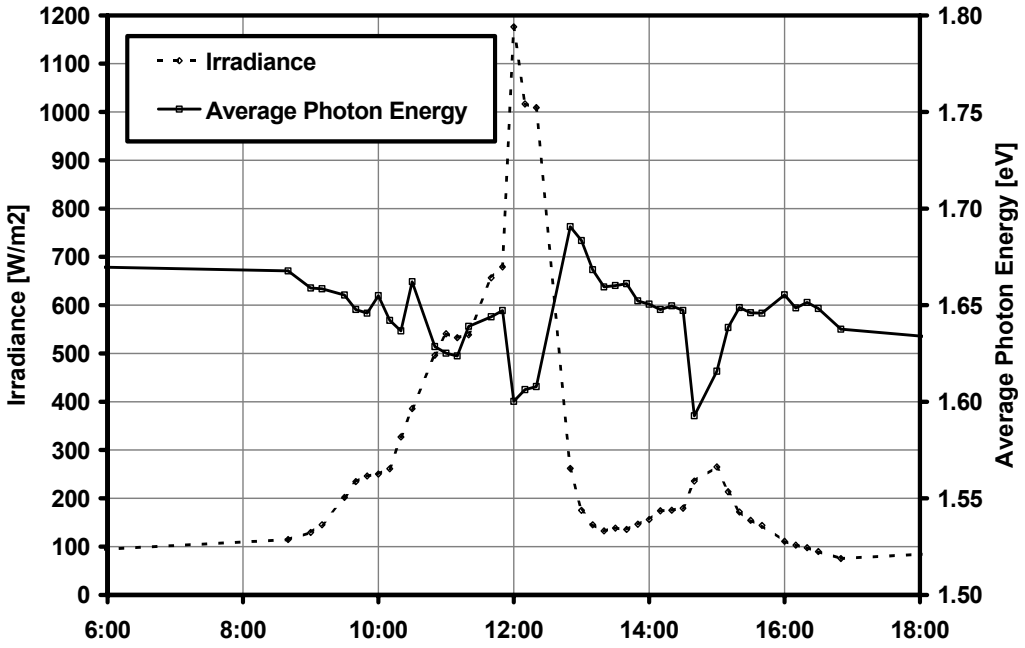

Figure 2.11: Spectral blueness variation – cloudy day study

In the following analysis, data was used with these restrictions: Since the highest quality filter for the spectral measurements has proved to be the stability test based on concurrent broadband irradiance measurements, only data where this is available have been included. This has limited the set to just over a year. The only other restriction is the rejection of data below $50Wm^{-2}$. This reduces low S/N errors from the spectroradiometer and excludes conditions marginal for energy production by PV.

Figure 2.12 shows the spread of APE with broadband irradiance. The plot is rather scattered since a given broadband irradiance can often arise through many different sky conditions, each with a different spectrum. This is not so much the case at very high irradiances however, as these only occur with cloudless skies and low air mass, seen on the right of the figure. The clearly defined boundary to the bottom of the data field corresponds to cloudless skies. Points found further from this boundary are associated with conditions of increasing cloud cover, which are represented in a dense cluster in the top left. This graphic will reinforce the argument that spectral irradiation variation is not a significant effect on photovoltaics, assuming irradiances below $500Wm^{-2}$ are dismissed as energetically negligible. However, many countries proposing increased use of PV do so despite having a poorer solar resource, where a significant proportion of that resource is delivered at lower irradiances.

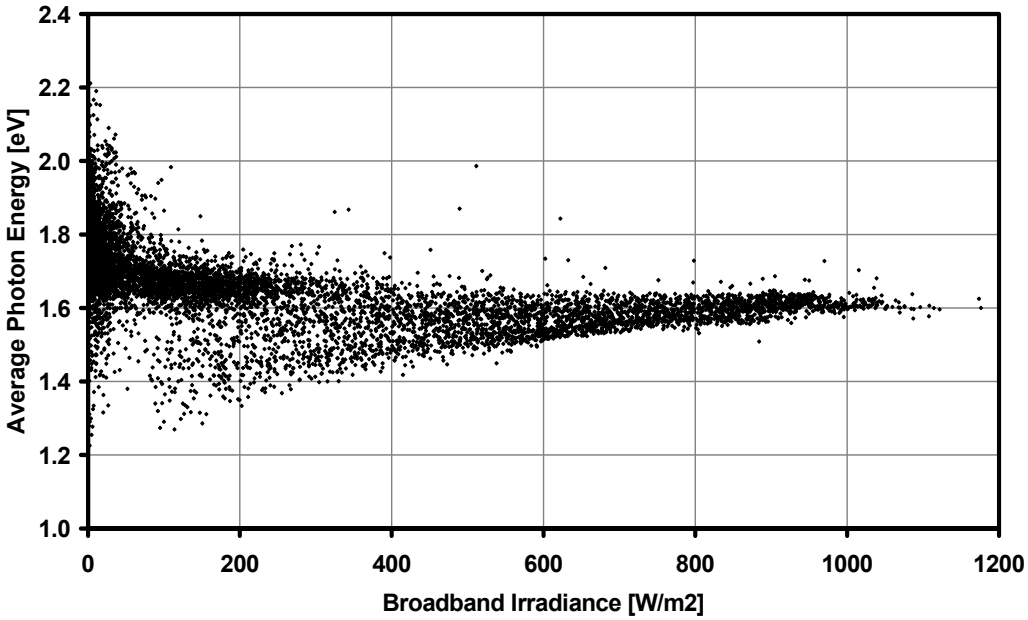

Figure 2.12: Spectral blueness variation with broadband irradiance

By filtering the data by angle of incidence and clearness, it is possible to strip out the dependence on air mass, as in Figure 2.13. For the UK Midlands, the minimum daily air mass varies from 1.15 on the summer solstice to 4.27 on the winter. The rate of change of solar elevation also varies with the season, with an impact on the time spent with the Sun at different AM.

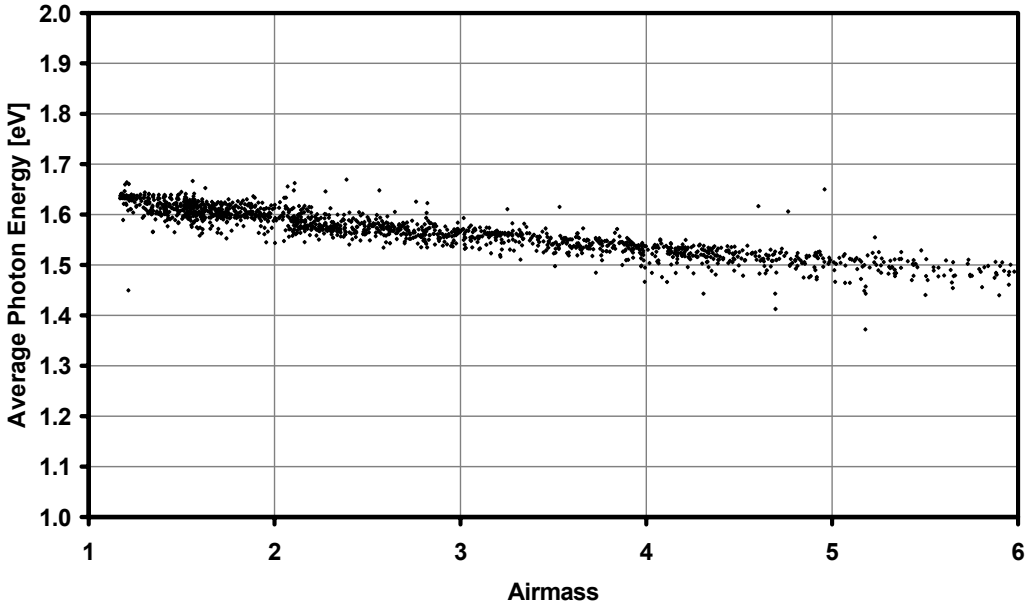

Figure 2.13: Spectral blueness variation with Sun position (airmass)

Figure 2.14 shows the data filtered again by AoI and then into three AM bins to demonstrate the effect of cloud cover. The opacity of the atmosphere is generally represented by the clearness index (k_T), defined as the ratio of total irradiance measured on a horizontal plane at the Earth's surface to the total extra-terrestrial irradiance incident on a horizontal plane at the top of the atmosphere:

$$k_T = \frac{G_H}{G_0 / AM} \tag{2.6}$$

where G_0 is the solar constant. However, this parameter is not independent of the air mass since it is a measure of the total broadband attenuation and hence is affected not only by the amount of cloud present, but also by the atmospheric path length.

To separate the two effects, an AM-independent variable to describe clearness is used, the cloud index (k_T*), following the approach of Merten & Andreu [7]. Measured global irradiance data for the site of interest is plotted against air mass and a line fitted to its upper boundary to mark the highest irradiance possible for that site at that air mass. Here, the following functional form was used:

$$G_{MAX}(AM) = \frac{G_0}{AM} \times e^{(-\tau AM)} \tag{2.7}$$

where τ is fitted empirically for the site and G_{MAX} replaces the denominator in equation (2.6). It will be noted that this formula does not expressly consider the diffuse irradiance contribution. However, it compares well to the more involved Perez-Kasten formula [8] and has the benefit of fewer empirical coefficients. Values greater than 1 arise from the judgement of exactly where to draw the boundary in the irradiance-AM plot.

To the right of Figure 2.14, representing clear skies, the effect of AM on the APE can be seen as before. It is apparent that increasing cloud cover skews the spectrum to the blue no matter what the AM and the effect becomes independent of AM below a cloud index of 0.5.

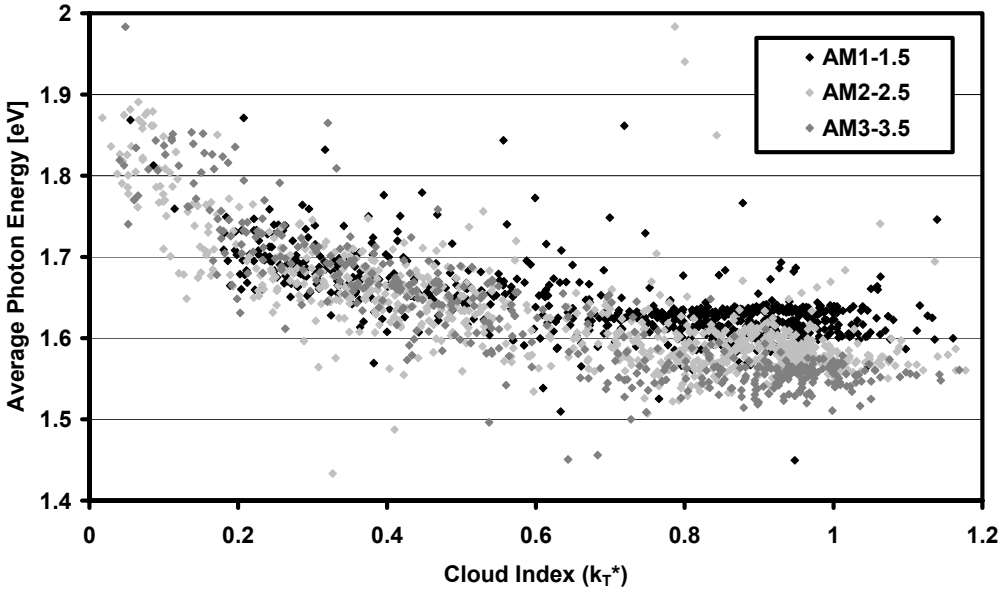

Figure 2.14: Spectral blueness variation with cloud cover (k_T*)

On an annual basis, clouds play a significant role in dictating the spectral irradiance conditions of the UK. Figure 2.15 shows the distribution, by data count and incident solar irradiation, of average photon energy. The distribution is drawn from data taken from September 2003 to August 2004 (inclusive), since this comprises an almost uninterrupted 12-month spectral irradiance measurement period (Figure 2.3). The peak in the frequency count curve is at a considerably higher APE than the STC value of 1.62eV. This is principally due to cloud effects, as can be seen in the lower APE value of the peak in the solar irradiation curve (i.e.: not so much solar energy reaches the site when it is cloudy – rather as one expects). Yet the sheer number of instances of cloudy skies skews even the annual distribution by energy. Given that the minimum airmass of 1.15 experienced in Loughborough leads to clear-sky spectra of APE ~1.65eV (Figure 2.13), a conservative estimate of the solar irradiation delivered under cloudy skies might be 25% of the annual total. A further 25% arrives at APE lower than the STC spectrum, due to the latitude of the site and hence long periods of time spent with a high AM sun.

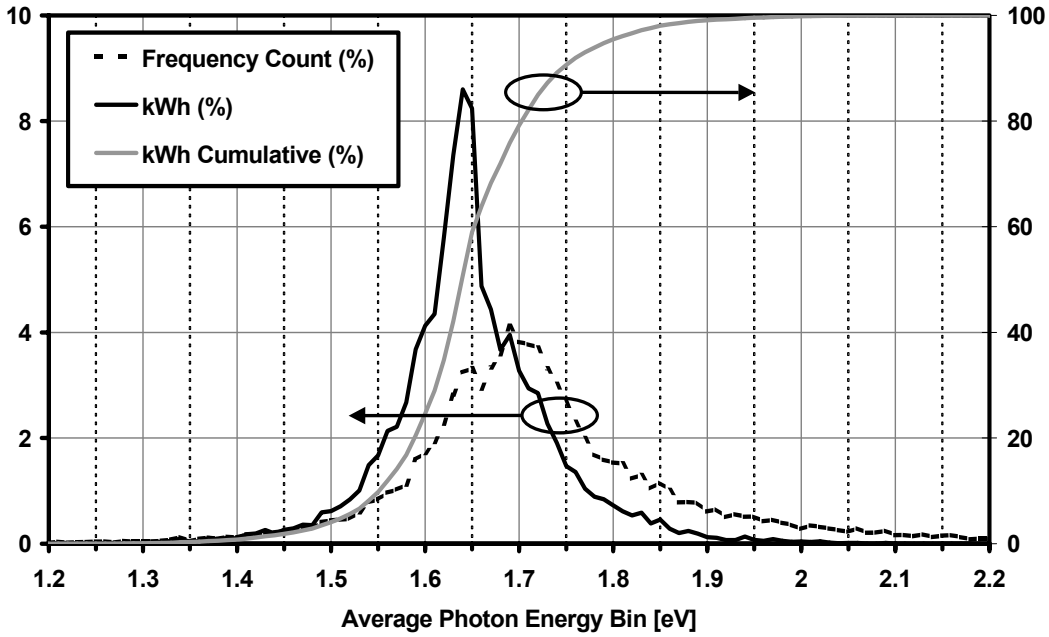

Figure 2.15: Annual distribution of spectral blueness, by frequency count and incident solar energy

Figure 2.16 shows how this distribution breaks down to give a clear seasonal pattern to the solar irradiance spectrum. The data are presented as monthly averages weighted by irradiance, to give a clearer idea of the energetic significance than a count-based average. Since there is little variation in cloud cover between the seasons in the UK, the seasonal pattern seen in the figure is due predominantly to AM variation. The influence of cloud cover is to pull the APE up all year round.

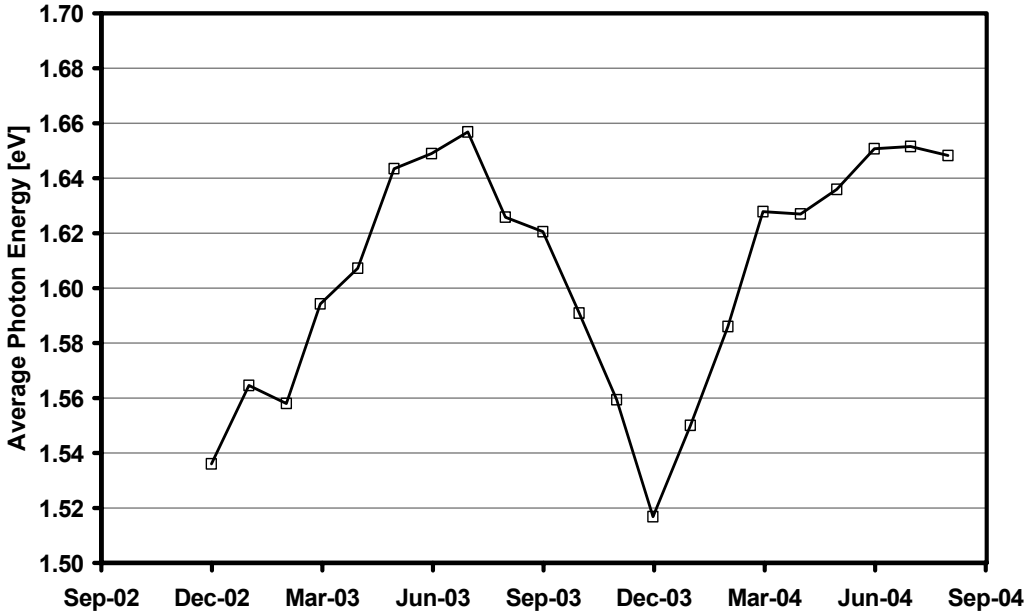

Figure 2.16: Seasonal variation of spectral blueness in Loughborough

2.3.3 Spectral Environment of Other Locations

Only one other set of continuous long-term spectral irradiance measurements exists in the world (or at least is publicised) – that of the U.S. National Renewable Energy Laboratories (NREL) in Golden, Colorado. The NREL outdoor PV testbed includes two spectroradiometers, one mounted horizontally and one at latitude tilt (~40˚). Both are based on silicon detectors, so have a measurement range limited to 300-1100nm. Thus in the presentation of the following data, the average photon energy has been calculated for this range.

Figure 2.17 demonstrates that the seasonal variation is not limited to such high latitude sites as the UK only. Accounting for the difference in APE scales, the magnitude of the variation is lower for Golden and the winter dip not so sharp, as could be expected from the latitude.

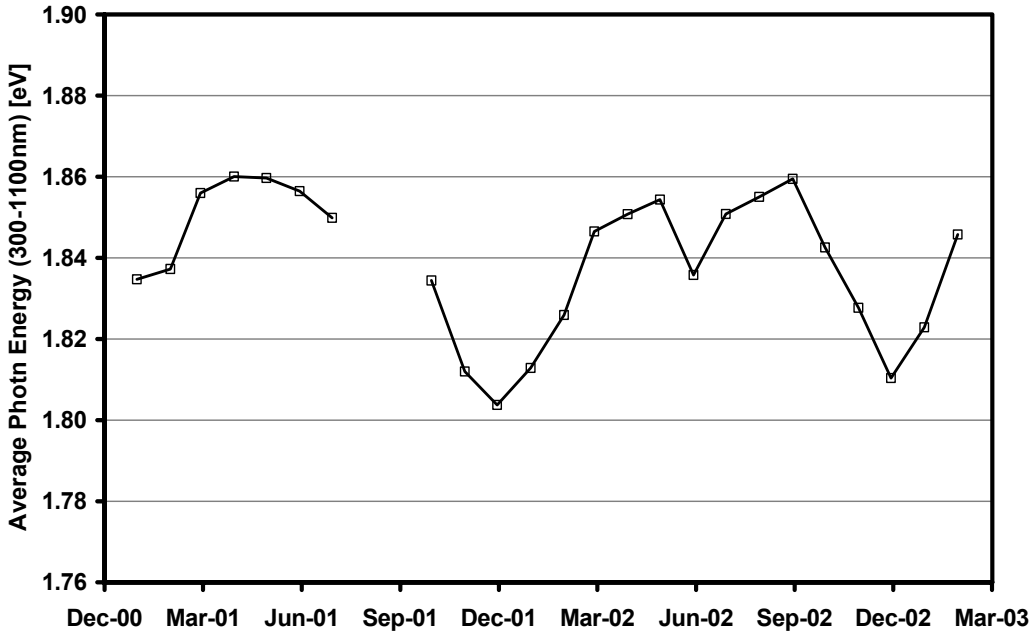

Figure 2.17: Seasonal bariation of spectral blueness in Golden, Colorado

Finally, Figure 2.18 shows how the spectral environment of Golden differs from that of Loughborough. The spectral irradiance standard used in the STC was originally an ASTM standard. Recalling from Table 2.3 that the standard spectrum has an APE (300-1100nm) of 1.86, comparison to the figure below might explain the choice for the standard in the first place.

Aside from the difference between the peaks of the Loughborough and Golden distributions, low cloud amount in Colorado is also evident in the rapid drop-off at higher APE values, with very little tail into this region. The effect of high winter airmass is similar to both locations, with Loughborough receiving a slightly higher proportion of its solar energy under such conditions.

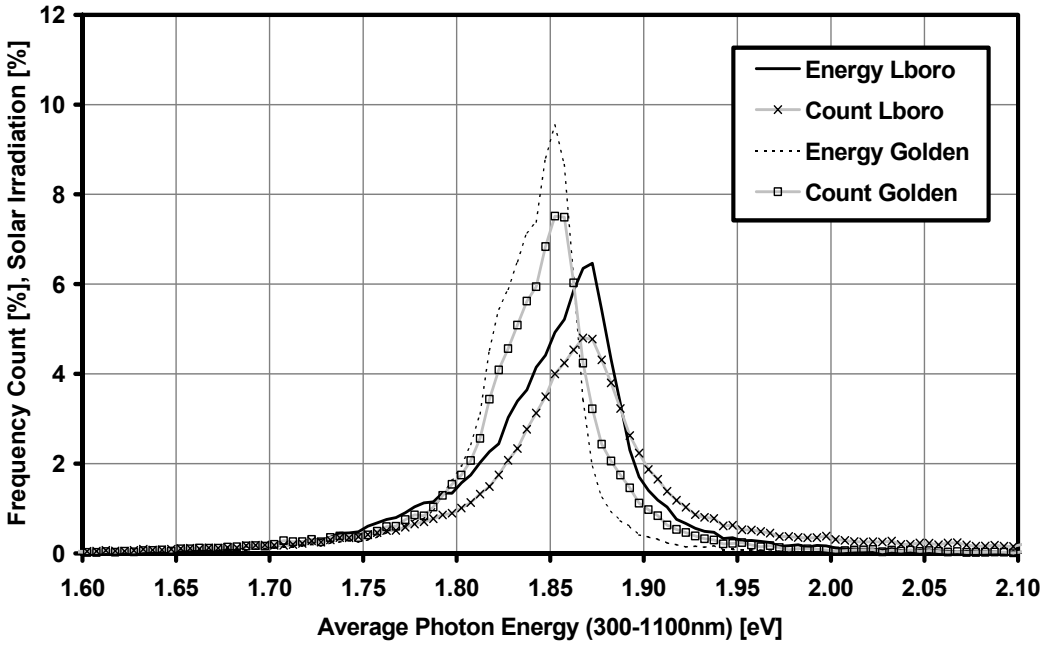

Figure 2.18: Annual distribution of spectral blueness, comparing Loughborough and Golden

2.4 Conclusions and Recommendations

2.4.1 Measurement System and Data Processing

The outdoor measurement system at CREST is undoubtedly one of the better ones currently operating, but of course has its problems. The prioritising of three specific improvements above all else is suggested to improve future data collection:

- Failsafe control of the logging PC clock. The timing issues concerning measurement of solar-driven influences are critical. Problems arose in this area principally through a lack of communication between administrative and academic units within the university and inflexibility of control software accompanying elements of the system hardware. After a considerable amount of time spent by the author, this issue has now been laid to rest for the present system incarnation, but there will always be evolution of such measurement systems and the experience of the author should be heeded to avoid future frustration.

- Investment in a commercial data logger will provide a good return. The largest environmental factor influencing the output of PV devices is irradiance, so the more accurately it can be measured the better. The CREST system does not have uncommonly large errors in this respect, but it has been noted the largest contributor is the in-house built boost circuitry. However, CREST has recently acquired a Campbell Scientific CR series logger and this is sure to improve the next version of the system.

- As more detailed effects on PV are investigated, system measurement speed will need to increase. Currently, a rather long time is necessary to measure the spectrum and an even longer time to measure I-V curves as more devices are added to the roof. Eventually, more than one Keithley (or other) measurement unit will be required, with additional multiplexers working in parallel. This should narrow the gap between measurements of different parameters and not so much data will need to be filtered out because of stability of the conditions.

2.4.2 Spectral Characterisation

In the following chapters investigating the influence of the spectrum on PV devices, the average photon energy will be used to characterise the spectral conditions, as this has been found to be a convenient, device-independent spectral descriptor. For sites where no spectral measurements exist, spectral irradiance modelling is proposed as an alternative source from which to calculate the APE and will be treated in a further chapter.

A better solution for widespread implementation, since it relies only on measurements and reduces error, may be through the use of filtered pyranometers measuring two or more spectral bands. This is not a quick or easy solution however as it requires expenditure on additional sensors and essentially, specification of measurement bands/filters as an addendum to current measurement standards.

2.4.3 Spectral Variation

Variation in the solar irradiance spectrum, both theorised and previously observed at other locations, has been confirmed in the CREST measurement data and quantified using the APE as a measure of spectral blueness. Further influences, specific to the location have also been observed. Key drivers determining spectral variation are discussed in depth in the chapter on spectral irradiance modelling, but may be summarised as follows:

- Bulk atmospheric effects. Increasing values of airmass (lower solar elevation) result in a reddening of the spectrum since the scattering of shorter wavelength radiation by air molecules results in a reduced forward transmission compared to that of longer wavelengths. Increased aerosol turbidity enhances this effect, since again shorter wavelengths are scattered to a greater extent. Increased atmospheric water vapour content decreases this effect as absorption occurs mainly at longer wavelengths.

- System orientation effects. Solar angle-of-incidence effects are noticeable at angles > 75˚. It is not possible to say to what extent this is due to the angular response of the spectroradiometer. However, while calibration charts have not been forthcoming, the integrating sphere specification claims a ‘near-perfect’

cosine response. Also, findings do agree with a prediction of increased APE for more diffuse irradiance in the irradiance mix impinging on the measurement plane. For the CREST system, such conditions represent a very small fraction of the available solar resource, but could manifest as more significant in other system designs such as vertical PV facades for buildings. Another PhD underway at CREST is investigating AoI effects on PV modules and will include further evaluation of the spectral contribution.

- Weather effects. Previous observations refuting the neutral-density filter hypothesis for cloud and demonstrating higher transmission for shorter wavelengths have been confirmed in the CREST data. The theoretical debate is on-going and is split between simply increased water vapour absorption in the near-IR, complex multiple scattering phenomena in the blue, and albedo enhancement through increased sky reflectivity. Currently, CREST does not have the instrumentation to add to this debate since measurements of beam and diffuse spectral irradiance are needed as a minimum.

2.4.4 Spectral Environments

The spectral environments of Loughborough and Golden, Colorado were compared and shown to be quite different. The peak in the annual solar energy distribution by spectral blueness appears to be set by the latitude of the site, due to the airmass effect.

Golden enjoys a much sunnier climate than Loughborough and this has propagated to the energy distribution. The effect of a cloudy climate is to broaden the distribution into the blue, extending it to higher APE values. This has been demonstrated to constitute more than just a low-energy tail, with at least a quarter of Loughborough's solar energy resource delivered under these conditions.

Based on analysis of the spectral solar irradiance resource, there is evidence that the current standard spectrum may not be applicable universally as the best design point for PV modules in terms of energy extraction. However, the effects of this spectral variation on the performance of real PV devices must be investigated first, to determine their significance on electrical energy production. This is the topic of the following chapter.

3 Effects of Irradiance Spectrum on Photovoltaic Devices

The work in this chapter aims to contribute to the understanding of the effects of operating environment on photovoltaic device performance. The focus is on the consequences of spectral irradiance variation. This environmental factor has not previously received a full impact analysis, partly because of the increased demands of its measurement and parameterisation but also because it is often considered to cause a relatively weak effect on PV. The reasons behind this conclusion and the recent questioning of such a stance are discussed in the following overview of the topic.

The environmental factors influencing PV device performance are the device temperature, total irradiance level, irradiance spectrum and optical effects due to shading and the solar angle of incidence to the device. A distinction is made between these factors, which affect efficiency on short timescales, and module degradation. The latter is a long-term, rather steady decline for most modules, applying also to stabilised amorphous silicon (the arguments concerning seasonal recovery of light-induced degradation are explored below).

Numerous performance analysis studies have been carried out to assess the magnitudes of these effects, yet there is still some debate about the relative importance of each factor. This is due partly to the fact these influences are not independent of each other. Their separation for quantification has proved a major challenge that has not yet been met conclusively. Therefore any discussion of the effects of spectral variation necessarily involves consideration of the other environmental influences.

3.1 Overview of performance investigations and modelling

There is much variation in the extent to which the irradiance spectrum affects energy production through photovoltaic devices. Firstly, the variety of spectral distributions encountered is site specific, since the main drivers for spectral change are the path length through the Earth's selectively absorbing atmosphere and the opacity of the atmosphere. The seasonal and daily variation in the path length is determined by the site latitude and the opacity is due to the local climate and weather of the site. Secondly, there are large differences in the sensitivity of different PV materials to spectral variation. This is determined in the first instance by the band gap of the material, which sets the upper wavelength limit of the spectral response. The fine structure of the response, reflecting the absorption and transport qualities of the material, completes the definition of which parts of the incoming spectrum the device can utilise. Finally, there are detection issues relating to the instrumentation used to measure the irradiance value for the calculation of device efficiency. If a pyranometer with similar spectral response to the PV device is used, any spectral effect will remain undetected since the measured 'broadband' irradiance will vary as the output power of the PV. This would be the case for example when using a silicon pyranometer to monitor conditions at a crystalline silicon (c-Si) PV system.

Ignoring or being unable to account experimentally for any of these factors has led to differing opinions as to the impact of spectral irradiance variation, as researchers focus on a single technology or perform tests at a single location. This combines with the influence of other environmental factors to produce a rather confused picture. A typical example is the ongoing uncertainty in the underlying causes of the observed seasonal performance variation in amorphous silicon (a-Si) devices, with the research field split over the contributions of spectral variation and reversal of light-induced degradation through summer annealing [9], [7].

Analyses of environmental, and hence spectral, effects take one of three strategies or a combination thereof. Studies based on **pure simulation** parameterise the various environmental factors and model PV device response to these changes based on some representation of the device. The earliest investigation into the dependence of solar cell performance on the spectrum was carried out in this way [3]. Osterwald simulated spectra using the clear-sky model SPCTRAL2 (discussed in the following chapter).

These are parameterised by the solar zenith angle and atmospheric turbidity (aerosol content) and water vapour content. The device performance indicator is the short-circuit current, modelled as:

$$I_{SC} \approx I_{PH} = A_{active} \times \int E_i(\lambda) SR(\lambda) \cdot d\lambda \tag{3.1}$$

I_{PH} is the photocurrent, A_{active} is the area of the device (m^2), E_i is the incident spectral irradiance ($Wm^{-2}nm^{-1}$) and SR is the spectral response of the device (AW^{-1}). The calculated I_{SC} values are normalised by the total (broadband) irradiance and presented relative to I_{SC}/G under STC. Devices of four materials are simulated: mono-crystalline silicon (c-Si), amorphous silicon (a-Si), gallium-arsenide (GaAs) and cadmium-sulphide/copper-indium-diselenide ($CdS/CuInSe_2$). Despite the limitations of the study, a significant difference is seen between the a-Si device, favouring bluer spectra, and the others, favouring redder. This is due to the blue-centred, rather narrow spectral response of the a-Si material.

Faine et al performed similar work, modelling spectra with SPCTRAL2 for a variety of hypothetical test cells of different band gaps [10]. One part of the study is an investigation into the difference in annual energy production at different latitudes for each of the devices. The result is a 17% reduction in the annual energy yield of the 1.4eV gap device when operated at a latitude of 50 degrees (e.g. Penzance) compared to the equator. There is a 25% reduction for the 1.9eV device. These figures do not include temperature or angle-of-incidence effects, but broadband irradiance reduction due to obliqueness of the solar angle is present. Although only the effect of air mass variation is modelled in the spectrum (i.e. weather conditions are not taken into account), a much stronger spectral effect for the high band gap material is apparent in this theoretical approach.

The strength of these methods is that effects can be very easily separated, as shown. However, one must be cautious about drawing strong conclusions since the modelling of any environmental process tends to be rather complex and hence imperfect. In addition other, unmodelled, influences are likely to be acting to reinforce or offset that which is investigated and it may be misleading to ignore them. Finally, the PV models used must be able to simulate the device response reasonably well for the results to be

meaningful: this becomes an issue with materials such as amorphous silicon, for which the established simple diode models are not wholly appropriate.

Research based on **indoor measurements** utilises a solar simulator to control the environment of a real device in a known way and thus isolate different effects. Aspects of the test environment are varied one at a time or in combination and the electrical parameters of the PV device monitored to derive response functions. These may be simple empirical fits of I_{SC}, P_{MPP}, etc. to each environmental factor, or may incorporate more detailed device modelling to determine trends for the underlying parameters. The response functions are applied to environmental data either simulated as in the above methods, or sourced from actual meteorological measurements.

Although device temperature and total irradiance can be varied with some precision in a simulator, it is far more difficult to vary the spectrum in the lab in any fashion that resembles genuine operating conditions. Under these circumstances, spectral effects are either omitted or are accounted for in further modelling.

A major piece of work into the operational performance of PV has been the development of the Realistic Reporting Conditions (RRC) method of the Fraunhofer Institute for Solar Energy Systems (ISE) [11]. The method estimates the deviation of power generated under realistic conditions from that generated under STC by separately modelling the effects of irradiance, temperature and spectrum differences from their STC values. In the original work, power output is simulated from empirical relations of device response to the different factors, as measured indoors. Heidler et al [12] apply the method to c-Si, poly-crystalline silicon (p-Si) and GaAs modules, modelling the devices with the two-diode equation:

$$I = I_{01}\left(e^{e(V-IR_S)/kT} - 1\right) + I_{02}\left(e^{e(V-IR_S)/mkT} - 1\right) + \frac{(V - IR_S)}{R_{SH}} - I_{PH} \qquad (3.2)$$

I_{01}, I_{02} are the dark saturation currents, R_S, R_{SH} are the series and shunt resistances, m is the ideality factor, e is the electronic charge, k is Boltzmann's constant and T is the device temperature. I-V characteristics were measured in a simulator at several different combinations of irradiance and temperature and used to fit the parameters of the two-diode model. The photocurrent I_{PH} is modelled through equation (3.1) to complete the

device model, which can then be used to calculate power output and efficiency for a given set of irradiance, temperature and spectral conditions.

The RRC method was put into practice using meteorological data from the institute, including long-term spectral measurements. Although there were no outdoor PV measurements to validate the results, these matched expectations regarding the much-investigated temperature effect. Minimal spectral effect was determined, again as expected for the low band gap materials studied. It is not documented why a-Si was excluded from the work, but it is possibly due to the poor representation the two-diode model makes of non-crystalline materials. However, a-Si, c-Si, p-Si and GaAs were all included in a precursor study at the institute in the previous year, looking only at spectral effects on the short-circuit current [13]. Equation (3.1) was applied to two years of measured spectral irradiance data, leading the authors to conclude that spectral variation is of negligible significance to crystalline silicon performance, marginal for GaAs and important for a-Si and similar high band gap devices. For a-Si they showed deviations in the I_{SC}/G ratio from the STC spectrum of up to 9% on a monthly timescale.

In the subsequent publications regarding implementation of the RRC method [11], [14], [15], the spectral component is discussed but never included in the final analysis. Different, empirical, approaches are applied to circumvent the previous difficulty in modelling a-Si devices, so the absence is most likely due to the lack of available measured spectral data. In the latter paper, a way forward is identified through spectral irradiance modelling. This is also the course taken in the detailed paper by Nann and Emery [16], who adopt the RRC method (with a two-diode PV model, rather than the original empirical fit-to-measurement) and spectra simulated with the SEDES2 extension to NREL's SPCTRAL2 code. The following chapter on spectral irradiance modelling includes a full review of these and other routines.

Parretta et al [17] have carried out a validation of the RRC method, using measurements of beam and diffuse irradiance to approximate spectral data and adding a loss mechanism for reflection. The RRC simulation agreed with measurements to within 5%, although only a c-Si module was studied, for which temperature increase was the main loss factor and is also the simplest to model. To date, there is no published validation for a-Si modules using measured spectral data.

Experiments using **outdoor measurements** of device and environmental data face the challenge of untangling the complex inter-dependency of environmental parameters to separate their effects. A standard approach when research relies on outdoor measurements is to filter the data according to the environmental factors *not* under investigation to a small range of values, thus limiting their effect on the PV device. For example, an extraction of the temperature coefficient would normally be made with data from a narrow bin of irradiance around the STC value of 1000 Wm^{-2}. Problems arise regarding the parameterisation of the spectrum, however, because so few research institutes measure it as a matter of course. Where no measurements of the spectrum exist, the best that can be done is an air mass correlation under clear skies. This approach severely limits the range of spectral conditions taken into account.

Hirata & Tani [5] performed outdoor I-V and temperature measurements of p-Si and a-Si modules for a year, with concurrent spectral irradiance measurements using filtered pyranometers as well as standard broadband measurements. A conventional procedure is used to calculate module power based on STC efficiency with irradiance and temperature correction:

$$P_{MPP} = D \times G \times A \times \eta_{STC} \times \left[1 + \alpha_{PMPP}\left(T_{MOD} - T_{MOD}\big|_{STC}\right)\right] \tag{3.3}$$

D is a constant allowing for decreased efficiency due to dirt build-up (0.94, 0.93 for the p-Si and a-Si modules, respectively). G is the irradiance, A is the module area, α_{PMPP} is the lab-measured temperature coefficient of maximum power, T_{MOD} is the module temperature and $T_{MOD,STC}$ is the module temperature at STC (25˚C). The measured power values are accumulated on a monthly basis and plotted relative to the power calculated through equation (3.3). Over the year, variation of 20% is seen for the a-Si module, with the peak in summer. The available spectral ratio (or useful fraction UF – as discussed in the preceding chapter) for each module is also calculated on a monthly basis as:

$$UF_m = \frac{\int_0^{t_m}\int_{\lambda_1}^{\lambda_2} E_i(\lambda)\cdot d\lambda \cdot dt}{\int_0^{t_m}\int_0^{\infty} E_i(\lambda)\cdot d\lambda \cdot dt} \tag{3.4}$$

$E_i(\lambda)$ is the incident spectral irradiance, λ_1, λ_2 are the lower and upper wavelength limits of the module spectral response and t_m is the length of the month. Variation in the monthly UF values of 14% is seen over the year for the site (Tokyo) for the a-Si module, coinciding with the variation in the measured power output (corrected for broadband irradiance and temperature). A smaller, but just as well correlated variation is seen in the UF and power output of the p-Si module. The authors conclude that spectral effects are critical for high band gap devices, but make no analysis of other contributing effects which may cause the discrepancy in magnitude of the observed variations.

The Sandia National Laboratories (SNL) in the U.S.A. have developed a PV performance model based solely on empirical correlations to outdoor device data [18]. The model is valid only for clear skies – data not fulfilling this criterion have been filtered out so as to fit the air mass (AM) dependency function used to account for spectral variation. Separate temperature coefficients for I_{SC}, I_{MPP}, V_{OC} and V_{MPP} are determined from the module specifications and are used to correct all measured values to a standard temperature (50˚C is used). Measured, temperature-corrected, I_{SC} data are plotted against AM and parameters for a polynomial are fitted to derive a spectral correction function. Angle-of-incidence (AoI) effects are similarly taken into account, again with I_{SC} data used since both these effects adjust the irradiance, which mostly influences the photocurrent. The measured plane-of-array (PoA) irradiance is modified for spectral (AM) and AoI effects and has temperature-corrected I_{SC}, I_{MPP}, V_{OC} and V_{MPP} data plotted against it to derive further empirical dependency functions. In this way the authors claim to have a method for calculating power output for any environmental conditions occurring under clear skies. The validation of the approach appears impressive, but relies on the same environmental data as was used to fit the PV parameter dependencies and is carried out for only one type of crystalline silicon module. It is thus not presently clear how applicable the method is for other locations and materials, but work on these is on-going as it is currently the favoured approach for the new power and energy rating standard draft [19].

BP Solar also have an empirical approach to PV system modelling to calculate power output [20]. They suggest a general five-parameter function to represent PV response to the environment, where the physical significance of the parameters is unimportant, i.e. it is not an investigative tool as far as the operation of the modules is concerned, but the

calculation result can be compared to the measured output to fault-find. The five parameters are determined through fitting to measured data at one location:

$$P_{system} = \left(\sum_t G\right) \times \left[A_t + B_t \times \left(\sum_t G\right) + C_t \times \overline{T_{amb}} + D_t \times \overline{WS}\right] - E_t \qquad (3.5)$$

The parameters *A*-*E* depend on the time period of the fitting dataset (*t*), which may be an annual set or monthly to investigate seasonal output variation. Irradiance, *G* is summed over the period, ambient air temperature, T_{amb} and windspeed, *WS* are averaged for the period. Once the parameters have been fitted for a system or module installed at one site, meteorological data from a proposed site can be folded in to estimate the electrical power yield for the new system (similar to the measure-correlate-predict methods used in the wind power industry).

In contrast, the paper of Merten & Andreu [7] presents a detailed approach to the analysis of environmental effects on a-Si devices. The device model is Merten's adaptation of the one-diode I-V model to a-Si, through the addition of a term accounting for recombination losses in the intrinsic layer:

$$I = I_{PH}\left(1 - \frac{d_i^2}{(\mu\tau)_{eff}\left[V_{bi} - (V - IR_S)\right]}\right) - I_0\left(e^{e(V-IR_S)/mkT} - 1\right) - \frac{(V - IR_S)}{R_{SH}} \qquad (3.6)$$

d_i is the thickness of the intrinsic layer, V_{bi} is the built-in voltage, $(\mu\tau)_{eff}$ is the effective lifetime-mobility product and the other terms are as in equation (3.2). Linear temperature coefficients for I_{SC}, V_{OC}, FF, efficiency, R_S and R_{SH} are determined from outdoor measurements. The module temperature is varied and I-V curves measured over a short period of time around noon, to minimise spectral and total irradiance changes (thus isolating the temperature effect). These coefficients are then used to correct other I-V data to a standard temperature (25˚C) to perform an analysis of spectral effects for clear-sky conditions, which are concluded to yield a 16% increase in efficiency in summer relative to winter for the Barcelona site (41.5˚N).

The pure simulation, indoor measurements and outdoor testing methods each have their strengths and weaknesses. Simulation enables very definite separation of different effects, but one needs reliable models to draw conclusions relevant to real systems.

Indoor measurements allow very precise characterisation of devices in a well-controlled environment, but tend not to be able to test modules over the full range of conditions experienced in installation. Outdoor testing guarantees realistic operating conditions, but results must be interpreted with a mind open to all the possible mechanisms in effect. For example, in a recent outdoor module rating study [21], low illumination conditions were forced by increasing the angle-of-incidence to the sun, with no consideration for the changes in reflection losses and incident spectrum this induces. The result was unfeasibly high efficiency under low light for the a-Si samples, when in fact this is likely to have been bolstered by improved spectral matching as the modules received a greater proportion of diffuse (blue) light. In a similar fashion, positive temperature coefficients for power have been reported for a-Si (e.g. [22]) when extracted from outdoor data. Since there is a strong correlation between temperature and incident irradiance and, under clear skies, between incident irradiance and blueness of the spectrum, the favourable change in spectrum can outweigh the weak negative effect of temperature on a-Si. Detailed data analysis carried out as part of this analysis has shown that due consideration of the spectral effect resolves such contradictory results [23].

When carefully applied, the results of modelling from different approaches can perform well, against one another and measured operational device data. Kroposki et al [24] neatly summarise and validate the culmination of developmental work on NREL's version of the RRC method and SNL's empirical approach against modules of seven different technologies.

Early investigations concluding the impact of spectral variation on PV performance as negligible were largely drawn on the basis of experiments focussed on crystalline silicon devices. This is now being challenged as the contribution that a-Si offers to cost reduction and the future potential of other wide band gap technologies is recognised. However, spectral effects are still not fully understood, especially in their relationship to other environmental factors, and there remains some confusion over the significance of the impact on energy production. A key assumption often made is that the fraction of energy delivered under non-clear skies is negligible. While this may be true for low latitude locations with small quantities of cloud, researchers enjoying less favourable climates have been quick to extol the virtues of PV in their non-ideal sites, where energy generated under cloudy skies is thought to make up a significant fraction of the

annual total. It is under these conditions where the largest deviations from the standard spectrum are observed.

3.2 Variation of PV Efficiency

With regard to the performance of photovoltaic devices, the impact of spectral variation is anticipated mostly in the photocurrent, since it alters the irradiance resource experienced by the device. Voltage variation may arise due to dependence on the current and the temperature of the device may also change (depending on spectral absorption), affecting parameters with a thermal dependence. This section aims to extract a quantification of these effects, to assess the significance of spectral variation on device performance relative to other environmental influences.

Four modules from the CREST outdoor testbed are analysed, one crystalline silicon (c-Si), one single-junction amorphous silicon (a-Si), one same-bandgap double-junction a-Si (a-Si 2j) and one triple-junction a-Si with a Germanium alloy bottom cell (a-Si 3j).

Figure 3.1 shows the seasonal variation of efficiency for the four modules and how this breaks down into short-circuit current response (I_{SC}/G), open-circuit voltage (V_{OC}) and fill-factor (FF). All parameters are presented as irradiance-weighted averages by month. This gives a better representation of the impact on energy generation and suppresses contributions from marginal situations of low irradiance where I_{SC}/G and efficiency can pivot rapidly due to increased thermopile error. To enable comparison of the different modules, all data are shown relative to the respective STC values. These values have been measured in a Spire flash tester, or extracted from the outdoor data in the case of the multi-junction devices, which are not suitable for short-pulse flash testing.

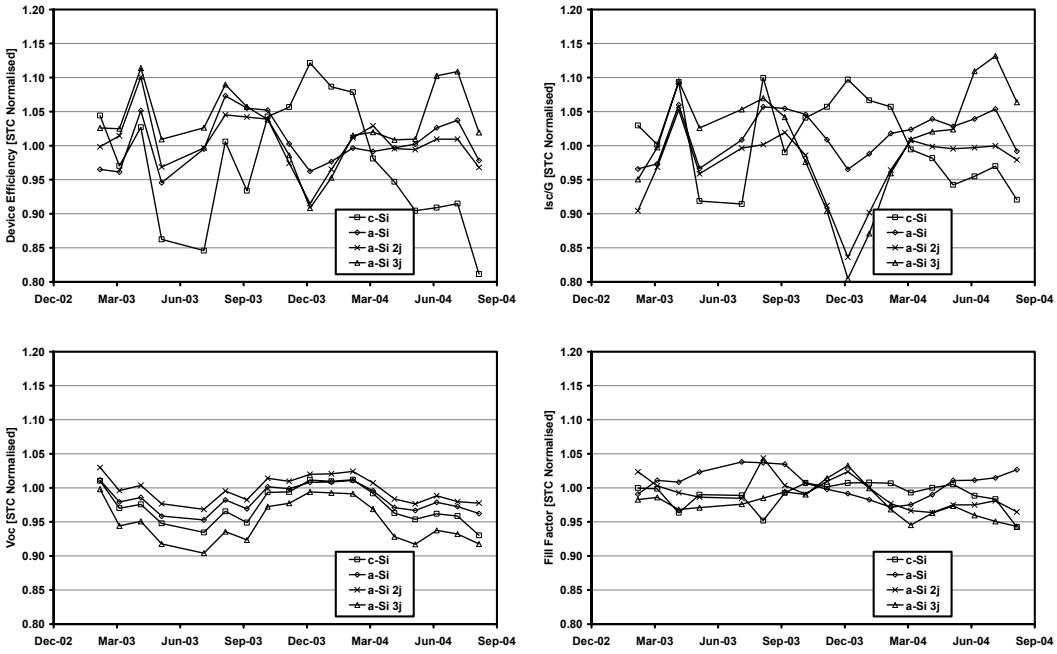

Figure 3.1: Seasonal variation of PV output (top-left to bottom-right: Efficiency, I_{SC}/G, V_{OC}, FF)

Neglecting the problems of the summer 2003 irradiance data (caused by low volume of data), there are clearly repeating seasonal patterns in all the device parameters. It is also apparent that the efficiency variation of the a-Si modules is underpinned predominantly by the I_{SC} and that of the c-Si module is further supported by V_{OC}. While the FF of the c-Si module does not exhibit a strong seasonal pattern, those of the a-Si modules do. However, that of the single-junction device is inverted with respect to the multi-junctions.

To assess the mechanisms in play for this variation to occur and to determine the root causes, it is necessary to consider the environmental parameters ultimately driving the device performance variation. These patterns correlate strongly with those of broadband irradiance (G), spectral variation (APE), module temperature (T_{MOD}) and solar angle of incidence (AoI), shown in Figure 3.2 with the same irradiance weighting as the device data, but no normalisation. The variation of temperature is similar for each module, so only that of the c-Si device is shown for clarity.

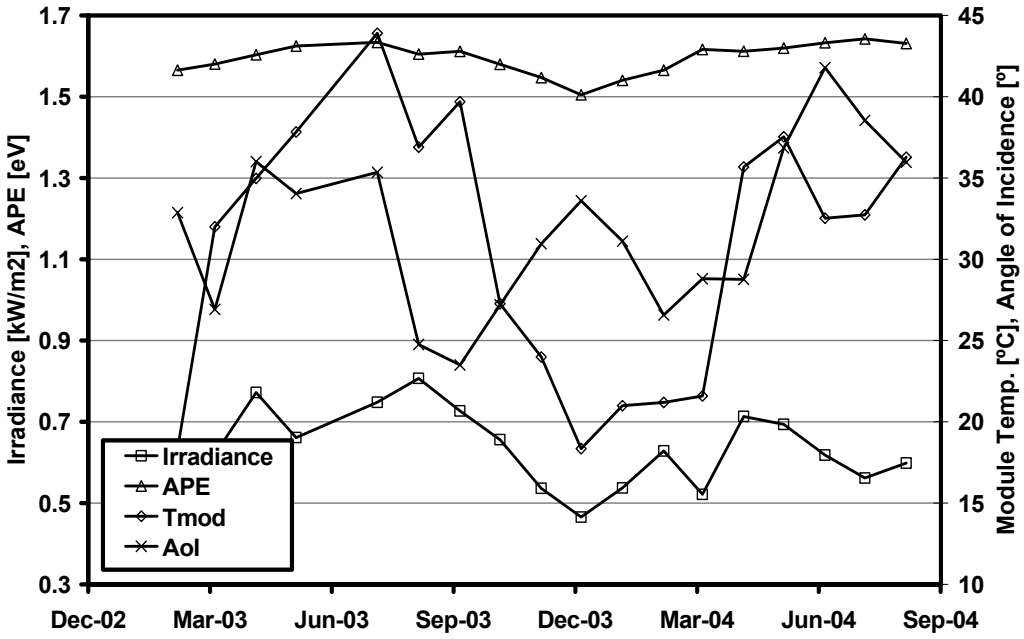

Figure 3.2: Seasonal variation of environmental parameters

Variation of all these drivers is set by the sun. Spectral blueness is determined primarily by solar geometry through the airmass, with secondary effects due to weather as discussed in chapter 2. The AoI follows a more complex pattern, since it is measured to an inclined plane. In winter the sun is lower in the sky than the rake of the system and in summer it is higher. Thus the minima in the irradiance-weighted AoI occur in spring and autumn, when the noontime solar elevation most closely matches the system pitch.

Module temperature is a strong function of irradiance, so both of these quantities also follow a pattern set by annual variation of solar geometry, but with a much greater dependence on weather than the APE. It should be noted that 2004 saw a summer that was poor even by British standards, hence the distortion to the usual pattern.

These environmental effects on relatively short timescales overlay a gradual trend in device degradation, applying to all the modules. Rapid degradation of a-Si modules in their first few months of outdoor exposure is not regarded in this thesis, save for the possibility of a seasonal pattern of recovery through annealing, discussed below. The a-Si modules included in this analysis have been operating for a substantial period of time and are considered to be fully stabilised.

The following sections aim to shed some light on the tangle of which environmental parameters influence which electrical parameters for which devices and to what extent.

3.2.1 Variation of Short-Circuit Current

The photocurrent (I_{PH}) is often approximated as the short-circuit current (I_{SC}), making the assumption that the device is sufficiently well constructed for parasitic resistances not to have too great an effect. The validity of this assumption depends on the PV material and production quality, but has been found reasonable for the four modules investigated here (see the following discussion). Since it is obvious that all other influences on the short-circuit current are secondary to the effect of exposing the device to more light, investigation of I_{SC} takes place through normalisation by broadband irradiance.

I_{SC}/G varies with any difference in linearity with irradiance between the device and the thermopile. Although the linearity error of the thermopile itself is given by the manufacturer and is low (chapter 2), errors introduced in the signal amplification become more significant at low irradiances. However, this instrumentation effect is random so should be minimised through the binning technique employed in the following and is also mitigated through the applied irradiance weighting on the data presented.

The four drivers identified in Figure 3.2 all have the potential to influence the current response. They correlate strongly with each other on a monthly basis, but not necessarily instantaneously. Hence the investigation is based on raw measurements from the database, grouped by each environmental parameter.

Temperature Effects

Module temperature may affect the photocurrent in two ways: Through a change in absorption efficiency represented by an instantaneous temperature coefficient, or via material changes caused by annealing recovery of light-induced degradation. Temperature coefficients of I_{SC}, V_{OC} and P_{MPP} are generally given in module specification sheets, measured under STC irradiance and spectrum. I_{SC} typically increases by 0.06-0.1%/ºC under these conditions (this is the range for the modules presented here). Hence, given the variation in module temperature in Figure 3.2, one

could expect a summer I_{SC} enhancement of 1.1-1.8% and a winter reduction of 0.4-0.7% due to this effect.

A common representation of I_{SC}, accommodating first-order irradiance and temperature effects, can be used to perform a correction based on the temperature coefficient:

$$I_{SC} = G \times \left[\frac{I_{SC}|_{STC}}{G|_{STC}} + \alpha_{ISC} \left(T_{MOD} - T_{MOD}|_{STC} \right) \right] \tag{3.7}$$

where G is the irradiance, T_{MOD} is the module temperature, α_{ISC} is the temperature coefficient of I_{SC} and the *STC* subscript denotes values at standard test conditions.

The current response of each module has been averaged with irradiance weighting in bins of temperature and is plotted in the left hand graph of Figure 3.3. The frequency distribution of the bin data count is also shown. The current response data with the application of the temperature correction of equation (3.7) is plotted in the right hand figure.

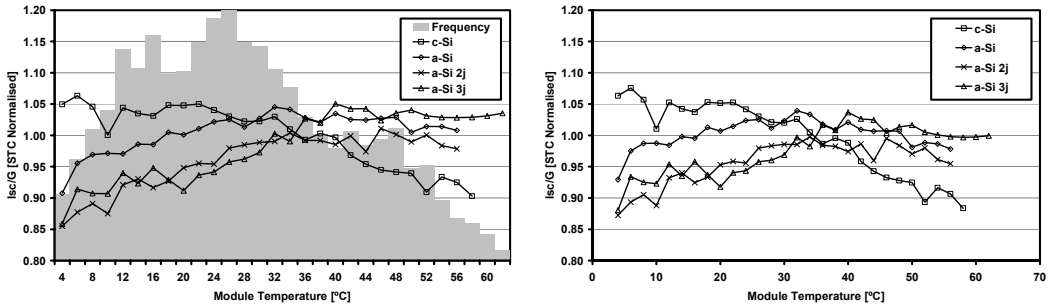

Figure 3.3: Current response variation with module temperature (temperature correction on right)

From this presentation of the data, all the modules appear to exhibit a non-linear dependence on the temperature. While the linear correction reduces the overall variation for the a-Si modules, the c-Si device displays a negative trend, which is then steepened.

The fundamental difference between the data used to fit temperature coefficients and that of Figure 3.3 is that the latter are taken from under much more varied conditions than the former. If there were only a temperature effect acting on the devices, this

procedure would correct all the data to a constant value (the STC current response). With additional environmental drivers included, the performance departs from expectation and is clearly not accounted for simply by the temperature coefficient correction. However, this method is the usual extent of present day performance evaluation methods employed for energy yield prediction.

By hypothesising additional mechanisms at work and testing them through analysis of this dataset, it should be possible to determine the ingredients of the mix and their proportions with greater certainty.

One such mechanism relating to temperature is a seasonal degradation/annealing pattern in a-Si module performance. It has been reported that reversal of light-induced degradation may occur at module temperatures as low as 40°C [25]. Controlled light soaking of several a-Si modules in cycles of cool (~24°C) and warm (~48°C) phases showed losses in I_{SC} of between 0.4 and 3% relative and subsequent recovery under heating to pre-soak values. Similar devices to the a-Si modules analysed in this thesis were included in the annealing study. Since the UK environment does not apply the same intensity of light soaking or lead to substantial time at even these relatively low module annealing temperatures, it is reasonable to take these values as the maximum extent of any degradation/annealing effect likely to be observed in the CREST measurement data. Furthermore, such patterns occur on longer timescales than will make visible in the raw data the relatively small impact on the current response. The distribution of module temperatures for the dataset (which includes two summers) shown on the left of Figure 3.3 also demonstrates that annealing would have to take place at even lower temperatures than this if it is to significantly affect the performance of PV in the UK midlands. As a result, there is no clear evidence for this effect in Figure 3.3.

Irradiance Effects

Aside from scaling PV device output as the available resource increases, variations in the level of irradiance can affect I_{SC} through influence of the parasitic resistances. Under short-circuit conditions (from the 1-diode model):

$$I_{SC} \approx I_{photo}\left(1-\frac{R_S}{R_{SH}}\right) \tag{3.8}$$

where I_{photo} is the photocurrent and R_S and R_{SH} are the series and shunt resistances, respectively. Both resistances are functions of irradiance, but for high-quality devices, their ratio is much less than unity under all conditions. 'Shunty' devices may suffer an increase in the R_S/R_{SH} ratio under low irradiance, while for others this ratio may have a strong, positive dependence on irradiance and be affected at higher light levels, with a knock-on effect in the current response.

The parasitic resistances have been extracted from the gradient of measured outdoor I-V characteristics at short-circuit and open-circuit points and their ratio investigated for low and high irradiance conditions. The worst-case figures for the four modules analysed here are current losses at low irradiance (50 Wm^{-2}) of 0.15% (c-Si), 1.5% (a-Si), 0.5% (a-Si 2j) and 2.5% (a-Si 3j) and at higher irradiances (~1000 Wm^{-2}) of 0.05% (c-Si), 0.5% (a-Si), 0.3% (a-Si 2j) and 0.8% (a-Si 3j).

Figure 3.4 shows the current response binned by irradiance. The temperature correction of the previous section has been applied.

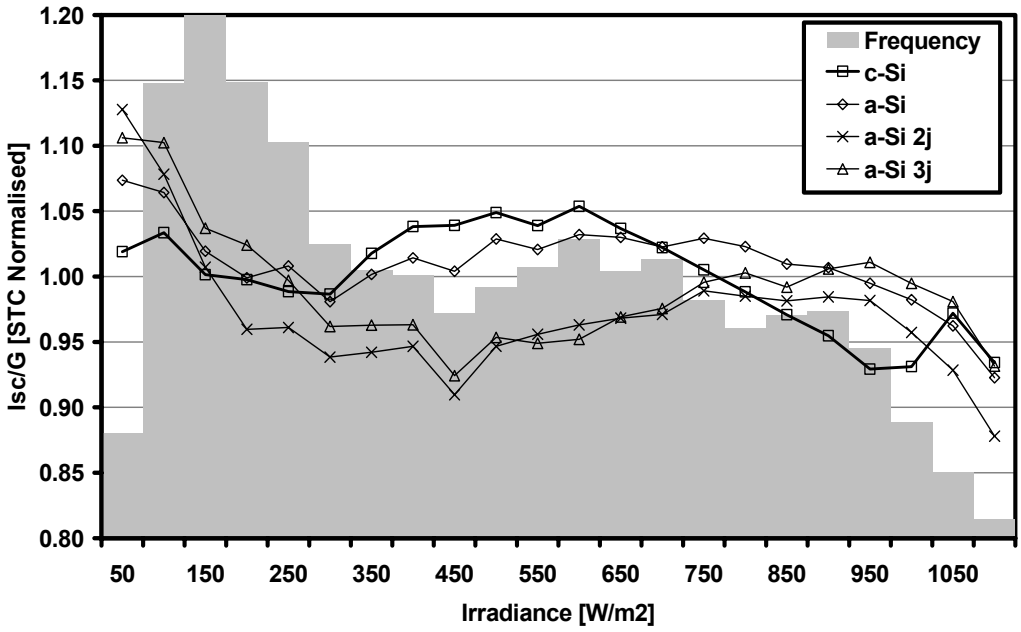

Figure 3.4: Temperature-corrected current response variation with irradiance

The complexity of Figure 3.4 cannot be explained by mechanisms relating only to broadband irradiance. Decreases in current response of the order discussed above may be present at the low and high irradiance extremes, but are dwarfed by much larger effects from some other cause. These other effects seem to have some correlation with irradiance however, pulling the current response up for all devices at low irradiance and acting in a device-specific fashion in the mid-range.

Angle of Incidence Effects

AoI may influence the current response via the increased cosine response error of PV modules compared to the domed thermopile pyranometer. CREST presently has no facilities for measuring module reflection losses in a systematic way[†]. However, published data from other research bodies (e.g. [18]) have shown only small reflection losses for angles of incidence below 60˚, before an increasingly rapid collapse in the current response ratio at steep AoI (typically 5% at 60˚, 10% at 70˚, 20% at 80˚). As noted in chapter 2, AoI has a weak effect on the spectrum also, due to the balance of beam and diffuse irradiance.

The current response binned by angle of incidence is presented in Figure 3.5, again corrected for temperature:

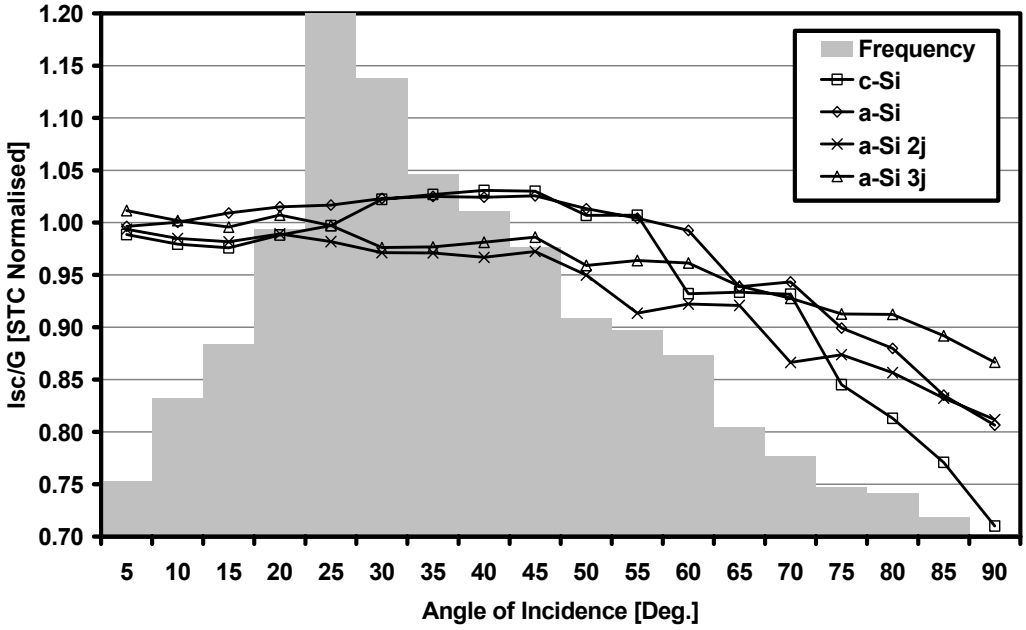

Figure 3.5: Temperature-corrected current response variation with angle of incidence

[†] There is current PhD research in this area at CREST however and such facilities are under construction. Results are due for thesis publication in 2006 by Sheryl Williams.

Although steep AoI coincide with low irradiance incident on the measurement plane, the implication from Figure 3.4 is that these conditions act to increase I_{SC}/G, not reduce it as observed in Figure 3.5. However, the frequency distribution shows that situations where the AoI exceeds 60˚ are relatively rare, while conditions of low irradiance (by whatever cause) are rather common. It is thus believed that irradiance (and hence temperature) are not so strongly correlated with AoI on an instantaneous basis. The effect of AoI on the spectrum was found to be very weak compared to other influences in the investigation in chapter 2. This is supported by the results of Figure 3.5, in which optical effects of the module conceal any evidence for such a weak spectral effect on the current response. Instead, the CREST data confirms the expectations of reflection calculation from the literature (e.g. [26]) for certain module types (although the effect on the c-Si module is rather large).

Spectral Effects

Thermopile pyranometers respond to such a broad band of radiation so uniformly that their output can be considered unaffected by spectral variation (Figure 3.6). The I_{SC} of a PV device however is a direct representation of the matching of spectral irradiance resource to the device spectral response. With all other influences constant, spectrum-induced variation in I_{SC}/G should be observable when the denominator is a spectrally insensitive broadband irradiance measurement. Scaling by any other irradiance measurement (e.g.: a silicon-based pyranometer) will show an enhanced or weakened spectral effect, depending on the relative spectral sensitivities of test module and detector [1], [27].

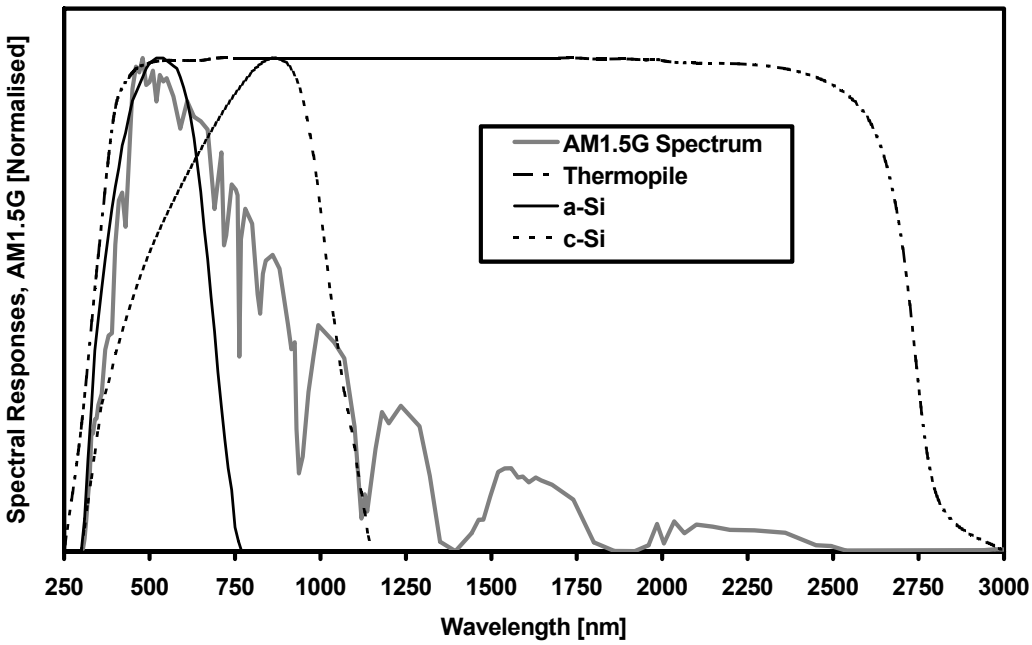

Figure 3.6: Thermopile pyranometer, a-Si and c-Si spectral response with respect to the AM1.5G standard spectrum

From Figure 3.6 and recalling that average photon energy is a measure of the blueness of the spectrum, one could expect that a higher APE would benefit those PV devices with a high band gap and so absorb exclusively in the blue. Lower band gap materials are not expected to be so sensitive to the spectrum, since they have a wider spectral response. Two-terminal multi-junction devices, consisting of stacks of series-connected junctions, are current-limited by the sub-cell with the lowest photogeneration. It is thus anticipated that such devices will have a peak current response under the spectrum where the sub-cell currents are best matched and exhibit the highest spectral sensitivity among the devices.

Most of these theoretical predictions are demonstrated in the results of Figure 3.7, showing the temperature-corrected current response of the four test modules binned by APE and normalised to their respective STC values.

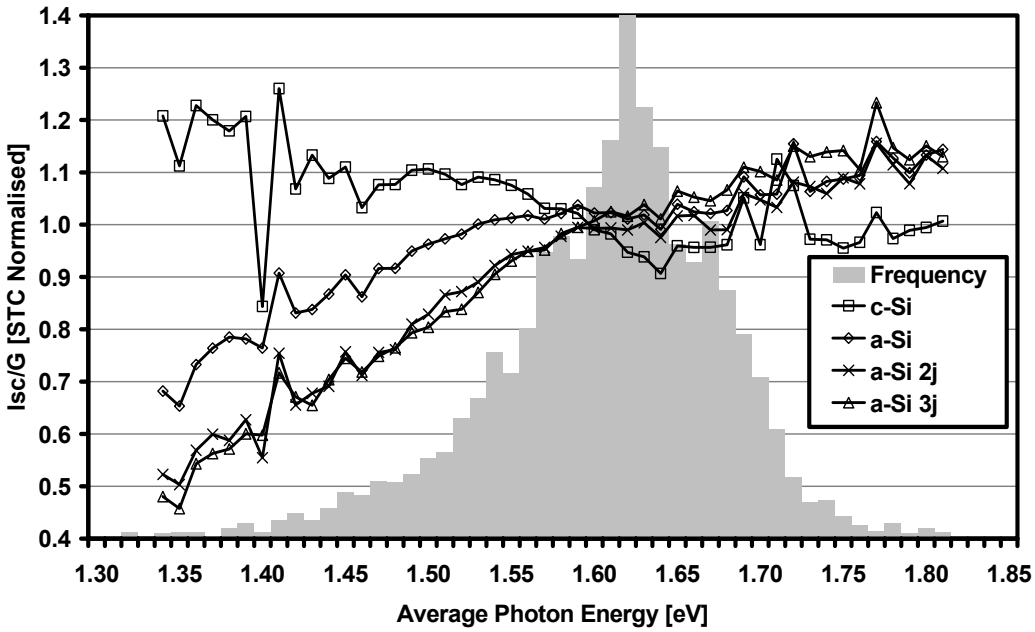

Figure 3.7: Temperature-corrected current response variation with average photon energy

The response curves in the above figure define two distinct regions above and below an APE of 1.64eV. This is the upper limit of APE seen under clear skies in Loughborough – data to the right are from cloudy conditions. The change in the relationship between current response and APE in these two regions is largely due to the simplification of using the APE to represent the spectrum. As explored in chapter 4, clear- and cloudy-sky spectra are quite different and this is not wholly contained within the APE measure.

Contrary to the assumption that bluer spectra will benefit PV devices, the current response of the c-Si module displays a negative trend with increasing APE up to 1.64 eV. The reason for this may lie in the detail of the spectral response curve. The curve for this actual module is unknown, but c-Si SR curves from the literature show there is considerable variation between modules (Figure 3.8, left).

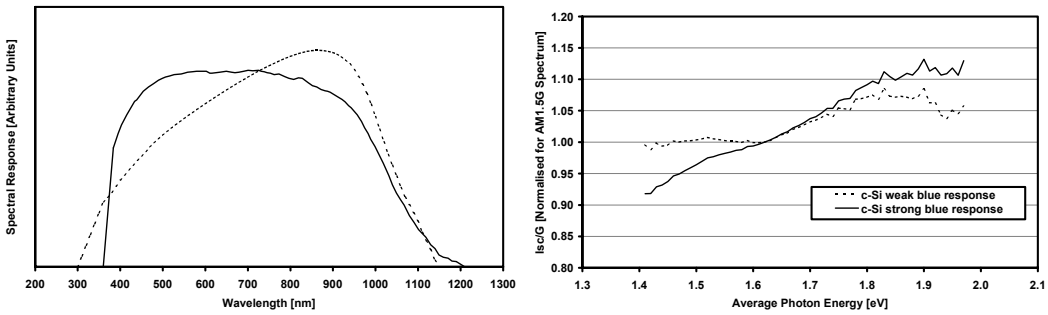

Figure 3.8: Published spectral response curves for different c-Si modules (left) and the effect on sensitivity to the spectrum (right)

For a module with a weak response to blue light, such as the module with the dashed curve above, it would be quite feasible for the highest current response to occur under a redder spectrum than for the other example shown. The right hand figure supports this hypothesis. It shows the relative current responses of two modules with the SR curves shown on the left, simulated by the product of each spectral response curve and measured spectra - a technique discussed in more detail in chapter 5. From the results of Figure 3.7 and the right hand of Figure 3.8, the c-Si module analysed would have a weaker blue response than either of the SR curves of the left of Figure 3.8, yet this appears to be a plausible explanation of the trend seen for the c-Si module.

The current response of the single-junction a-Si module behaves exactly as expected from the spectral matching model encapsulated in equation (3.1), with reference to the a-Si spectral response (SR) curve in Figure 3.6 and the measured spectra under extremes of APE from Figure 2.8. It should be noted that the SR curve depicted is not that of the single-junction module in this analysis, which is unfortunately not available or measurable at CREST, yet the graphic is indicative for the technology.

The anticipated peak in I_{SC}/G for the multi-junction modules was not observed. The understanding that such devices spend a proportion of their operating life with a current mismatch between the sub-cells, with current response peaking under some spectrum where they are matched, appears to be flawed. The reality, at least for the two modules considered here, seems to be that the sub-cell currents are *never* matched in normal operation in the UK. Both the devices are continuously limited by the current from the top cell (absorbing in the blue). This has been confirmed by the manufacturer of the triple-junction module and can be seen in the sub-cell spectral response curves of both multi-junction devices (which were obtained in confidence and thus not presented in

this work). The result is that these modules do not have a greater sensitivity to the spectrum caused by sub-cell mismatch, yet increased sensitivity relative to the single-junction a-Si device is still observed. This is due instead to the narrower spectral response of the multi-junction device top cells relative to the single-junction. Similarly, the triple-junction device can be seen to be more sensitive than the double-junction, because the a-Si 3j top cell spectral response is narrower than that of the a-Si 2j device.

The influence of the spectrum is also the only forthcoming explanation for the mystery features of Figure 3.3 and Figure 3.4 of the previous sections on temperature and irradiance effects. The lower irradiances of Figure 3.4 correspond to one or both of two conditions: cloudy skies and situations of low solar elevation. In chapter 2, it was shown that clouds act to skew the spectrum to the blue. This improves the matching to the spectral response of the high band gap devices and the current response increases. High airmass has the opposite effect. The data of Figure 3.4 have been separated by airmass-corrected clearness index (equations (2.6) and (2.7) from chapter 2) into a cloudy-sky and a clear-sky group and plotted in Figure 3.9 on the left and right, respectively.

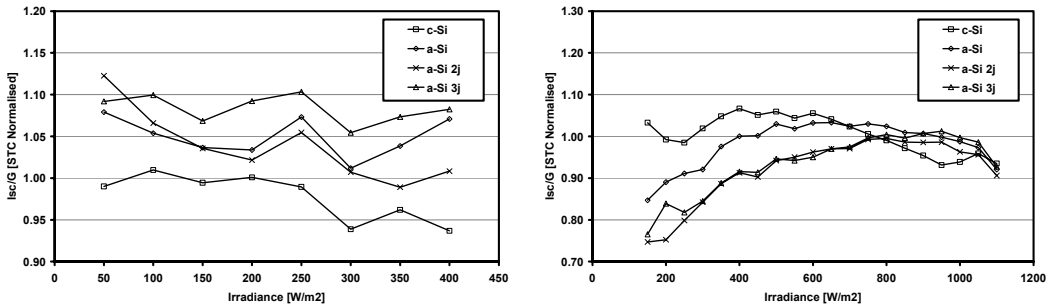

Figure 3.9: I_{SC}/G dependence on irradiance for cloudy skies (left) and clear skies (right)

This clearly shows the bulk of the non-linearity of the a-Si modules' I_{SC}/G with irradiance is caused by the spectral effect and also accounts for some of the behaviour of the c-Si module. Figure 3.10 confirms the same relationship between APE and irradiance under clear and cloudy conditions (module temperature dependence is shown for comparison).

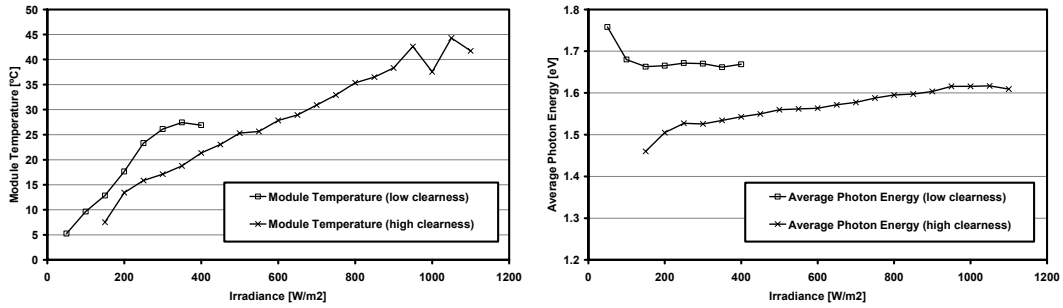

Figure 3.10: Correlation between module temperature and irradiance (left) and average photon energy and irradiance (right) for clear and cloudy skies

The decrease in current response at very high irradiance has not been explained by the discussion of the spectrum thus far. Although a small dip in this parameter is observed in Figure 3.10, it is not enough to account for the reduction in I_{SC}/G. Neither is light-induced degradation a likely candidate, since this is a relatively slow process and the high irradiance conditions in question are concurrent with mitigating high module temperatures.

A possible cause is found with the spectrum, but in this case the drop in current response would be caused by the spectrum having become so blue-shifted that the point of optimal match to the device spectral response is passed right through, as hypothesised for the c-Si module. This may seem contradictory to the previous conclusion about cloudy-sky spectra having a higher APE than the bluest clear-sky case and the observed continuing increase in I_{SC}/G under cloudy conditions. However, increase in the APE occurs in different ways for clear and cloudy conditions. For clear skies, the peak in the spectrum shifts to shorter wavelengths as the airmass decreases and the spectrum becomes more blue. Although this is also true under cloudy skies, the cloud attenuation is the dominant factor. As the overall broadband irradiance is reduced by cloud, the long wavelength tail of the beam spectrum is completely suppressed and the spectrum becomes less red, increasing the APE without shifting the peak to shorter wavelengths.

The spectral effect on the current response can be summarised as follows. Under clear skies, the airmass effect reduces I_{SC}/G by 0% (c-Si), 10% (a-Si), 20% (a-Si 2j, a-Si 3j) at 200 Wm^{-2} (1.50 eV APE), with all values relative to each module's STC performance. At 500 Wm^{-2} (1.56 eV) these figures have improved to *increases* of 5% and 3% for c-Si and a-Si, respectively and losses of 5% for the multi-junctions.

Between 800 and 1000 Wm^{-2} (1.59-1.62 eV) all the a-Si modules perform at or near their rated capacity as the c-Si module suffers losses of 0-7%. At the highest irradiances up to 1100 Wm^{-2} (1.62 eV), all modules supply 90-95% of their STC current response.

Under cloudy skies, between irradiances of 50 and 400 Wm^{-2} (1.76-1.67 eV APE) there are current response losses of 0-5% for c-Si, and gains of 2-7% (a-Si), 0-10% (a-Si 2j) and 6-10% (a-Si 3j) for the other modules, relative to the STC values.

I_{SC}/G dependence on APE is more or less linear for cloudy conditions, but not for clear skies. This complicates parameterisation for spectral correction, an issue which shall be addressed in the following section on efficiency and in more depth in chapter 5.

Figure 3.11 shows the a-Si device I_{SC}/G seasonal variation in comparison to the primary influences: spectrum, irradiance and module temperature (in that order).

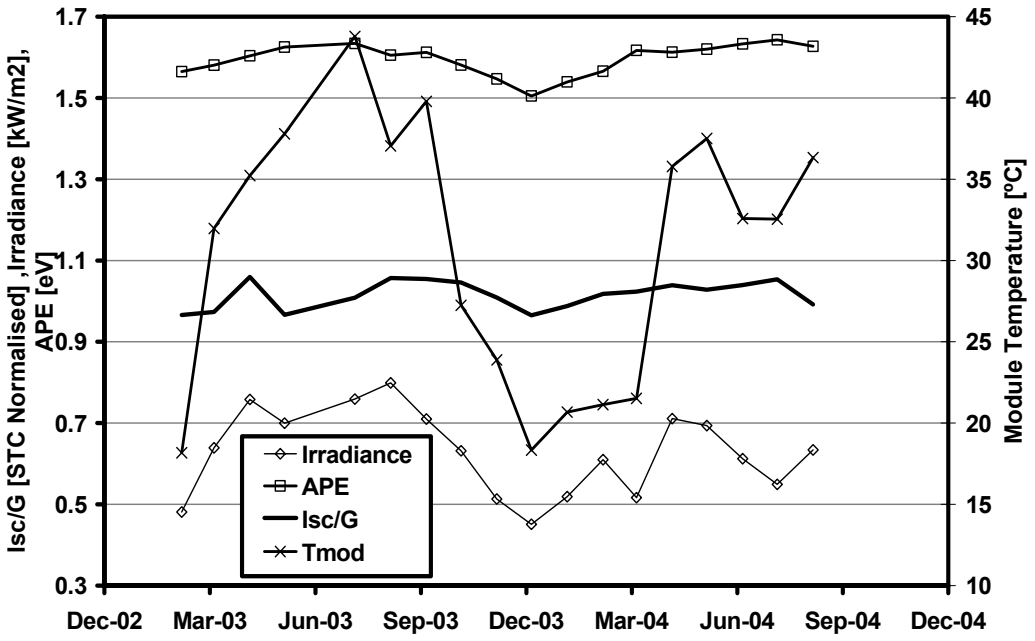

Figure 3.11: Current response of the a-Si module with the main influences of variation

3.2.2 Spectral Influence on Other Device Parameters

Open-circuit Voltage

The spectrum is not expected to affect the V_{OC} directly to a great extent, but indirectly through the logarithmic dependence on I_{SC}. Temperature is well known to be the biggest effect on voltage and this is seen in the top-left graph of Figure 3.12. The correction

based on the V_{OC} temperature coefficient of the manufacturer is shown in the top-right graph and is applied throughout. The results for all four modules meet the expectations for the influence of irradiance and angle of incidence.

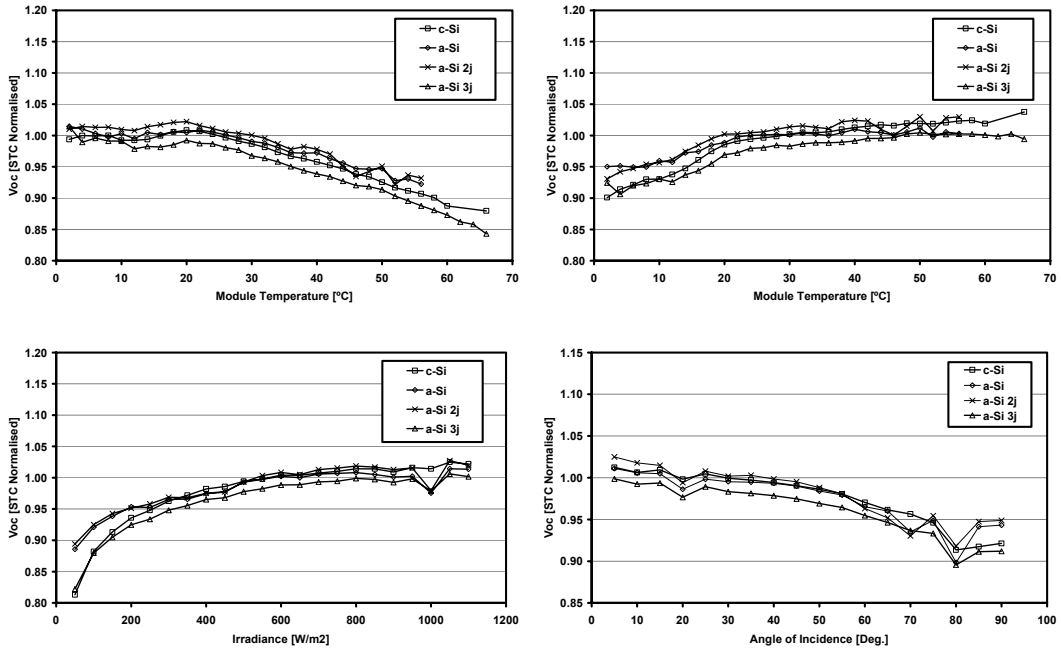

Figure 3.12: Environmental effects on open-circuit voltage (top-left to bottom-right: Temperature, Temperature with correction, Irradiance, Angle of Incidence)

Figure 3.13 shows the V_{OC} plotted against average photon energy. The most noticeable feature is the discontinuity between bright, clear-sky conditions and cloudy skies at around 1.64eV. This is to be expected however, as the V_{OC} is not normalised by irradiance as the I_{SC} was in the previous section. The apparent increase in V_{OC} with APE under clear skies and decrease under cloudy conditions is the result of following the I_{SC} change with irradiance, correlated positively and negatively with the APE in these two regimes (from Figure 3.10).

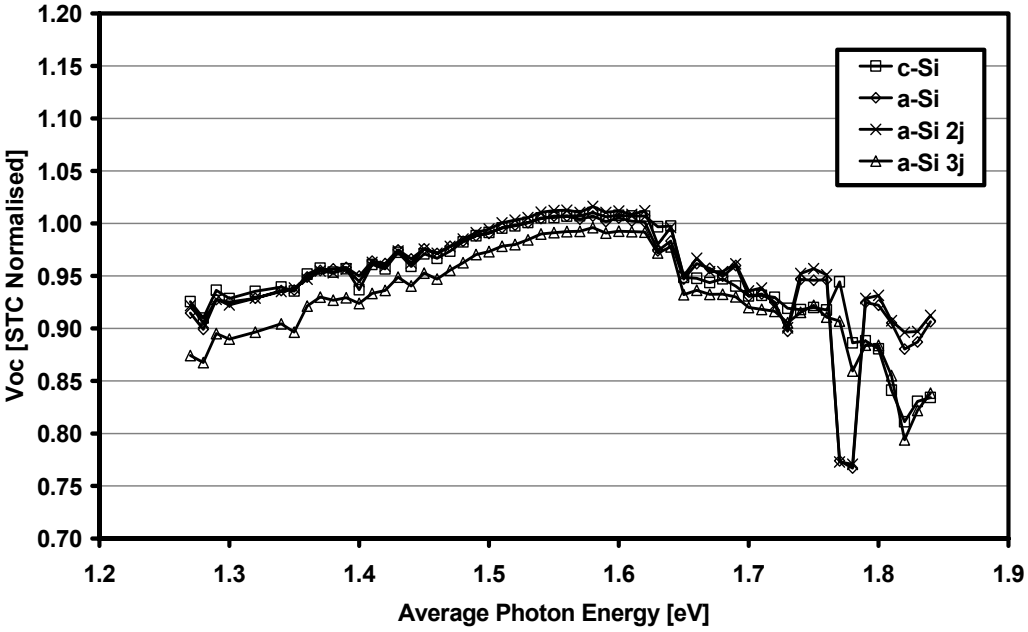

Figure 3.13: The relation of open-circuit voltage to Average Photon Energy

Fill Factor

The fill factor of a photovoltaic device is defined by four measurable/extractable electrical parameters:

$$FF = \frac{I_{MPP} \times V_{MPP}}{I_{SC} \times V_{OC}} \tag{3.9}$$

where I_{MPP} and V_{MPP} are the current and voltage at maximum power point.

The maximum-power current and voltage have a much greater dependence on PV material and specific module build quality than I_{SC} and V_{OC}. Series and shunt resistances play a large role in determining the shape of the I-V characteristic and as discussed previously, are also functions of irradiance. This makes it extremely difficult to generalise environmental effects on the fill factor. Nonetheless, previous research into the matter has covered many different types of PV device over the years and it is possible to expect certain trends in the CREST data from the body of published literature.

Figure 3.14 shows the observed variation of fill factor with operating environment. Angle of incidence has been excluded since no visible trend is in evidence. With the

exception of the temperature dependence in the top left of the figure, all values have been temperature-corrected through the underlying parameters of equation (3.9).

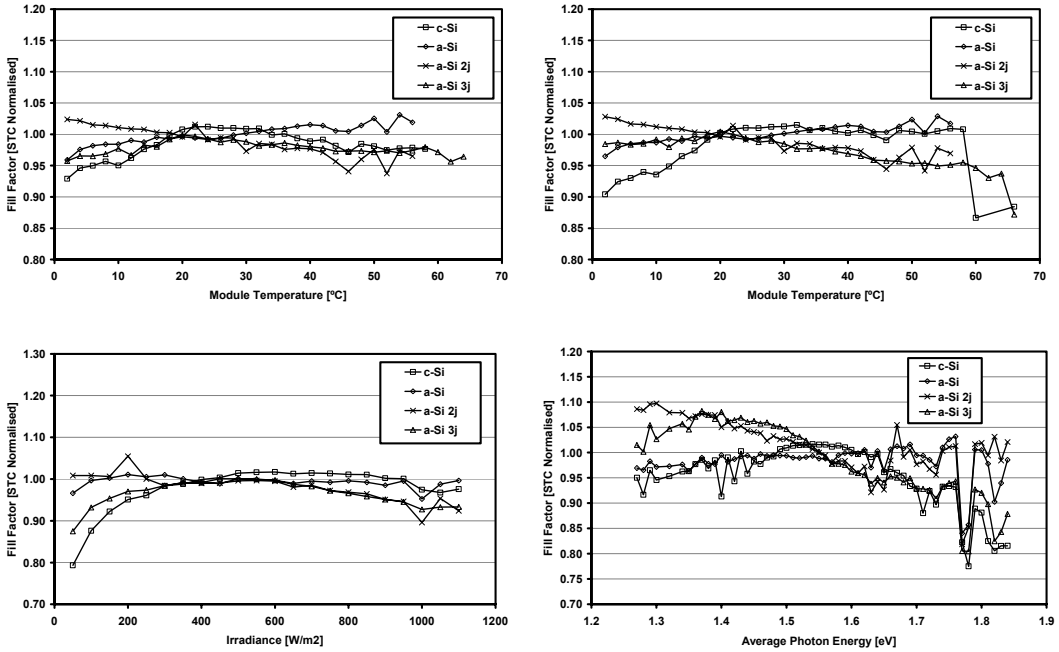

Figure 3.14: Environmental effects on fill factor (top-left to bottom-right: Temperature, Temperature with Correction, Irradiance, Average Photon Energy)

The picture that Figure 3.14 gives is a confusing one, in that there are features hinting at general patterns while also making clear there are significant differences between the modules. With the exception of the a-Si double-junction, the FF decreases under low irradiance/temperature, with the multi-junction devices also suffering at high irradiance/temperature. It has been reported that multi-junction devices exhibit an increase in the fill factor when the sub-cell currents are mismatched and this is observed in the CREST data also, where both the double- and triple-junction module FF are highest under rather red spectra.

To elucidate the influence on the fill factor, the effects on the I_{MPP}/I_{SC} and V_{MPP}/V_{OC} ratios have been separated. It was thus found that the spectrum has no direct influence on either ratio, or indeed the fill factor. The shape of the curves in the bottom right graph of Figure 3.14 arises only because of the correlations between APE, irradiance and module temperature under clear- and cloudy-sky conditions. Furthermore, it is believed that temperature affects V_{MPP} and V_{OC} to the same degree and thus does not largely influence their ratio and similarly for I_{MPP}/I_{SC}.

It was found instead that the influence of irradiance alone is sufficient to account for the variation seen in the current and voltage ratios and this is presented in Figure 3.15.

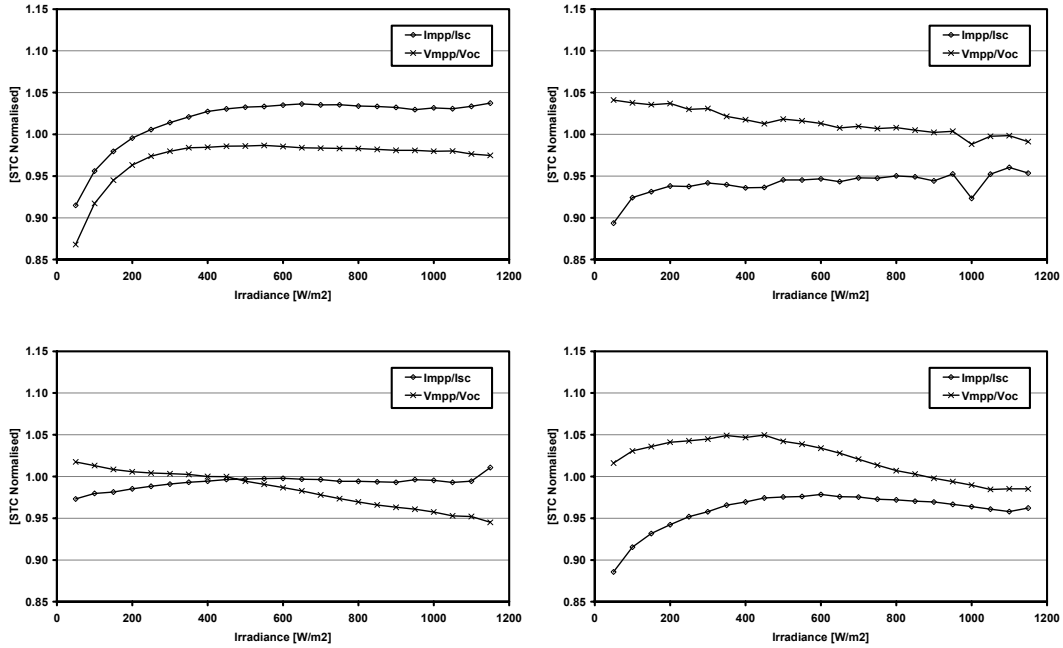

Figure 3.15: Influence of irradiance on I_{MPP}/I_{SC} and V_{MPP}/V_{OC} ratios for (top-left to bottom-right): c-Si, a-Si single-junction, a-Si double-junction, a-Si triple-junction

Under low light levels, I_{MPP}/I_{SC} decreases exponentially as irradiance reduces. This happens to all modules as the photocurrent reduces and the difference between I_{SC} and I_{MPP} becomes comparable to the magnitude of I_{SC}. The rate at which this collapse happens is set predominantly by the shunt resistance R_P, since this largely determines I_{SC}-I_{MPP}.

The particular c-Si device used for this analysis has a rather high R_S, compared to other commercial c-Si modules and the I_{MPP}/I_{SC} ratio can be seen to suffer. Multi-junction devices generally have a high R_S compared to single-junctions because of their structure. As a result, the triple-junction module exhibits a similar drop in the current ratio. It is believed the double-junction device withstands this because of shunt resistance enhancement specifically carried out in the production by the manufacturer. No production details are available for the single-junction a-Si module, but parasitic resistance values extracted from outdoor measurements confirm this to be a well-constructed module. The V_{MPP}/V_{OC} ratio also degrades for the low-shunt resistance modules.

At higher light levels, the series resistance increases with irradiance for all the modules. Since the open-voltage is almost static for higher irradiances, a reduction in V_{MPP}/V_{OC} is observed.

In summary, the spectrum only affects the fill factor insofar as it influences the short-circuit current, but the impact on this parameter on an absolute scale is overshadowed by the broadband irradiance.

Efficiency

In terms of the electrical parameters discussed and the area A, the efficiency of a PV module can be expressed:

$$\eta = \frac{(I_{SC}/G) \times V_{OC} \times FF}{A} \tag{3.10}$$

It follows from this and the preceding discussion that the spectrum influences device efficiency almost exclusively through the short-circuit current response, resulting in the same sensitivity to APE.

To evaluate the effect of spectrum-driven efficiency change on energy yield, the spectral effect must be corrected for. Although not linear such as the temperature correction, a second- or third-order polynomial function instead can fit the I_{SC}/G dependence on APE reasonably well and be used in a similar way. This has been carried out for the four modules and a spectrum-corrected power output calculated. Considering the instantaneous power output to represent the average for each ten-minute measurement interval, sums of energy are built on a monthly and annual basis for the measured power and that calculated with the spectral correction to AM1.5G. The ratio of these sums yields the spectral effect on energy production over the timescale, *t*:

$$\eta_{Spec}(t) = \frac{\sum_t \left(I_{SC}^{meas} \times V_{OC}^{meas} \times FF^{meas} \right)}{\sum_t \left((I_{SC}/G)^{SpecCorrection} \times G^{meas} \times V_{OC}^{meas} \times FF^{meas} \right)} \tag{3.11}$$

For the year September 2003 to August 2004, η_{SPEC} yields increases of 1% for the c-Si and a-Si modules, due to spectral effect and losses of 6% and 3% for the a-Si double-

and triple-junction devices. The seasonal pattern of the spectral impact on energy generation is shown in Figure 3.16.

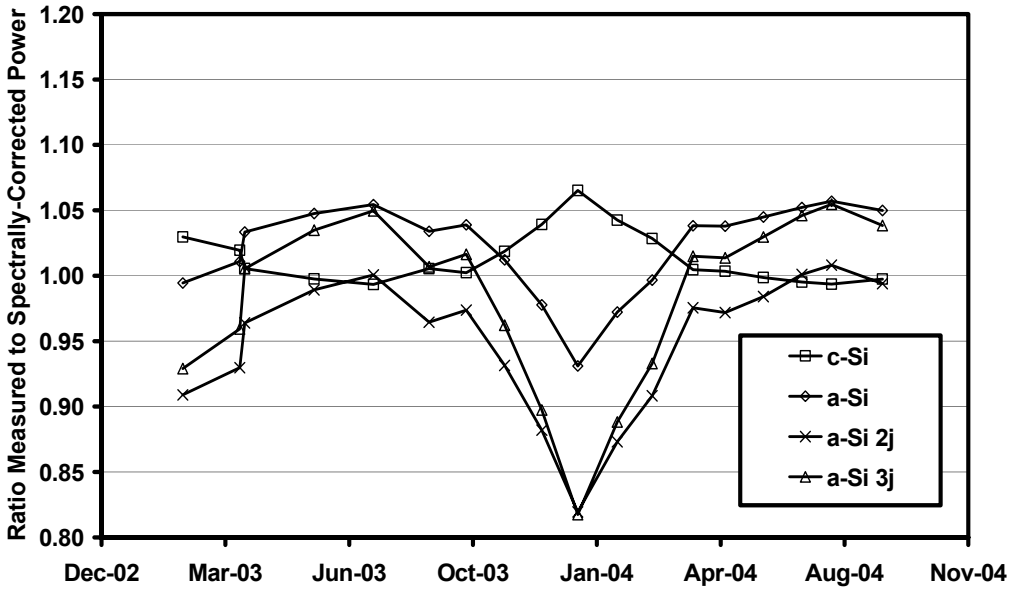

Figure 3.16: Seasonal spectral effect on energy yield

3.3 Conclusions

The largest obstacle to the analysis of environmental effects on PV device performance from outdoor data is the difficulty of their separation. Filtering of data to isolate the different influences has the effect of distorting the dataset because of the strong correlation between the various drivers. Supporting indoor measurements might be a way forward, but regarding the spectral effect these are not possible at the module level within reasonable cost boundaries. The method used here has been to present a case of evidence by cutting the data along different axes while preserving the integrity of the set.

It has thus been demonstrated that variation in the solar irradiance spectrum has no direct influence on the open-circuit voltage or fill factor of the module types tested here. The impact of the spectrum falls entirely on the short-circuit current and the effects propagated just so to the efficiency. These effects are summarised in Table 3.1.

Module	Clear Skies, High Airmass (1.50 eV)	Clear Skies, Mid Airmass (1.56 eV)	Clear Skies, Low Airmass (1.59-1.62 eV)	Clear Skies, Low Airmass (1.62+ eV)	Cloudy Skies (1.67-1.76 eV)
c-Si	0%	+6%	0%	-1%	+0-5%
a-Si	-10%	+3%	0%	-7%	+2-7%
a-Si 2j	-20%	-5%	0%	-8%	+0-10%
a-Si 3j	-20%	-5%	0%	-6%	+6-10%

Table 3.1: Sensitivity of efficiency to different spectral conditions (relative to STC efficiency)

Given the spectral environment of the UK discussed in chapter 2, the spectral effect has been shown to affect seasonal energy yield from the different modules with summer/winter enhancements of -1/+7% (c-Si), +5/-7% (a-Si), +1/-18% (a-Si 2j) and +5/-18% (a-Si 3j). This compares with a summer/winter temperature enhancement of +2/-1% for all modules.

4 Spectral Irradiance Modelling under Realistic Skies

A spectral influence on the efficiency, and hence energy yield, of PV systems has been predicted and demonstrated experimentally in the previous chapter as well as by a number of researchers. The magnitude of these effects depends on location and PV module technology, so while of little interest to some, for others it is crucial for accurate system sizing, yield and cost calculations. As technologies with increased spectral sensitivity such as interconnected multi-junction devices and concentrators become more commonplace, there will be even greater need to account for spectral irradiance variation. It is unlikely that this need will be met through widespread measurement systems because of cost and practicality considerations.

This chapter reviews the historical development of spectral irradiance modelling, which has focused almost exclusively on clear sky conditions, before presenting an empirical extension to account for less favourable climates.

4.1 Overview of spectral irradiance modelling for clear skies

A range of modelling techniques has been applied to describe the spectral distribution of irradiance, varying widely in complexity. At the simpler end are those based on empirical fits of small numbers of parameters from measured spectral irradiance data, such as by Crommelynck & Joukoff [28]. Here the spectrum is roughly approximated as a triangular form, with spectral irradiance rising from zero at 300 nm to an apex located at a fixed wavelength (465 nm) and falling again to zero at another fixed wavelength (1189 nm). The wavelength for the spectral maximum was selected as generally representative of the observed measured spectra over one year at the test site (Uccle, Belgium), i.e. valid for all conditions. However, pinning the spectral maximum to a fixed wavelength leads to a fixed relative spectral distribution. Hence this model is not an investigative tool for changes in the spectrum, but rather a first approximation for allowing consideration of the spectral distribution beyond a broadband irradiance value.

At the other extreme are models where each electron state transition due to interaction with radiation of every type of molecule found in the atmosphere is modelled individually. These models are very high resolution since the transmission of different wavelengths of radiation is calculated line-by-line, referring to the transition lines of which there are hundreds of thousands. Since the majority of spectral irradiance modelling work has been undertaken in the U.S., the only line-by-line model found in literature concerning photovoltaic applications is FASCODE, developed by their Air Force Geophysical Laboratory (AFGL) [29]. The transmission probabilities of each transition of each substance are taken from a database storing the results of laboratory experiments. The atmospheric abundance height profile of each substance is taken from a "standard atmosphere", defined through balloon and aircraft measurements at different altitudes. The result is the spectral transmission between the top and bottom of the atmosphere. Combined with a top-of-atmosphere (extra-terrestrial) spectrum as input, this yields the ground-level beam irradiance spectrum. FASCODE and the moderate and low resolution banded derivatives MODTRAN [30] and LOWTRAN [31] were developed primarily for remote sensing and do not model the propagation of diffuse irradiance. For most PV applications, this tends to negate the usefulness of the high accuracy transition data, especially considering the computational overhead involved.

In 1982, the Solar Energy Research Institute (later the National Renewable Energy Laboratory) in the U.S. used the Monte Carlo method to simulate clear-sky spectral irradiance with a model called BRITE and compared its performance with the then current version of LOWTRAN [32]. The beam spectral irradiance output of BRITE (which also used a multi-layer model of the atmosphere) compared favourably with the rigorous AFGL model. On this basis, coupled with the diffuse spectrum modelling ability lacking in LOWTRAN, it was BRITE simulations that formed the set of standard irradiance spectra used by the PV community until very recently. At the time of writing however, there are proposals to redefine the standard spectra through a new model (SMARTS, discussed below). This is because it has not been possible to reproduce the exact results of the original BRITE simulations since the software became obsolete some years ago.

The best compromise between simplicity and accuracy for engineering (and specifically PV) applications has been found with transmission models based on Bouguer's law:

$$T = \frac{I(x)}{I_0} = e^{(-kx)} \tag{4.1}$$

where I_0 is the incident irradiance and $I(x)$ is the irradiance at depth x into the atmosphere with an extinction coefficient k. Most such models are based on a single-layer representation of the atmosphere. Concentration height profiles of different gases are not generally known, instead they are assumed uniform in an atmosphere modelled as a single slab. Equation (4.1) is applied for different attenuation processes, each with its own extinction coefficient (a function of wavelength based on the absorption/scattering by different gases and particle size distributions) and the transmittances are multiplied to give the overall transmission fraction for each wavelength. This transmission is applied to an extra-terrestrial spectrum to yield the ground-level irradiance. The main difference between the following models is the choice of which absorption and scattering mechanisms to include and the data used for the extra-terrestrial spectrum and gas absorption coefficients – the availability of this data has developed over time as more advanced experiments have been carried out, yielding higher measurement accuracy and greater understanding of the atmosphere.

The earliest published attempt to model solar spectral radiation was performed by Moon [33]. This includes work to collect data sets and models on almost every pertinent aspect, from atmospheric absorption processes to the extra-terrestrial spectrum - many years before the first satellites were launched. Although the data from these early experiments now seem quite crude, Moon laid the foundation for a simple solar spectral radiation model for clear skies, which in essence is the same as that incorporated as the foundation in this work. Starting with an extra-terrestrial spectrum, he extracted from measured data the factors in Bouguer Law representations of attenuation by scattering (molecules, water vapour, and dust particles) and absorption (ozone and water vapour). The air mass was calculated as the secant of the zenith angle and the combined total resulted in a beam radiation model. This is shown in Figure 4.1, with the calculation also made by the source for the proposed new spectral irradiance standard for PV.

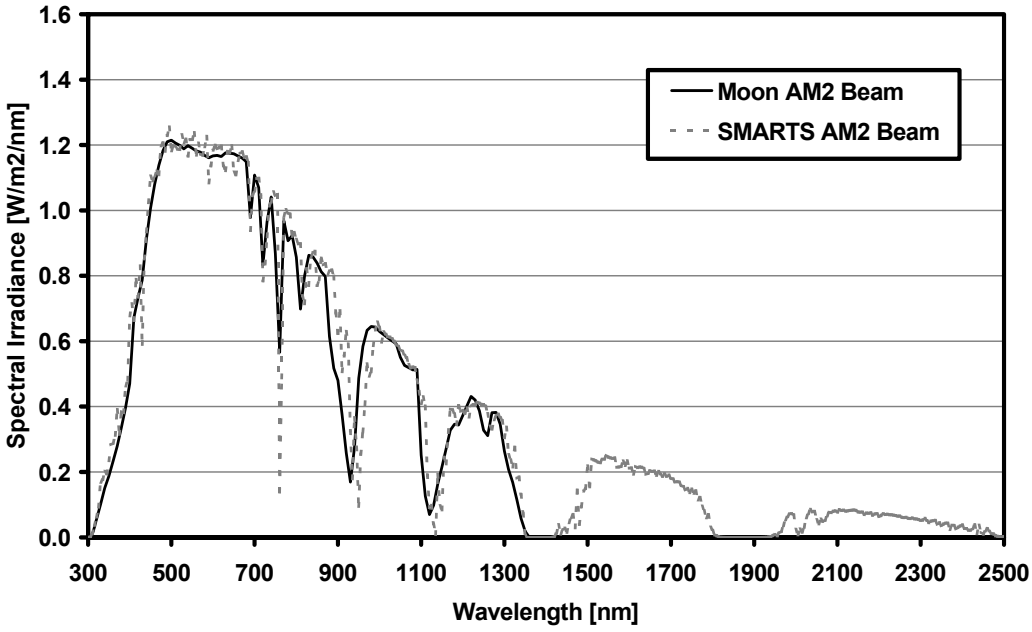

Figure 4.1: Comparison of Moon's 1940 beam spectral model and that generated by a modern code

25 years later, Gates [34] expanded Moon's original work to include advances in knowledge of the atmosphere and solar spectrum. Bouguer's Law was again employed to model various attenuation processes. Moon's molecular (Rayleigh) scattering term was retained, but the effects of water vapour and dust were combined into a single term for aerosol (Mie) scattering. The absorption by ozone term remained unchanged but that of water vapour was extended to include other gases such as carbon dioxide and other

less abundant, but still effective, atmospheric constituents. Data and expressions characterising the absorption and scattering terms was again pooled from observations made by several different workers. The greatest advance on Moon's work was to incorporate a diffuse irradiance model, which considered only molecular scattering, with some qualitative notes on the effect of ground albedo.

By the end of the Seventies, increasing numbers of research satellites and new terrestrial techniques were meeting the demand for more detailed knowledge of the atmosphere. Leckner [35] set himself the task of again updating the earlier spectral work and presents a complete set of functions, which he used in the first computerised solar spectral radiation model. He changed the structure of the beam model by separating water vapour from the absorption by other gases, allowing the input of varying moisture content in the air where previously it had been fixed to a single value. In addition, he introduced the use of Angstrom's power law relation for aerosol turbidity and gives an excellent overview of the problems encountered in atmospheric aerosol modelling. A diffuse model, similar to that of Gates but with a simplified mathematical expression, is included. It is based on the difference between the calculated beam radiation and the total radiation absorbed by gases, but ground albedo is excluded and the forward scattering fraction (discussed in the next section) is fixed independent of zenith angle.

Hatfield et al [36] further developed the Rayleigh scattering diffuse model with sky-backscattered radiation (light reflected from the ground and back again from the sky). The single-layer model of Brine and Iqbal [37] uses essentially the same beam model as Leckner, albeit with updated expressions. Their addition to the field was to separate diffuse radiation into three clear components: a contribution from Rayleigh scattering, from aerosol scattering, and from ground-sky reflections. In this way, the differences in scattered radiation dispersion from the former two processes could be encoded. Further improvements were brought by Justus and Paris in 1985 [38], using a pressure-corrected air mass and an improved water vapour absorption expression in the beam model.

Bird and Riordan [39] of NREL made slight modifications to the model of Justus and Paris, in order to force it to match the output of the earlier BRITE model. A sub-model to translate the simulated solar spectrum on the horizontal to an arbitrarily tilted plane was added to complete their model, which they named SPECTRAL and a later version SPCTRAL2. This is the most widely used spectral irradiance model in PV research,

mostly because of its ease of use and performance in validation at numerous locations against other models and measured spectral irradiance data [40], [41].

In 2001, Gueymard published the derivation of a new model called *SMARTS2* (the culmination of earlier development work at the Florida Solar Energy Ceneter (FSEC)) [42], [43]. This work also begins with the established SPCTRAL2 model and refreshes it with the advances of the intervening years (improved absorption models, atmospheric data). Many of the improved sub-models are parameterised versions of the counterparts in the rigorous MODTRAN code and despite its relative simplicity, SMARTS2 output has been shown to agree remarkably well with that of MODTRAN. In addition to the fundamental improvements of the transmission calculations, SMARTS2 also has a range of useful ancillary functions such as models for acceptance angle and grating smoothing effects of spectroradiometers, to allow comparison of measured and modelled data. SMARTS2 is presently recognised as the state-of-the-art parameterised spectral model and is the resource selected to generate the proposed update of the ASTM spectral irradiance standard used in PV device testing standards [44].

4.2 Application of existing clear-sky models to UK climate

The concept of a Bouguer law based atmospheric radiation model of sufficient performance for PV research applications has been proven over time. Not a great deal differentiates the various models discussed above structurally, but an evolutionary refinement is apparent. For its selection as the successor to BRITE as the source for the ASTM spectral standard, Gueymard's SMARTS model has undergone rigorous performance testing against the most complex radiative transmittance models and a selection of measured spectral irradiance data [44]. It is also made freely available by the author and has been used here as the basis of the spectral irradiance model for all sky types.

This section gives a brief description of Gueymard's SMARTS model in order that the basis of the following discussion may be understood. The full detail of the model is found in the original report [42] and the publication of the beam component model [43]. Note the suffix number has recently been dropped by the author, in favour of a rolling version number. At the time of writing, SMARTS v2.9.2 is current with a new release

due shortly. The input selection and sensitivity is also discussed and an evaluation based on spectra measured at CREST is presented.

4.2.1 SMARTS Model Description

The irradiance striking a collector plane is modelled as three components: beam irradiance arriving directly from the solar disc, diffuse from the sky hemisphere, and a ground-reflected component. These are then combined and translated onto an arbitrarily inclined surface using a tilted surface radiation model by the same author:

$$E_{i\lambda} = E_{bn\lambda}\cos(AoI) + R_{d\lambda}E_{dh\lambda} + \rho_{g\lambda}R_r E_{h\lambda} \tag{4.2}$$

where $E_{i\lambda}$ is the spectral irradiance on the inclined plane, $E_{bn\lambda}$ is the beam spectral irradiance normal to the sun, $E_{dh\lambda}$ is the diffuse spectral irradiance incident on the horizontal and $E_{h\lambda}$ is the global spectral irradiance (the sum of beam and diffuse spectral irradiance incident on the horizontal). AoI is the solar angle of incidence to the collector plane, $\rho_{g\lambda}$ is the spectral ground albedo local to the system and R_r is the view factor between the collector plane and ground. $R_{d\lambda}$ is a similar view factor between the collector plane and sky, but is a function of wavelength and solar position to account for the varying isotropy of different wavelength-dependent scattering processes.

Beam Flux Calculation

The beam component is modelled as the product of the extraterrestrial spectral radiation and six wavelength-dependent transmission coefficients corresponding to processes of Rayleigh and aerosol (Mie) scattering, and absorption by ozone, water vapour, nitrogen dioxide and finally all other gases, which are assumed to be uniformly mixed throughout the atmosphere. The extraterrestrial spectrum has been assembled from data from the latest measurement missions over different wavelength bands and is considered stable, the one correction made being the effect of the change in Earth-Sun distance as the Earth completes its elliptical orbit. This is introduced as a simple broadband scaling factor to the spectral radiation outside the atmosphere at 1 astronomical unit (a.u.):

$$E_{bn\lambda} = DE_{0n\lambda}T_{R\lambda}T_{a\lambda}T_{o\lambda}T_{w\lambda}T_{n\lambda}T_{g\lambda} \tag{4.3}$$

where D is the Earth-Sun distance correction, $E_{0n\lambda}$ is the extraterrestrial spectral irradiance normal to the Sun at 1 a.u. and the T's are the transmission fractions of the atmospheric processes mentioned above. The transmittance for each of the six scattering and absorption processes are dealt with in individual sub-models, all of which are based on Bouguer's (Beer-Lambert) law, equation (4.1).

Rayleigh scattering describes the interaction of radiation with particles smaller than the wavelength, such as is the case for individual air (N_2, O_2) and water molecules. Interaction with larger suspended particles (aerosols) gives rise to Mie scattering and absorptive extinction. The balance between the two scattering processes depends on particle size distribution and wavelength and dictates what proportion of the scattered light reaches Earth and how much is reflected back to space, since they have different phase functions. The extinction coefficients and hence transmittances for both processes vary continuously with wavelength. The Rayleigh extinction coefficient varies as $1/\lambda^4$ and the aerosol extinction as $1/\lambda^{0\text{-}4}$ (depending on particulate size), leading to strong spectral biasing. Figure 4.2 shows how this biasing changes with airmass. The transmittance product of the two processes is shown relative to the AM1.5 case.

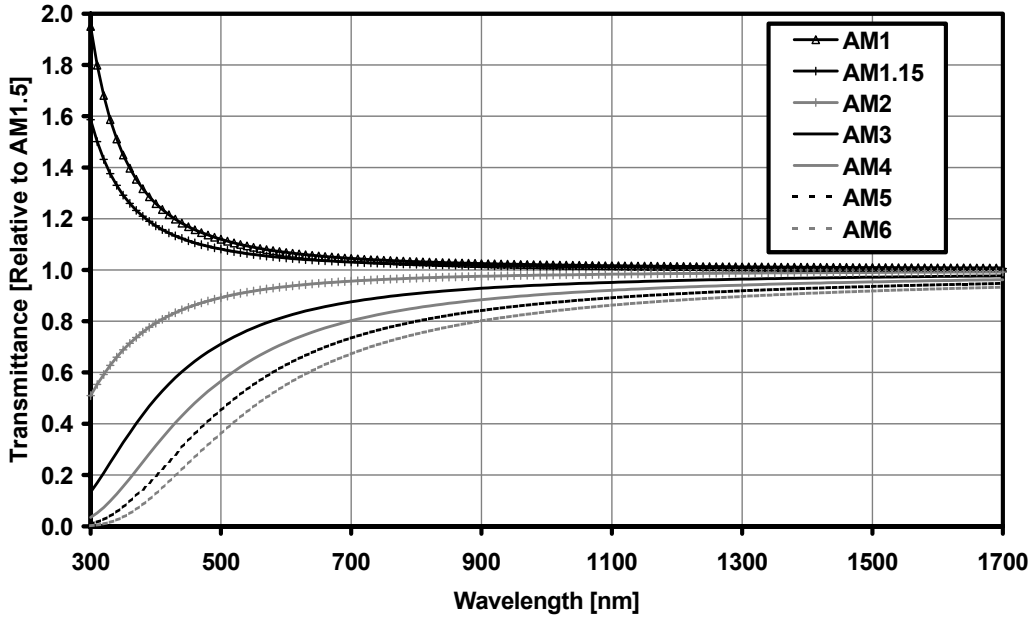

Figure 4.2: Change in Rayleigh-aerosol transmittance relative to AM1.5 conditions

In Loughborough, the minimum airmass experienced is approximately 1.15, in mid summer. In contrast, AM values below 4 are not encountered in December. Given that the maximum in the spectrum lies in the 4-500 nm range, it is clear to see the primary driver of the observed seasonal spectral shift is the effect of airmass on bulk atmosphere scattering.

The extinction due to absorption by various atmospheric gases (chiefly O_3, NO_2, O_2 and CO_2) does not vary smoothly with wavelength since it is caused by discrete energy transitions of these molecules (Figure 4.3). The extinction coefficients in the Bouguer law representations are the product of species abundance, which must be supplied as model input, and tabularised spectral absorption coefficients. These absorption processes do not greatly affect the spectrum over time since the affected bands tend to be narrow and the atmospheric abundances do not change regularly enough or with large enough differences to approach the spectrum-shifting of the scattering processes.

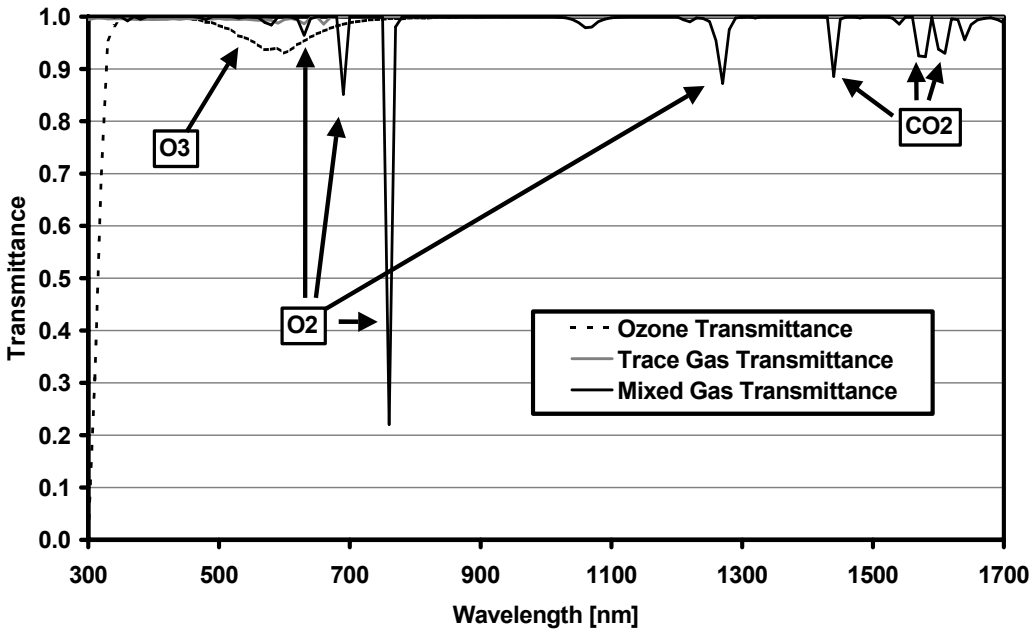

Figure 4.3: Atmospheric radiation transmittance after absorption by various gases

Absorption by water vapour does have a significant impact however. The isotope combinations and multiple rotational and vibrational modes of the molecule lead to many absorption windows in the near infrared and at longer wavelengths. The number and width of these represent a significant amount of absorption in the red end of the spectrum. Unlike the gases discussed above, the water vapour content of the atmosphere

can change on relatively short timescales (hours). Water vapour content is given in cm of precipitable water, the depth of water yielded were the vapour to be condensed at one atmosphere pressure. Increasing humidity deepens and broadens the absorption bands as shown in Figure 4.4. The figure shows transmittances for the largest likely range of precipitable water values, shown relative to 1.42cm, the value used in the generation of the standard spectrum. In Loughborough, summer values of 1-2cm and winter values of 2.5-4cm are the norm.

Precipitable water may be entered directly as an input to SMARTS, or it is calculated internally from inputs of surface air temperature and relative humidity.

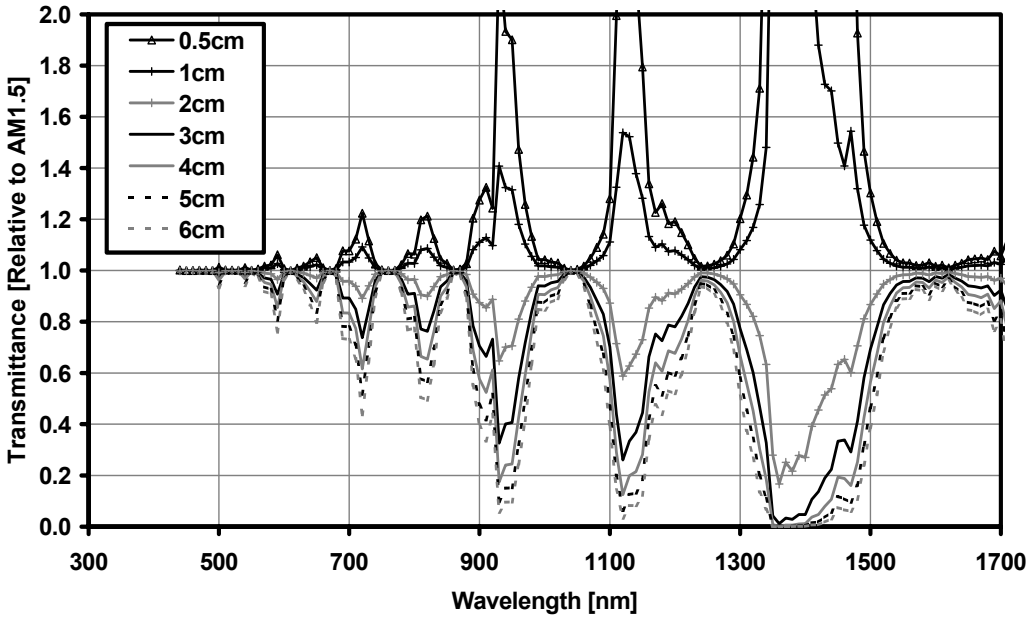

Figure 4.4: Atmospheric radiation transmittance after absorption by water vapour (relative to that of the AM1.5 standard spectrum)

Diffuse Flux Calculation

The diffuse spectral irradiance sub-model is drawn from the scattered fluxes arising from the processes introduced in the beam attenuation sub-model and comprises the sum of three components:

$$E_{dh\lambda} = E_{dR\lambda} + E_{da\lambda} + E_{db\lambda} \tag{4.4}$$

$E_{dR\lambda}$ is the downward flux of radiation scattered by Rayleigh centres, $E_{da\lambda}$ is the downward flux of radiation scattered by aerosols and $E_{db\lambda}$ is a backscattered flux arriving after an arbitrary number of reflections between the ground and sky.

The Rayleigh and aerosol components are modelled similar to:

$$E_{dR\lambda} = F_R DE_{0n\lambda}(1 - T_{R\lambda})T_{aa\lambda}T_{o\lambda}T_{w\lambda}T_{n\lambda}T_{g\lambda}\cos Z \tag{4.5}$$

$$E_{da\lambda} = F_a DE_{0n\lambda}(1 - T_{as\lambda})T_{aa\lambda}T_{o\lambda}T_{w\lambda}T_{n\lambda}T_{g\lambda}\cos Z \tag{4.6}$$

where F_X are the forward (downward) fractions of the scattered fluxes. In the beam model, only the overall transmittance is of interest and aerosols are modelled with a single extinction coefficient. However, aerosols tend not to be perfect scattering centres but also act as absorbers. The distinction becomes relevant in modelling the further propagation of scattered fluxes in the diffuse irradiance model, hence the introduction of separate transmittances for aerosol absorption and scattering processes, T_{aa} and T_{as} respectively. Two key parameters are used to describe aerosol scattering and thus propagate to the diffuse irradiance calculation. The single-scattering albedo is the ratio of the scattering coefficient to the extinction coefficient and determines T_{as}. The asymmetry parameter relates to the relative magnitude of radiation scattered in the forward direction and (with solar position) determines F_a. Both parameters vary with wavelength and humidity, although the relations differ between aerosol models.

The backscattered diffuse irradiance component is modelled as:

$$E_{db\lambda} = \frac{\rho_{s\lambda}(\rho_{b\lambda}E_{bn\lambda}\cos Z + \rho_{d\lambda}Edh\lambda)}{(1 - \rho_{d\lambda}\rho_{s\lambda})} \tag{4.7}$$

where $\rho_{s\lambda}$ is the sky reflectance, $\rho_{b\lambda}$ and $\rho_{d\lambda}$ are the ground reflectance for beam and diffuse radiation, accounting for non-Lambertian surfaces. These ground reflectances refer to the area extending a few km from the system and are not the same as the local reflectance in equation (4.2). Data files of spectral ground albedo for a range of surface types are shipped with SMARTS. The sky reflectance is derived from the atmospheric transmittance calculated in the beam irradiance sub-model.

4.2.2 Input sensitivity analysis

Although ostensibly a simple model, SMARTS still requires a number of input parameters. Many of these such as air pressure, temperature and relative humidity are readily available from meteorological networks. Others, such as gas abundances and aerosol turbidity and behaviour, must be estimated for most applications. To assess the errors introduced by these estimates, an analysis of the sensitivity of the model output to various inputs is presented in this section. The setup for producing the standard AM1.5 global spectrum (as per Table 6 in [44]) is used in all the following cases, with only the parameter under investigation being modified.

Effect of Meteorological Parameters

The single largest influence to alter the terrestrial solar spectrum under clear skies is variation of the atmospheric path length, parameterised with the airmass. As mentioned above, a change in airmass alters the spectral attenuation of the beam irradiance through bulk atmosphere scattering (and indirectly the diffuse component). Figure 4.5 shows the effect of airmass variation (simulating a sun-tracking surface to remove angle of incidence effects). Recalling the average photon energy as a blueness indicator, this parameter varies from 1.64eV at AM 1 to 1.42eV at AM 6 (a solar elevation of ~10°).

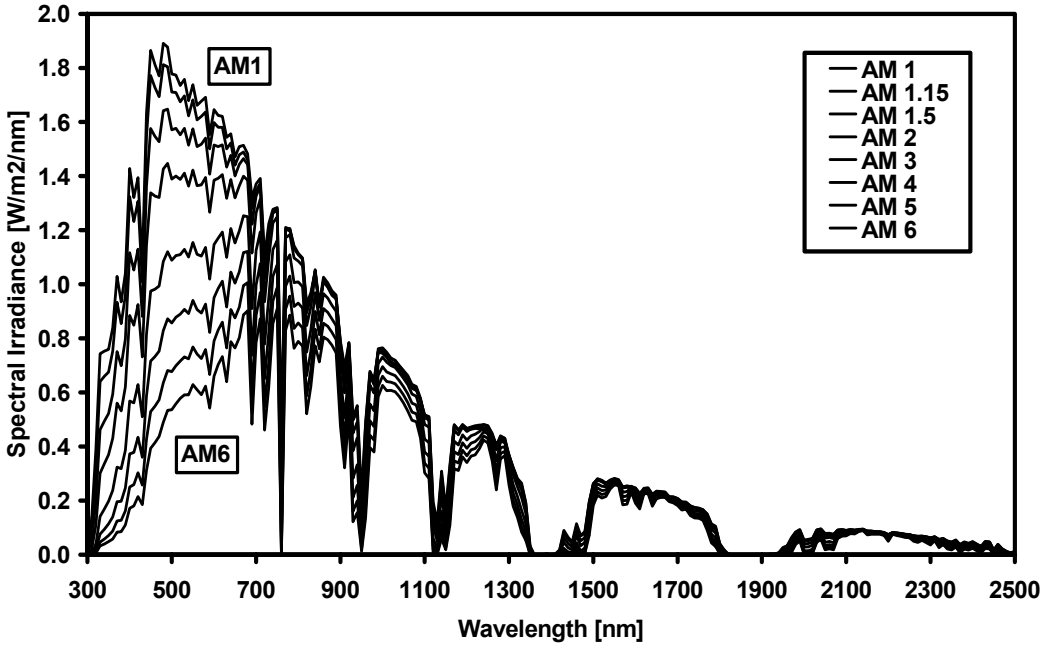

Figure 4.5: Sensitivity of SMARTS output to airmass variation

Since the airmass is determined from the location and time, both of which are generally known with precision, the atmospheric path length is also well known. However, a correction is applied according to the local air pressure, since weather systems introduce cells of air with different densities thus affecting radiation scattering. Figure 4.6 shows the effect of varying surface pressure on the simulated AM1.5G spectrum.

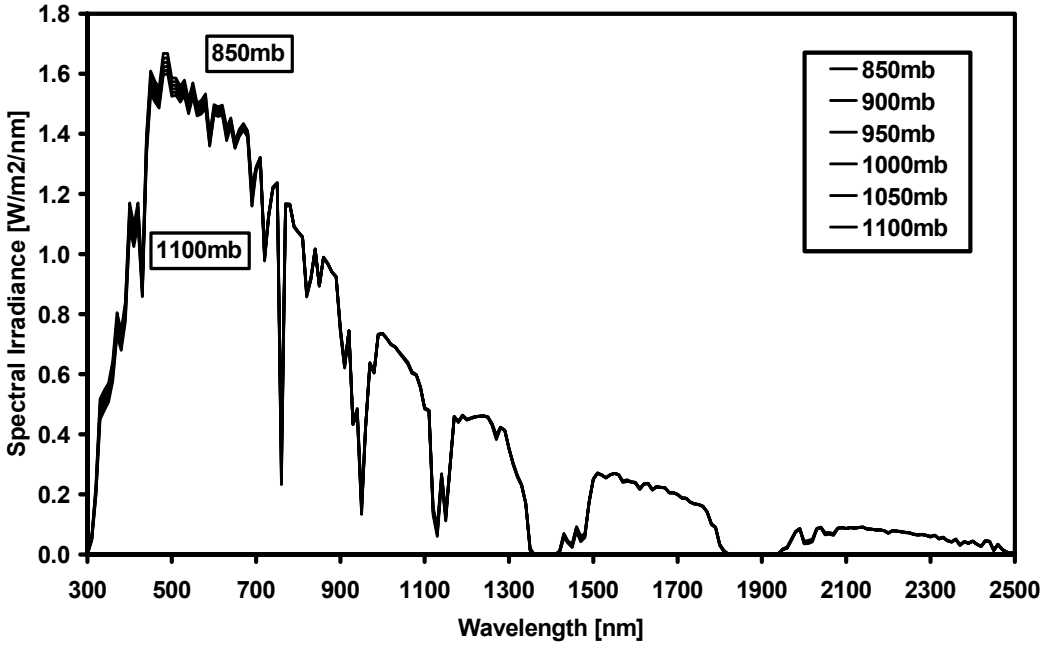

Figure 4.6: Sensitivity of SMARTS output to air pressure variation

Very little effect is observed: this is quantified by the average photon energy (APE), which to two decimal places remains constant over the range of pressure used. This range is itself extreme: the highest and lowest surface pressures measured in Loughborough in the last five years were 1043mb and 960mb. The mean value (1013mb, s.d. 12mb) is in agreement with the long-term global sea-level average of 1013.25 and the distribution may be considered typical. Increasing airmass does not increase the significance of the pressure correction. The key point here is that if measurements of air pressure are not available to use as input to SMARTS, this will not critically affect the simulation results.

In the previous section, the effect of atmospheric water vapour content was introduced. Direct measurements of precipitable water vapour are rarely available to use as input, instead measurements of air temperature and relative humidity are used to calculate it. Figure 4.7 shows the effect of varying air temperature and humidity. APE increases

from 1.59 at 0°C to 1.65 at 40°C (humidity constant at 60%) and from 1.59 at 10% humidity to 1.66 at 100% humidity (temperature constant at 25°C).

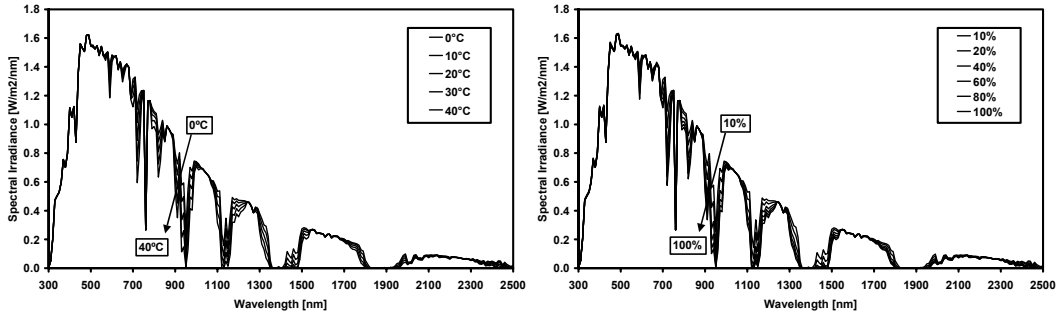

Figure 4.7: Sensitivity of SMARTS output to air temperature and relative humidity variation

Effect of Aerosol Parameters

The most troublesome aspect of modelling the spectral beam irradiance is in assessing the atmospheric aerosol loading. Characterising the aerosol in terms of its single-scattering albedo and asymmetry parameter is also fundamental to the diffuse irradiance calculation. The understanding of aerosol behaviour in the atmosphere is far from complete and active research is found in branches of remote sensing, meteorology and climatology. While it is generally appreciated that the issue is complex, simple models are still used in everyday engineering solutions because the inputs required for more detailed modelling are simply not available widely enough. SMARTS employs a modified version of one of the most common aerosol extinction representations, developed by Ångström in the 1920s:

$$\tau_{a\lambda} = \beta\left(\frac{\lambda}{1\mu m}\right)^{-\alpha} \tag{4.8}$$

where λ is given in μm and β is the aerosol optical depth (AOD) at 1μm. It has been shown that for most aerosol models, using a single set of α and β leads to large departures of the AOD calculated with Ångström's formula from measured AOD at different wavelengths. The modified formula used in SMARTS defines separate α for two spectral regions, either side of 0.5μm. The original β is retained for the longer wavelength region and is modified by a function of α for the lower.

The aerosol loading is thus input to SMARTS as a measure of turbidity, which may be given directly as Ångström's β (AOD at 1μm or $\tau_{1.0}$) or represented by another scale and converted. Turbidity measurements tend to be published as AOD at 0.5μm (closer to the spectral maximum) and this convention is used here (also in the specification of the standard spectrum). The impact of turbidity is shown in Figure 4.8 for the AM1.5G spectrum. The APE varies from 1.62eV in the aerosol-free case down to 1.59 for a $\tau_{0.5}$ of 0.48. This is as bad as is seen practically for very highly polluted urban centres or near forest fire/volcanic events (the June 2002 dip in APE in the NREL data of Figure 2.17 shows the effect of the Colorado 'Hayman' forest fire, one of the largest on record). For reference, the turbidity value to be used in the revised spectral standard is a $\tau_{0.5}$ of 0.084.

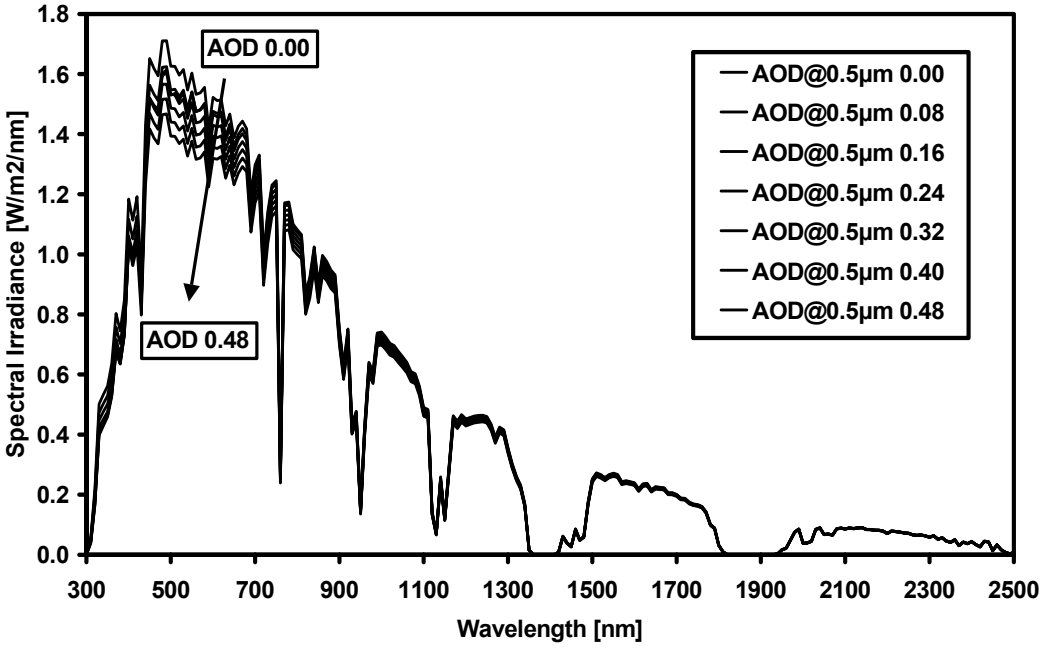

Figure 4.8: Sensitivity of SMARTS output to aerosol turbidity variation

Ångström's 'wavelength exponent' α in equation (4.8) is a simplified parameter, reducing a distribution of particle sizes to an effective particle size. α takes a value from 0, for very large particulates, to a theoretical maximum of 4, where the particle size is in the Rayleigh scattering regime (see earlier discussion). A more practical range, based on observations in the literature is 0.5-2.6. SMARTS offers the choice of 9 aerosol models with defined α values (in practice, these are functions of humidity also and this has been included where possible). The aerosol models also define the single-scattering albedo and asymmetry parameter as functions of wavelength (and humidity). Figure 4.9 shows

the choice of aerosol model has little effect on the standard spectrum (for which Shettle and Fenn's Rural Aerosol model is specified).

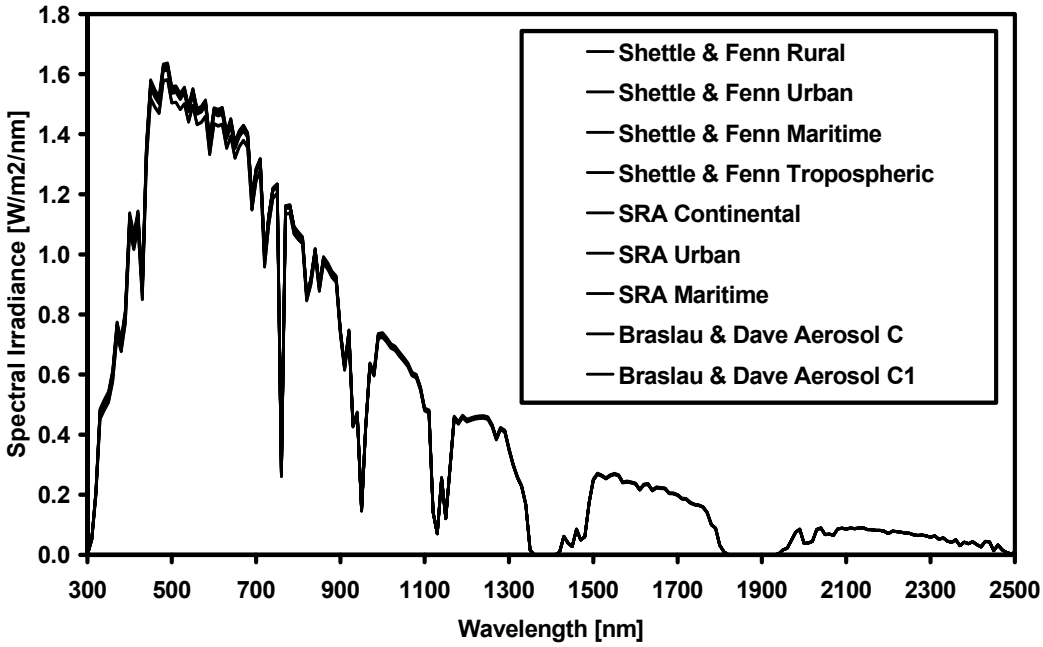

Figure 4.9: Sensitivity of SMARTS output to aerosol sub-model at AM1.5

This is not so surprising: the low airmass condition for the standard delivers a very low diffuse irradiance fraction so the differences between the models as far as the scattering/absorption properties of the aerosol are not apparent. The main factor separating the aerosol models is the particle size distribution. This is not obvious at low airmass, but serves to exaggerate or mitigate the airmass effect seen in Figure 4.5. The difference in spectral blueness variation with airmass for the Shettle and Fenn Rural and Maritime Aerosol models is shown in Figure 4.10

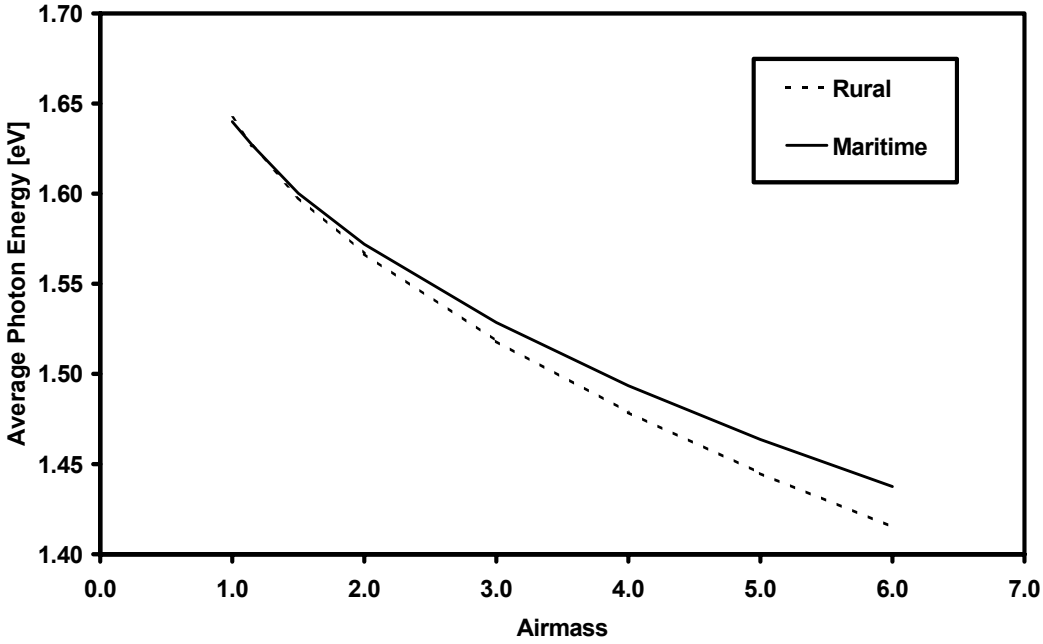

Figure 4.10: Sensitivity of SMARTS output to aerosol sub-model at higher airmass

Combined with airmass effects, aerosol turbidity and scattering properties can have a dramatic impact on spectral variation. However, turbidity is not an easy quantity to measure. There are empirical relations to convert values of visibility or meteorological range to $\tau_{0.5}$, but these source values are estimates using the human eye. This introduces a great deal of subjectivity to the 'measurement', generally means there is not a continuous scale (since existing landmarks will be used in most cases) and data availability is poor as it is not a standard measurement and there is no automated recording by data-logger.

AOD may be inferred from high-resolution spectral beam irradiance measurements, but requires a tracking spectropyrheliometer. Irradiance measurements are made at multiple wavelengths (avoiding water vapour and other strong gas absorption bands) at different airmass values, i.e. over the course of a cloud-free day. The measurements are corrected for air molecule scattering by modelling the Rayleigh transmittances, leaving extinction by aerosols as the sole attenuation process:

$$E_{bn\lambda} = DE_{0n\lambda}T_{a\lambda} = DE_{0n\lambda}e^{(-\tau_{a\lambda}m_a)} \tag{4.9}$$

where m_a is the airmass. A Langley plot of the day's measurements is made for each wavelength by taking the natural logarithm of each side and plotting $\ln(E_{bn\lambda})$ against

airmass. The gradients yield the AOD for each measured wavelength and are used to build a simultaneous set of equation (4.8), solved for α and β. In principle, β could be determined directly from a Langley plot of measurements at 1μm, but this wavelength is on the edge of a water vapour band and is not generally favoured for aerosol AOD extraction.

Aside from the instrumentation requirements, the Langley plot method is also rather prone to error, not least because it requires measurements taken over several hours to extract parameters which may vary on shorter timescales. Although SMARTS does offer the option of explicitly entering α parameters, the single-scattering albedo and asymmetry parameter, it is not possible to determine these at CREST. Therefore, the built-in Rural and Maritime aerosol models were selected for testing against the spectral irradiance measurements at Loughborough, as these seem the most appropriate according to their specified scope. Turbidity has been held fixed at the standards value of 0.084 ($\tau_{0.5}$).

4.2.3 Evaluation at Loughborough against clear-sky spectra

SMARTS was tested by comparison to 12 months of measured spectral irradiance data taken in Loughborough between May 2003 and April 2004. Data was filtered for spectral measurement stability and a broadband irradiance threshold of 20 Wm^{-2} was employed. Clear-sky spectra were selected as those where the integrated total gave an AM-corrected clearness index (equation (2.7)) greater than 0.8. The meteorological inputs are the concurrent data from LUMetS.

Figure 4.11 and Figure 4.12 show the summarised results of the modelling using the 'rural' and 'maritime' aerosols sub-models, respectively. The averaged measured and modelled spectra are shown, as are the mean bias error and r.m.s. error of each wavelength. No normalisation has been performed between the model results and measurement.

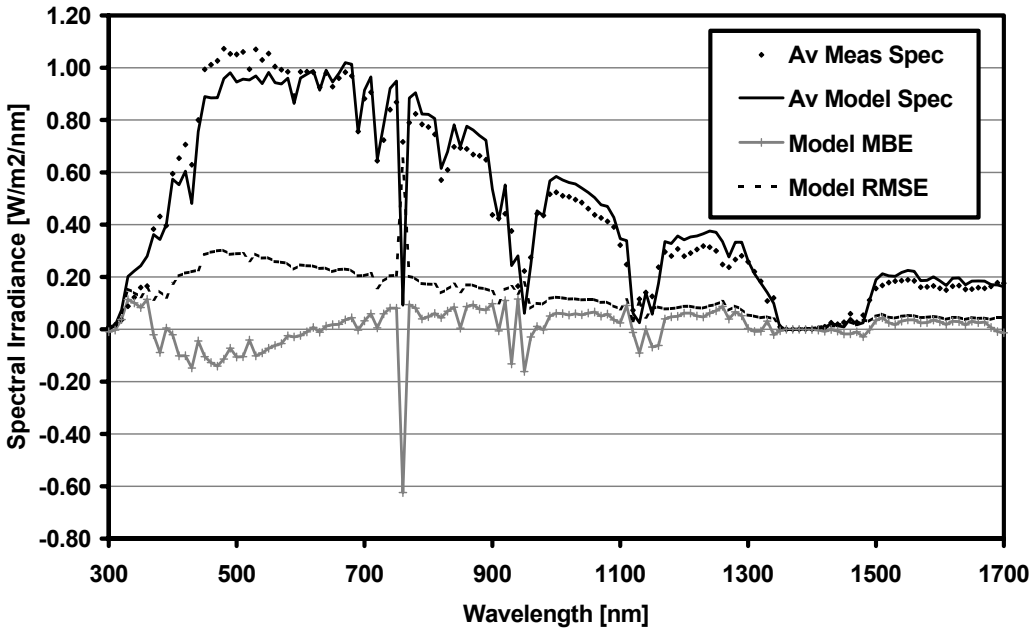

Figure 4.11: SMARTS performance against Loughborough data using the rural aerosol model

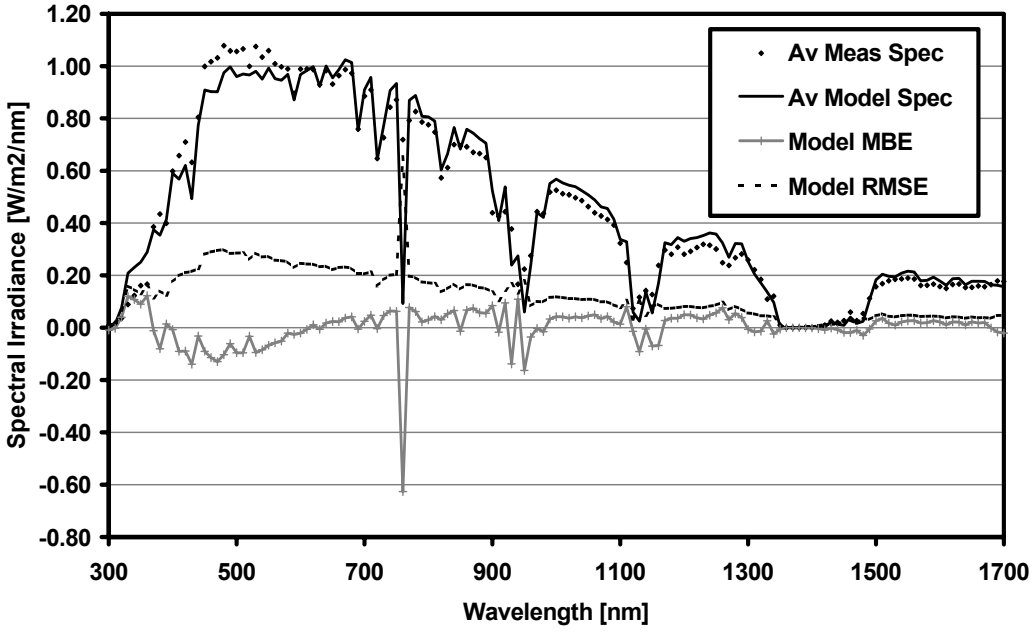

Figure 4.12: SMARTS performance against Loughborough data using the maritime aerosol model

The large spikes in the error curves are caused by the smoothing effect of the spectroradiometer gratings, which pass a finite bandwidth. The narrow absorption bands modelled by SMARTS are thus not represented exactly in the measured data. SMARTS

does have the option of simulating this effect which was not used here as it will not be employed in the modelling to follow and may prove misleading.

A marginal improvement is seen in selecting the maritime aerosol model over the rural. In terms of spectral blueness, the mean bias error of APE is reduced from –0.046 to –0.033eV by this selection and the rms error from 0.074 to 0.059eV. Further reductions in these errors may be possible by development of an aerosol model specific to the local climate or by including aerosol turbidity seasonal/daily profiles. However, as discussed previously the automatic selection of clear skies is an inexact science and it is as likely that the residual error seen in the preceding figure is due to measurements under partly cloudy situations (which skew to the blue) being passed by the clearness definition used.

Due to these reasons, the demands of aerosol characterisation discussed above and to facilitate wider applicability of the spectral model in development, it was decided not to pursue a refinement of the SMARTS sub-models specific to this one site.

4.3 Extension to all-sky irradiance modelling

4.3.1 Existing methods for cloud correction

SMARTS has been shown to work well within the designed, clear-sky use. However, whilst clear, cloudless skies may prevail in a few exceptional locations, this is generally not the case - certainly not in maritime climates such as that of the UK. Here, weather systems are in almost continual motion across the country and days with cloud-free skies are a rarity. Having no designed function to deal with cloud effects, untreated SMARTS results for cloudy days are nonsensical.

Attempts to include cloud effects in radiation modelling for PV are rather few and mostly limited to empirical relations for broadband irradiance. This reflects the long-standing attitude that energy delivered by PV systems under such conditions makes little contribution to the total yield. This is a convenient fallback argument when confronted with the overwhelming complexity of cloud physics modelling. MODTRAN includes some cloud spectral transmission modelling, but the input parameter requirements are too numerous and complex to be met for anything but specialist use. The alternative is to make some semi- or entirely empirical correction to a clear-sky

model and for this purpose simplified models such as SMARTS are sufficient to use as a basis.

Measurements of spectral irradiance are compared to output from the clear-sky model to fit coefficients for a parameterised cloud modifier. In the simplest case the parameter is broadband irradiance, by which the modelled spectrum is normalised. This treats clouds as a neutral density filter and fails to address spectral transmission, as shown later in this discussion. Other cloud correction methods rely in part on normalisation however and using the broadband irradiance is more practical than spectral irradiance at a specified wavelength, since broadband measurements are much more widely available.

Over short ranges of wavelength in the visible there has been some success parameterising cloud correction models with a clearness indicator and power functions of wavelength (e.g. [45]). However, such an approach was found not to be applicable to other parts of the spectrum containing strong absorption bands (especially those of water vapour), where the effects of cloud cover does not bear a continuous relation to wavelength. Thus practicable cloud corrections for the whole spectrum must be discretised into wavelength bins.

To the author's knowledge, only one full spectrum cloud correction has been developed and implemented for PV research. In the late 80s, work started to adapt NREL's SPCTRAL2 clear-sky model to cope with cloudy conditions [46], culminating in the SEDES1 model [47]. Broadband-normalised SPCTRAL2 output and measured spectral data were used to fit a scaling factor (as a second order polynomial function of clearness index) for each wavelength bin:

$$\frac{E_{i\lambda}}{E_{i\lambda clear}} = CCM_{\lambda} = a_{\lambda} + b_{\lambda} k_T + c_{\lambda} {k_T}^2 \tag{4.10}$$

where $E_{i\lambda}$ is the measured spectral irradiance on an inclined plane, $E_{i\lambda clear}$ is the normalised, clear-sky spectrum modelled by SPCTRAL2 and *CCM* refers to the 'Cloud Cover Modifier'. The polynomial form was decided on the basis of plots of the ratio on the left of equation (4.10) against k_T for selected wavelengths.

Although the approach seems reasonable, there are two points for concern: Firstly that the parameter used as a measure of cloud attenuation has an airmass dependence as discussed in Chapter 2 and repeated here:

$$k_T = \frac{G_H}{G_0 / AM} \tag{4.11}$$

where G_H is the measured broadband global irradiance, G_0 is the solar constant and AM is the airmass. Ignoring the airmass influence in the cloud modifier can lead to confusion, or rather duplication, where quite different sky conditions can share the same value of clearness index. For instance, a clear sky with the sun at low elevation could give the same k_T as a cloudy sky with the sun at higher elevation.

Analysis of spectral irradiance measurements from Loughborough shows the polynomial relationship on cloud attenuation reported by Nann and Riordan, but also a dependence on airmass. The second point concerns the set of measured spectral data used to determine the cloud modifier function coefficients. The set was limited to just over four months of Summer-Autumn data, thus does not contain information of seasonal variation of cloud types/quantity, or a representative distribution of airmass. Long-term spectral irradiance measurements exhibit seasonal patterns still not fully explained and it is the author's opinion that any empirical approach to spectral modelling should draw on data from at least one complete year. Finally, the quantity of data collected was such that all of it was required in fitting the CCM coefficients, leaving none for independent assessment of the overall model performance.

4.3.2 Improved technique

Because of these observations, it was decided to attempt to improve on this area, firstly through the use of the best of the available clear-sky spectral models (SMARTS). This should reduce the compensation performed by the CCM for deficiencies in the clear-sky modelling (e.g. aerosols, as cited by Nann and Riordan).

The parameterisation of the CCM is extended to include airmass dependence by binning data by this second variable and increasing the number of fit coefficients accordingly.

The clearness index k_T is replaced as the measure for cloud cover. For this purpose the AM-corrected clearness k_T* might seem a suitable candidate, but as discussed in Chapter 2, its designed use is as a tool to roughly separate conditions of different cloud cover. It is thus not a precise quantification as it is derived from an empirical broadband atmospheric turbidity. Extrapolating the concept in the light of the performance of SMARTS against the clear-sky Loughborough data, a clear weather index (CWI) parameter has been defined as the ratio of measured terrestrial irradiance on a horizontal surface to simulated clear-sky terrestrial irradiance (broadband SMARTS output) on a horizontal surface. In this way, the air mass can be used to parameterise spectral variation due to atmospheric path length and the CWI can be used to parameterise spectral variation due to atmospheric opacity.

Separate cloud adjuster functions are developed for the beam and diffuse spectra, based on air mass and clear weather index. These are implemented as reductors for each irradiance component, based on a Liu-Jordan assumption of isotropy of diffuse irradiance [48] and neglecting ground reflected contributions, giving the irradiance at wavelength λ incident on an arbitrary plane as:

$$E_{i\lambda} = E_{bn\lambda}\cos(AoI) + R_d E_{dh\lambda} \tag{4.12}$$

where $E_{bn\lambda}$ is the spectral beam irradiance normal to the Sun, AoI is the solar the angle of incidence to the plane, $E_{dh\lambda}$ is the spectral diffuse irradiance on the horizontal and R_d is the fraction of the sky to which the plane has a view.

The cloud adjuster for the in-plane spectral irradiance is defined at each wavelength as:

$$Adj\left|E_{i\lambda} = E_{i\lambda clear} - E_{i\lambda meas}\right. \tag{4.13}$$

where $E_{i\lambda clear}$ is the clear-sky modelled irradiance and $E_{i\lambda meas}$ is the measured spectrum. Combining (4.12) and (4.13) yields for the individual component adjusters:

$$Adj\left|E_{i\lambda} = Adj\right|E_{bn\lambda}\cos(AoI) + R_d\, Adj\left|E_{dh\lambda}\right. \tag{4.14}$$

12 months of spectral irradiance measurements (September 2003 to August 2004) were used to fit the empirical adjusters for the cloud module. This is currently the longest continuous period of measured spectra with concurrent thermopile measurements. The significance of this was discussed in chapter 2 – that the integrity of the spectral irradiance measurements is best ensured with the stability filter, relying on 10-second thermopile measurements. Since the best quality measurements are desired for both fitting and performance testing the spectral data were divided into two groups, each comprising alternate weeks of measurements. In this manner, data independent from the fitting set can be used for validation, while both sets contain spectra from all seasons and weather types.

For each measured spectrum, the clear weather index (CWI) is calculated from the ratio of measured global irradiance in the horizontal (from the corresponding pyranometer measurement) to modelled global irradiance (integrated SMARTS output). The airmass (AM) is calculated from the date, time and site location and the measured spectra are binned in these two parameters.

For each AM-CWI bin, data are compared on the basis of the solar angle of incidence (AoI) to the plane of spectral measurement (latitude tilt of 53˚). In this way, pairs of data are identified where the AM and CWI conditions are similar and the AoI are significantly different. It is assumed that each combination of AM and CWI gives rise to a unique perturbation of the clear sky spectrum, hence the same adjustment for cloud should be valid in each bin. By then considering two different angles of incidence on the inclined spectral measurement system, beam and diffuse components can be inferred and separate adjustments to the beam and diffuse spectra can be determined from (4.14):

$$\begin{aligned} Adj\left|E_{i\lambda 1}\right. &= Adj\left|E_{bn\lambda 1}\right. \cos\left(AoI_1\right) + R_d\, Adj\left|E_{dh\lambda 1}\right. \\ Adj\left|E_{i\lambda 2}\right. &= Adj\left|E_{bn\lambda 2}\right. \cos\left(AoI_2\right) + R_d\, Adj\left|E_{dh\lambda 2}\right. \end{aligned} \tag{4.15}$$

where the subscripts 1 and 2 specify the two measurements of the couplet. The following assumptions are made on the basis that the two measured spectra are from the same bin with the same conditions:

$$\begin{aligned} Adj\left|E_{bn\lambda 1}\right. &= Adj\left|E_{bn\lambda 2}\right. \\ Adj\left|E_{dh\lambda 1}\right. &= Adj\left|E_{dh\lambda 2}\right. \end{aligned} \tag{4.16}$$

Eliminating and rearranging (4.15) yields the adjuster for the beam component:

$$Adj|E_{bn\lambda 1} = \frac{Adj|E_{i\lambda 1} - Adj|E_{i\lambda 2}}{\cos(AoI_1) - \cos(AoI_2)} \tag{4.17}$$

Substituting back into either of the pair in (4.15) yields the adjuster for the diffuse component through:

$$Adj|E_{dh\lambda} = \frac{Adj|E_{i\lambda} - Adj|E_{bn\lambda}\cos(AoI)}{R_d} \tag{4.18}$$

The above procedure is performed for each bin and repeated as each data point is paired with every other in the bin to give several calculations of the adjusters, with each corresponding CWI taken to be the average of the pair. The results from all CWI bins are lumped for each AM bracket and $Adj|E_{bn\lambda}$ and $Adj|E_{dh\lambda}$ are fitted against CWI through a standard minimisation process (Levenberg-Marquardt, as implemented in Numerical Recipes in Pascal Code Library [49]). These parameterised functions are implemented with the clear-sky model to form the all-sky model package. The complete input data set required for the model comprises air temperature, pressure and relative humidity, which do not vary drastically over short distances allowing nearby meteorological stations to be used for data, and broadband global irradiance, which is required from the site of interest.

4.3.3 Validation

The second group of 26 weeks of spectral data from the same 12-month period was used to assess the performance of the spectral model. Input data were drawn from the concurrent set of meteorological measurements to simulate spectra, which were then compared to their measured counterparts on the basis of standard deviation and mean bias error for each wavelength of the spectroradiometer. The results for this annual assessment are presented in Figure 4.13, alongside the wavelength-resolved averaged values of all measured and modelled spectral irradiance values.

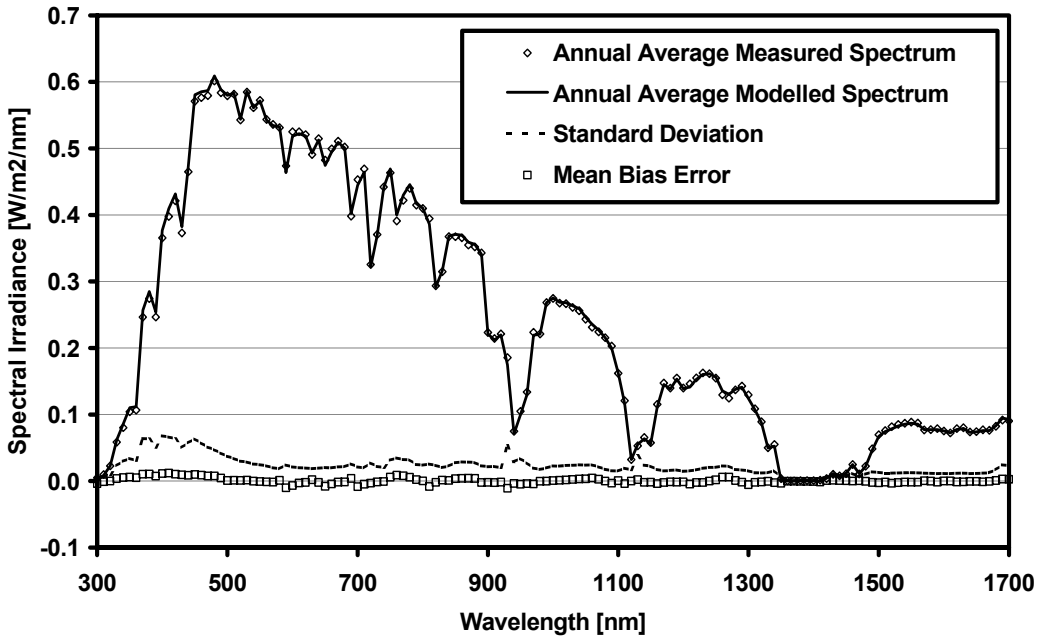

Figure 4.13: Overall results of 12-month ASPIRE performance testing

The basic form of the fitted functions appears sufficient to represent the spectral deviations from the clear-sky model on this annual timescale. Because of the use of measured data in the derivation of the model, the accuracy is ultimately limited by that of the spectroradiometer. As a result, the standard deviation can be seen to increase at shorter wavelengths, but is under 5% for the large majority of the spectrum. The maximum bias error is also in the short wavelength region, but overall displays good spectral stability.

The performance of the spectral model at shorter timescales was then investigated. The same analysis as above was carried out for the months of September 2003, December 2003, March 2004 and June 2004, representing the four seasons and shown top-left to bottom-right in Figure 4.14.

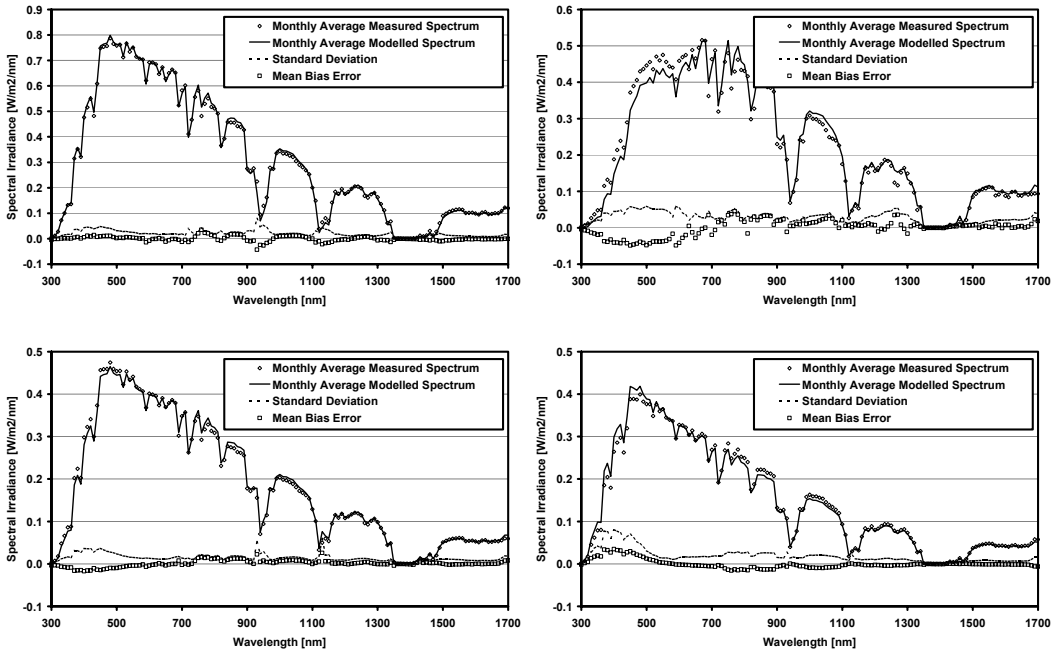

Figure 4.14: Seasonal ASPIRE results (top-left to bottom right: Sep 03, Dec 03, Mar 04, Jun 04)

The errors increase on this shorter timescale, but for most months this is marginal. The exception is December, for which quite a significant bias error is seen (-5% in the blue, +5% in the red). The cause of this is thought to be the maximum cut-off of AM6 for fitting the cloud correction function. The same cut-off is not used to filter out spectra during the performance assessment – instead, these conditions are dealt with using the coefficients of the highest (AM5-6) bin. AM6 corresponds to a solar elevation of only 10˚ and in most months the sun is in this region a very tiny fraction of the time. This is not the case in midwinter however and it seems the model under the current arrangement does not perform so well at these times. The solution would be to extend the fitting range into higher airmass, yet this requires higher-precision measurement of low irradiance conditions than is currently possible with the CREST outdoor system.

The impact this has on calculation of the average photon energy is shown in Figure 4.15 for the monthly timescale. Results from clear-sky modelling are shown for comparison.

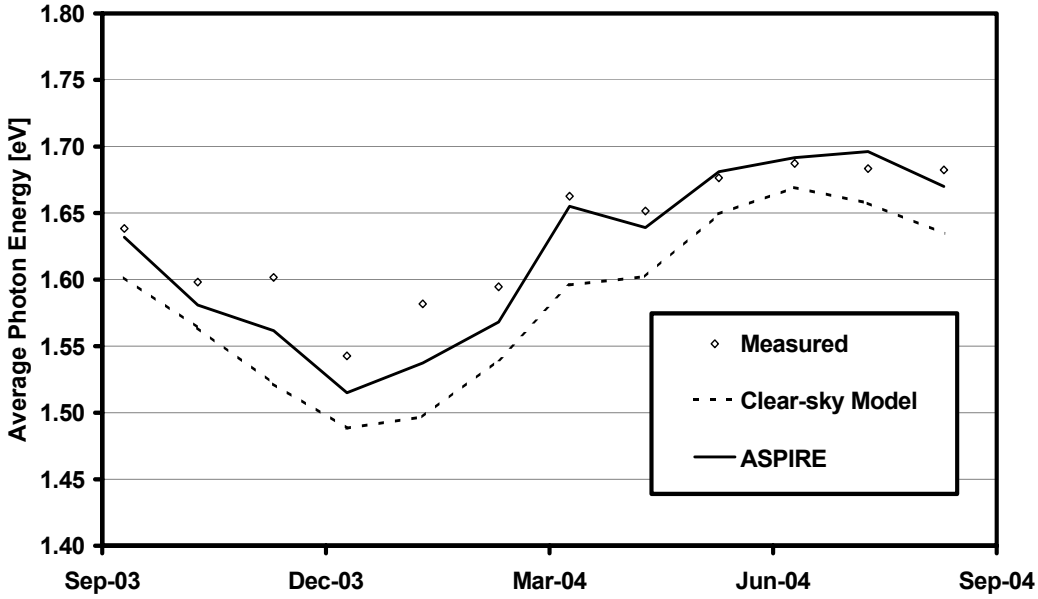

Figure 4.15: Monthly modelling of APE with ASPIRE

Spectral blueness is underpredicted for the winter months, anticipated given the bias errors of Figure 4.14, yet still halves the APE difference between measurement and model compared to using only the clear-sky model. From March to September, model and measurement agree to ±0.01 eV.

4.4 Conclusions

Under ideal conditions (dry, unpolluted atmosphere), the terrestrial solar irradiance spectrum can be modelled so accurately that this is the method used by the World Radiation Centre for calibrating primary spectral standards against solar spectrum measurements. It is thus reasonable to conclude that such an approach would improve understanding of the solar resource even under non-ideal conditions.

The key difficulties in everyday spectral irradiance modelling for engineering purposes originate in the temporal and spatial variability of different aspects of the atmosphere. Many of these, such as changing amounts of ozone, CO_2 and trace gases and variation of air pressure are of little consequence to photovoltaic applications, because of very slow variation or minimal sensitivity of PV technologies. The critical factors affecting solar spectral irradiance under cloud-free skies are airmass, water vapour and aerosol turbidity. The effects of the first two can be modelled well through solar geometry calculations and the use of measurements of air temperature and relative humidity. Measurements of aerosol turbidity are indirect and require equipment that is non-standard as far as national meteorological networks are concerned and thus poses the greatest challenge to improving the performance of clear-sky models.

In performance testing of the current state-of-the-art spectral irradiance model, SMARTS, at Loughborough, no measurements of aerosol turbidity were available. Instead, this parameter was held fixed to the value used in the upcoming revised spectral standard for photovoltaic applications. It cannot be said with any certainty what effect this simplification had on the assessment, since the difficulties in automatic clear-sky detection from a large dataset introduce an error to the process that has hitherto been impossible to quantify. Given these uncertainties, the maximum extent of the standard deviation can be said to be 20% in the visible and 10% in the near infrared. Published assessments at other locations with more predictable sunny weather have shown errors approximately half these values.

The ASPIRE model, an empirical add-on to account for cloud effects, has proved itself in Loughborough. The accuracy of the final model is limited by that of the instrument used to measure the fitting data, but the additional error does not exceed more than 5% on a monthly basis. The model has successfully simulated the rise in APE with

decreasing clearness observed in the spectral measurements presented in Chapter 2 (1.75-1.64 eV for an AM1.5 spectrum with clearness 0.2-1.0). This compares with variation of 1.59-1.64 eV due to changes in aerosol turbidity.

Monthly modelled APE values agree with measurement to within 0.01 eV for most of the year. The probable cause of the increased wintertime error has been identified and that rectification will require higher precision irradiance measurements under low light conditions. This should be possible in the future as the CREST outdoor system is upgraded further.

Further testing at other locations is required to complete the assessment of the model. This is currently hampered by the lack of spectral irradiance measurements in similarly cloudy climates (the very reason for developing the model in the first instance). However, a sizeable advantage has been demonstrated over the use of clear-sky modelling only, so it is believed improvements are to be had through adoption of this approach.

5 Modelling Spectral Effects on Photovoltaic Devices

The work of the previous chapters is now combined to model the effects of spectral irradiance variation on PV devices. Two approaches have been followed to model the I_{SC}: one based on the product of irradiance spectra (in the first instance measurements from the CREST outdoor system) and device spectral response (SR) curves, and one empirical model based on fitting measurement data to simple parameterised functions of the spectral effect. The empirical approach is extended to include a simplified estimate of the average photon energy to sever the reliance on spectral irradiance measurements. Non-spectral effects on other device electrical parameters are incorporated to provide a power model for energy yield estimation.

A discussion of the development of these approaches and their modification for use with multi-junction devices precedes validation against measured data. The strengths and shortcomings of each method are investigated and further developmental work is suggested in the conclusions.

5.1 Spectral Response-based Approach

From the analysis of chapter 3, it has been determined that spectral irradiance variation influences mainly the photocurrent of a PV device directly. It was also shown that for the four modules tested here (and for any module not suffering great detrimental effects due to parasitic resistances) the photocurrent is well approximated by the short-circuit current and that the current at the maximum power point is linear with I_{SC}. The implication is that modelling of the photocurrent with due note of the spectrum is the only additional requirement for improving present power calculation models and hence energy yield estimation.

Given the incident spectral irradiance and the spectral response of a device, the photocurrent can be modelled with an integration of their product, as introduced in the review section of chapter 3:

$$I_{PH} = N_{parallel} \times A_{cell,\,active} \times \int E_i(\lambda) SR(\lambda) \cdot d\lambda \tag{5.1}$$

where $N_{parallel}$ is the number of parallel strings in the module, the area used is that of a single cell and the integration extends over all non-zero values of the spectral response. The application of this approach to single-junction devices and the modifications required to model multi-junction cells are discussed in the following.

5.1.1 Single-junction Cells

This straightforward multiplication poses two major obstacles to implementation. The first is requirement of the irradiance spectrum, for which it is suggested the modelling approaches of chapter 4 are employed for widespread use. The second is the requirement of the device spectral response as an input, which is presently hard to acquire for the module level. Some manufacturers are able to supply such data, but there is little standardisation concerning the conditions and methods by which spectral response curves are measured.

It should also be noted that equation (5.1) contains no explicit temperature dependence for the photocurrent, yet it is known there exists such a relation of the order 0.1%/ºC. This is attributed to reduction of the band gap at elevated temperatures and represents a

change in the spectral response. The temperature dependence of the SR has not received a comprehensive investigation to date, but is in any case likely to be highly device-specific. It has been postulated that irradiance and the state of device degradation also vary the spectral response, through influence of the lifetime-mobility product of the material. How this changes with environmental conditions is not currently understood at all well. The best that can be done presently is to work with the assumption of a fixed spectral response, however this may be obtained, and consider the neglect of temperature dependence and other effects on the current as additional error in the simulation method.

No measured spectral response curves are available for either the c-Si or a-Si single-junction modules investigated earlier in this thesis. Instead, the SR-based model was tested against another single-junction a-Si device, for which the spectral response has been supplied. This device was not used in the analysis chapter because measurement data availability is not so good as for the other. An attempt is also made to model the c-Si device, using the SR curve measured for a different device (that shown in Figure 3.8 without the blue-enhancement). The magnitude of this SR curve has been uniformly scaled to reproduce the measured STC current when combined with the AM1.5G spectrum in equation (5.1).

Measured spectra from September 2003 to August 2004 were extracted from the CREST database and passed through the quality checks described in chapter 2. Where available, concurrent measurements of I_{SC} were also extracted. The short-circuit current of each module was calculated for each measurement timestamp from the measured spectrum and the spectral response using equation (5.1). Correlation plots of the measured and modelled I_{SC} are shown in Figure 5.1.

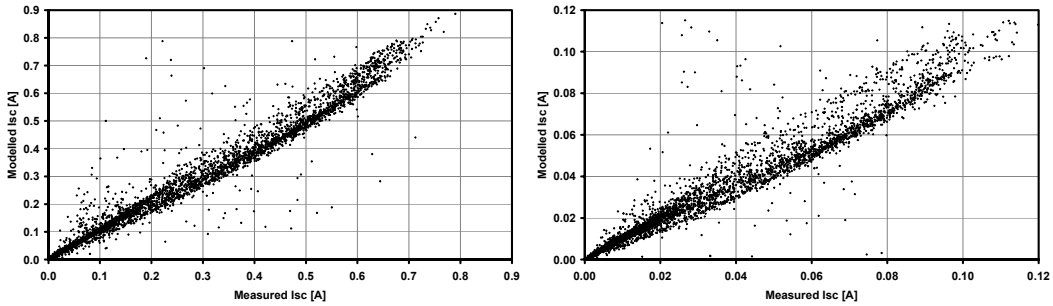

Figure 5.1: Correlation of modelled and measured I_{SC} for c-Si (left) and a-Si (right) modules

The main cluster on the c-Si correlation plot shows a reasonable agreement between measurement and model. Most of the divergence manifests as an over-prediction of modelled I_{SC}, which worsens at higher currents. This would seem reasonable, considering the correlation of short-circuit current with irradiance and temperature and the negative effect these two parameters have been shown to have on the I_{SC} for this particular module, as discussed in chapter 3. These effects are not considered in the fixed spectral response model, hence the observed deviation.

The current modelled for the a-Si module is more scattered, displaying under-predicted and over-predicted clusters. The former is congruent with the findings for the other a-Si module studied in chapter 3, which displays a positive temperature coefficient for I_{SC} (as do the two multi-junction a-Si devices). The over-prediction could be due to parasitic losses influenced by the irradiance.

However, there is a great deal of uncertainty concerning the SR curves used. Figure 5.2 shows the distribution of model error on a monthly basis, normalised to the measured monthly I_{SC} averages.

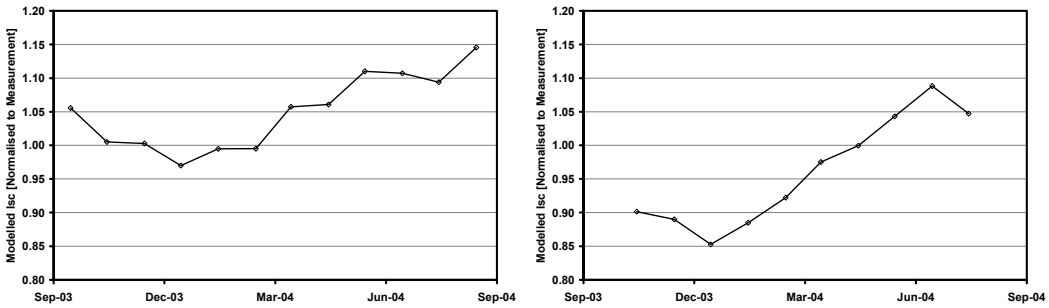

Figure 5.2: Error in SR-modelled monthly averages of I_{SC} for c-Si (left) and a-Si (right) modules

Although the above argument seems to be justified in the case of the c-Si module, for which the error is indeed largest during times of high temperature and irradiance, the case is less clear for the a-Si module. Although the causes speculated above may describe the behaviour of this module also, such statements cannot be made with great confidence. More information regarding environment-driven variation in the spectral response is required to quantify the effects of temperature and also the state of the

device (for instance, the a-Si module modelled here has been on the roof a long time since the SR was measured and there may be issues of degradation to account for).

5.1.2 Extension to Multi-junction Cells

SR curves are available for the two multi-junction devices analysed in chapter 3. These devices are both younger than the single-junction a-Si discussed above and are also less prone to degradation. Hence an investigation was conducted to model these devices using the same SR-based modelling approach.

Calculating the current output of a multi-junction cell is more complicated than for a single cell due to the added constraints imposed by its structure. The system of series-connected sub-cells is analogous to a series-connected string of cells in a module. From Kirchhoff's current law, the same current passes through all components thus connected. This overall string current is limited by the current passage of the weakest component.

The ability of an individual PV cell to pass current is reliant on its performance as a current generator. Mismatch losses arise whenever well and poorly performing cells are connected together in series. In modules, this might arise out of cell failure, or partial shading of the module. The principal difference between cells in a module and sub-cells in a multi-junction device is that while all cells in a module would generally expect to be exposed to the same irradiance, this is not true of sub-cells stacked on top of each other. The top cell of such a device casts a spectral shadow on the cell(s) beneath, dependent on its absorption and the incident spectrum. The photocurrents of each sub-cell thus work in an almost permanent state of mismatch, save for the particular spectrum under which the currents coincide.

For active current sources such as PV cells, the current through a mismatched string is a little higher than the isolated output of the worst generator. However, the difference is small and making the approximation that the string current is equal to that of the worst cell simplifies calculations enormously.

This allows equation (5.1) to be applied for each sub-cell of a multi-junction device, with the device output given by the smallest of these currents (as in [50]). The

additional complications over the calculations of the previous section are the requirement of the spectral response curves of each sub-cell and having to calculate the spectral irradiance transmitted through upper sub-cells to those below. This transmission is calculated following the approach by Schade [51], to assume the quantum efficiency of the top cell is equal to the absorption:

$$T_\lambda = 1 - QE_{TOP,\lambda} = \frac{\Phi_{T\lambda}}{\Phi_{i\lambda}} \tag{5.2}$$

where Φ_i, Φ_T are the incident and transmitted spectra as photon flux densities. In terms of the spectral response of the top cell, the spectral irradiance transmitted to the underlying cell is:

$$E_{T\lambda} = E_{i\lambda}\left(1 - \left(\frac{hc}{q\lambda} \times SR_\lambda\right)\right) \tag{5.3}$$

where E_i, E_T are the incident and transmitted irradiance spectra in $Wm^{-2}nm^{-1}$, the spectral response SR is given in AW^{-1}, wavelength λ is in m and h, c and q are Planck's constant, the speed of light in a vacuum and the electronic charge, respectively.

For transmittance to subsequent sub-cells, exactly the same approach is taken, substituting for the incident spectrum and spectral response where appropriate. The result for the standard spectrum and the a-Si 3j module is shown in Figure 5.3.

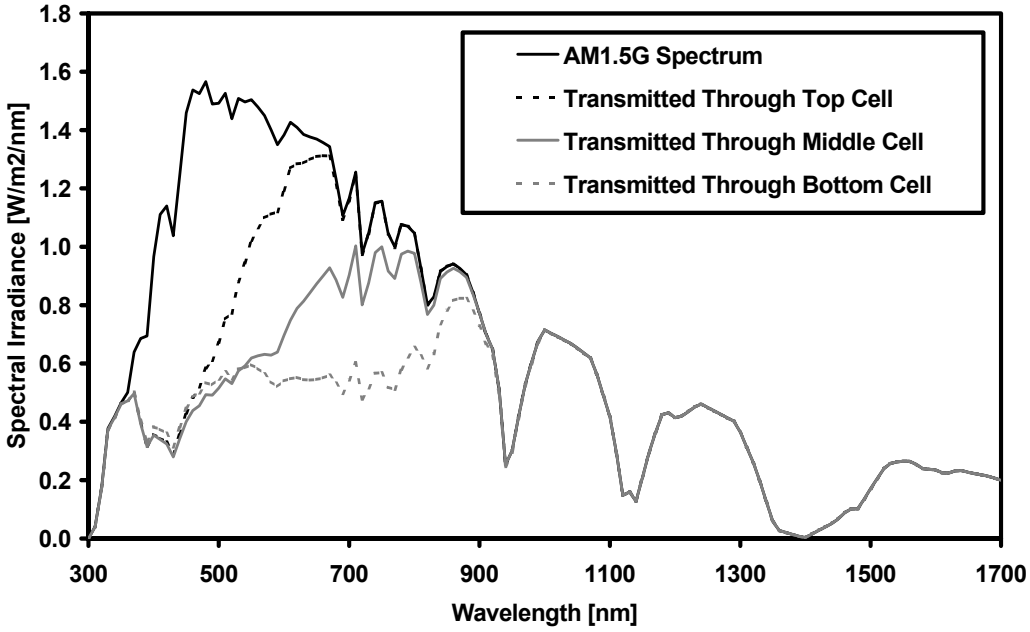

Figure 5.3: Spectral irradiance transmission through the a-Si triple-junction device

The same validation approach was taken as for the single-junction devices in the previous section, with the sub-cell photocurrents of the a-Si 2j and a-Si 3j modules calculated with equations (5.1) and (5.3). The minimum sub-cell current for each device was taken to be the device short-circuit current and these are compared to the values from the measurement system in Figure 5.4.

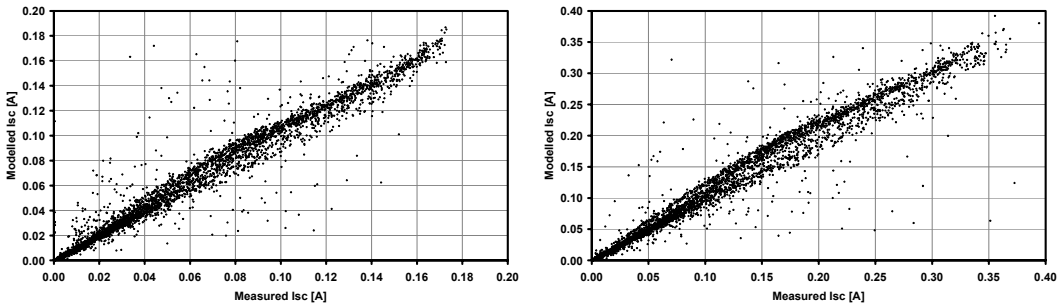

Figure 5.4: Correlation of modelled and measured I_{SC} for a-Si 2j (left) and a-Si 3j (right) modules

The modelling results for the multi-junction devices do not exhibit any greater scatter than for the single junctions and do not demonstrate a clear irradiance/temperature-dependent bias error. The manufacturer-supplied temperature coefficients of I_{SC} are marginally lower for the multi-junction devices than the single-junction a-Si. Hence it is possible the temperature effect is limited in these devices by the exchange of current-

limiting sub-cells. Again, this is conjecture without knowing how the SR curves change under different conditions. The error on a monthly basis is shown in Figure 5.5.

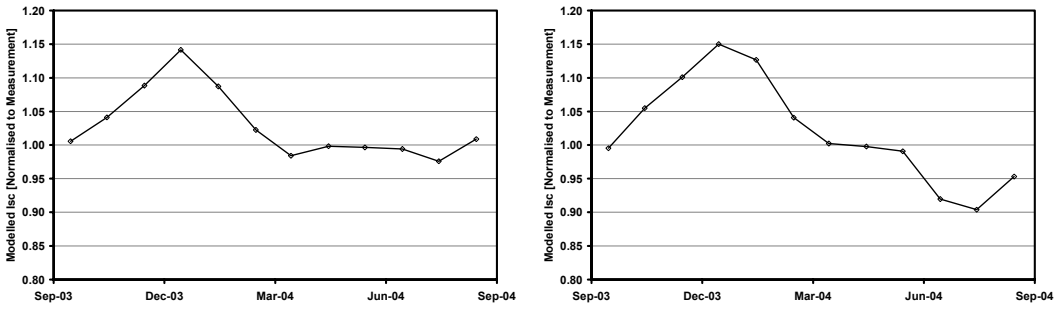

Figure 5.5: Error in SR-modelled monthly averages of I_{SC} for a-Si 2j(left) and a-Si 3j (right)

From Figure 5.5 it appears the error in the SR-based model for the multi-junctions is far more dependent on the spectrum than irradiance or temperature, as for both modules it echoes the seasonal change in APE seen in chapter 2. Note, the disparity of the last three months for the triple-junction device was observed also in the measurement data (chapter 3) and is not considered an error in the modelling here.

For the winter months of most extreme error, the current is limited by the top sub-cell. This is the cell with the narrowest spectral response, which may make it proportionally more susceptical to temperature change. Then the cooler winter operating temperatures would further narrow the response at a time of very little irradiance resource in the blue and reduce the current drastically in this situations, an effect not modelled in the simple approach here.

The limiting factor with a modelling approach based on spectral response is the SR itself. Ultimately, such a method may prove the best way to model I_{SC}, but a greater understanding of how the SR changes will have to be developed to achieve this goal.

5.2 Empirical Parameterisation Approach

Empirical methods of modelling the performance of PV devices offer an alternative that does not require extensive knowledge of device behaviour. They have the potential to predict quite accurately what the power output of a module fully characterised at one location will be for a new site. This requires parameterisation by any such variables that

affect PV efficiency as will be available for potential installation sites, over as wide a range as possible. Thus far, such approaches have been limited to irradiance and temperature effects by the availability of input variables and in the characterisation procedures themselves. This section will examine the current methods, before investigating any benefit that inclusion of spectral effects might bring.

5.2.1 Temperature Effect Model

The I_{SC}, and hence V_{OC}, dependence on irradiance-related variation of the parasitic resistances as discussed in chapter 3 is almost universally ignored in PV device modelling. There is presently no general model of how these resistances change, a behaviour which varies greatly between different PV technologies. Yet it is accepted (and was reinforced in the course of this work) that such effects influence devices mostly under low irradiance conditions and hence this is a convenient reason for disregarding them when the goal is prediction of energy yield on monthly or annual timescales.

Module temperature is thus the only cause commonly modelled as disturbing the linearity of I_{SC} on irradiance and is also well known to influence the voltage of a device. The temperature dependences of the electrical parameters of most PV devices are generally given as, or approximated by, linear relationships referencing back to the values under Standard Test Conditions:

$$I_{SC} = G \times \left[\frac{I_{SC}|_{STC}}{G|_{STC}} + \alpha_{ISC} \left(T_{MOD} - T_{MOD}|_{STC} \right) \right]$$
$$V_{OC} = V_{OC}|_{STC} + \alpha_{VOC} \left(T_{MOD} - T_{MOD}|_{STC} \right) \tag{5.4}$$

Similar relations are also given for power at maximum power point (P_{MPP}), or both the current and voltage at this point (I_{MPP}, V_{MPP}).

Potential PV installation sites will generally have some useable form of irradiance measurements, either from instrumentation setup by the developer or from a national meteorological network. The UK Meteorological Office for instance measures global (horizontal, hemispherical) irradiance as standard at each of its stations. Such

measurements may be translated to the inclined plane to give a good estimate of the solar resource [52]. Module temperature is more challenging in that it must be determined indirectly from measurements of ambient air temperature and irradiance. This is done typically by adjusting the Nominal Operating Cell Temperature (NOCT) of the module, given by the manufacturer or measured as the equilibrium temperature under particular environmental conditions[†]:

$$T_{MOD} = T_{AMB} + G \times \frac{NOCT - 20}{800} \tag{5.5}$$

where T_{AMB} is the ambient air temperature and G is the irradiance. This simple approach has a rather limited accuracy as the module temperature depends on many factors and can be installation-specific. More rigorous methods include factors for the array mounting arrangement and windspeed in an attempt to address this issue [53].

The directly measured module temperatures have been used here to model I_{SC}, V_{OC} and electrical energy yields for the four modules, using the equations (5.4). The energy yield has been calculated as the product of modelled P_{MPP} and the measurement interval. Results are presented on a monthly basis, relative to the measured values of each parameter, in Figure 5.6.

[†] NOCT Conditions: Irradiance 800 Wm^{-2}, AM1.5G Spectrum, ambient temperature 20ºC, windspeed > 1ms^{-1}

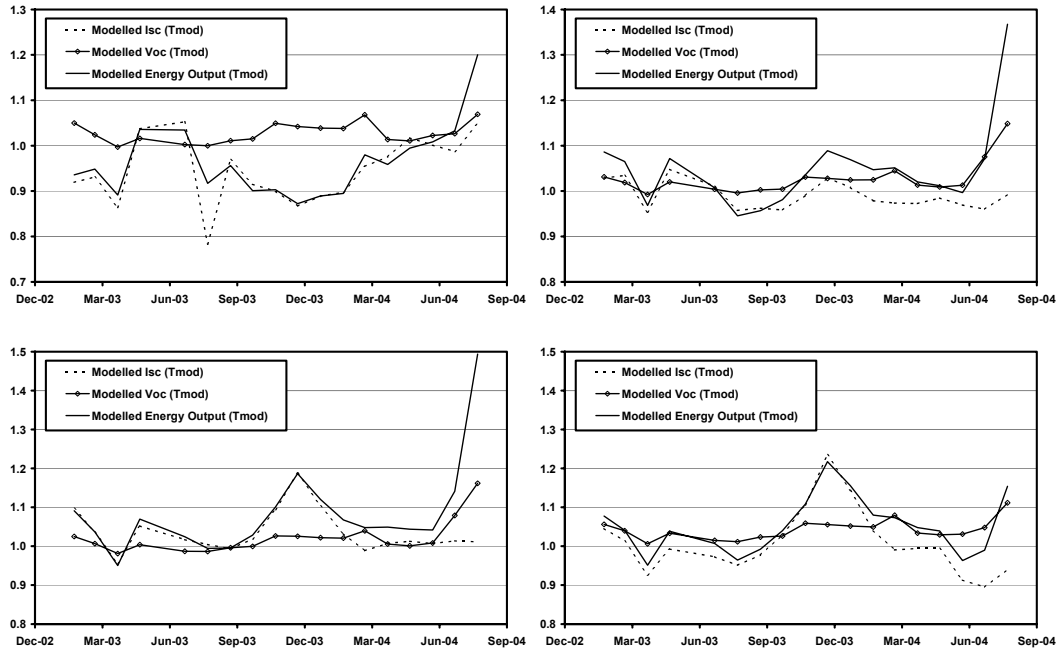

Figure 5.6: Results of modelling I_{SC}, V_{OC} and energy yield from empirical models of irradiance and module temperature (top-left to bottom-right: c-Si, a-Si, a-Si 2j, a-Si 3j)

With the exception of the last two months (which suggest some developing problem with the measurement system), the models produce remarkably good results considering their simplicity. Furthermore, the temperature coefficients used were those supplied by the manufacturer for the type of module and were not measured specifically for the devices tested.

The V_{OC} values are generally within 5% of measurement, although this includes over-estimation occurring during the winter months. This may be due to the setup of measuring the temperature on the back surface of the modules, which could be losing heat rapidly at these times.

Error on I_{SC} and P_{MPP} values are in the region of ±10%, rising a little in deep winter for the multi-junction devices. Modelling of both of these parameters relies heavily on irradiance measurements, whose accuracy is in the 5-10% range down to 100 Wm^{-2}. Although the measurement error does increase as the light level falls and so might explain the increased winter error in the modelling results, the trend is reversed in the case of the c-Si module. Given the findings of chapter 3, it is thus believed that the majority of the error in Figure 5.6 is caused by unaccounted-for spectral effects.

5.2.2 Extension to Spectral Effect

The inclusion of spectral effects into equations of the form used above has not been adopted previously for two main reasons. Firstly, measurements of solar spectral irradiance are not available in enough locations to make such an approach viable, except through spectral modelling. Secondly, parameterisation of the spectrum has never been made simple enough to use in this way, instead always incorporating PV device-specific information.

Using the Average Photon Energy defined in chapter 2 as an indicator of spectral blueness, it should now be possible to include spectral effects in these empirical device models, firstly with measured spectra from the CREST system and ultimately in general use with spectral irradiance models such as SMARTS and ASPIRE.

The simple approach taken in chapter 3 for assessing the spectral effect on power production is expanded as follows. Only I_{SC} and I_{MPP} are subject to the additional spectral modelling, since these are the parameters previously identified as having a significant dependence on the spectrum. I_{MPP} is treated in the same way as I_{SC}, since the differences between them are largely caused by the parasitic resistances and they demonstrate near-perfect linearity for the four devices examined here (a-Si 2j is shown for example in Figure 5.7).

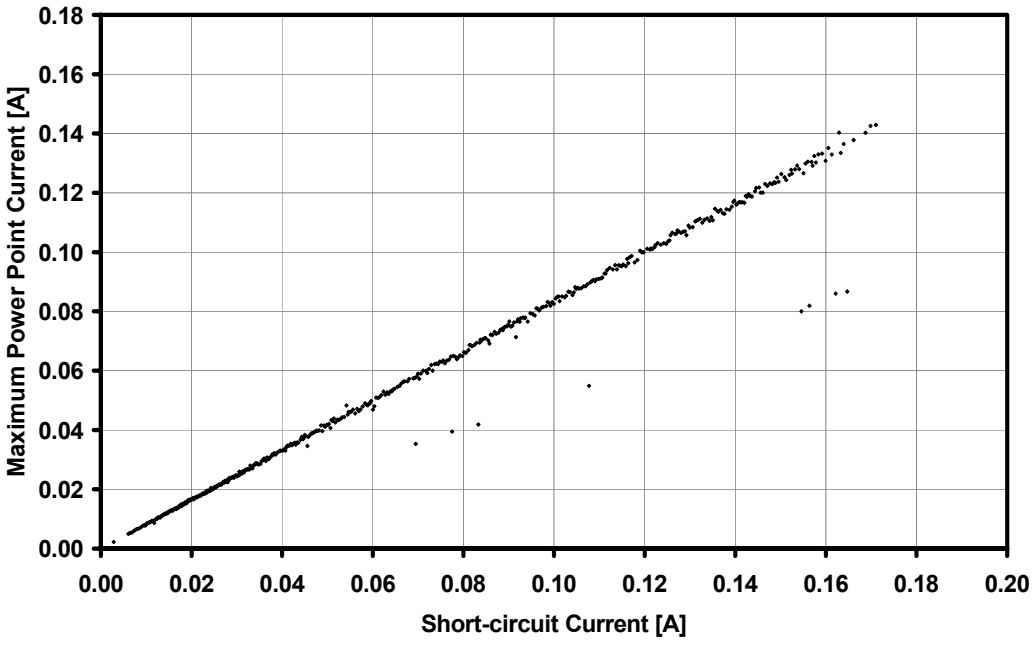

Figure 5.7: Linearity of I_{SC} and I_{MPP} (a-Si 2j)

I_{SC}/G and I_{MPP}/G are first corrected for temperature by rearranging the current equation in (5.4). As seen in chapter 3, the relation between these quantities and the spectrum APE is not linear. It is a combination of the matching between the device spectral response and the incident spectrum and the way that the APE itself varies with the spectrum. For the modules investigated, a third-order polynomial was sufficient to represent the variation of current response with APE:

$$\frac{\frac{I_{SC}}{G} - \alpha_{ISC}\left(T_{MOD} - T_{MOD}\big|_{STC}\right)}{\left[\frac{I_{SC}\big|_{STC}}{G\big|_{STC}}\right]} = a_0 + a_1 APE + a_2 APE^2 + a_3 APE^3 \tag{5.6}$$

Because of the normalisation by STC values on the left of equation (5.6) and the linearity displayed in Figure 5.7, the same coefficients were applied in the case of I_{MPP} also.

Thus V_{OC} and V_{MPP} are modelled as before (temperature-adjusted STC values) and I_{SC} and I_{MPP} are modelled as temperature- and spectrum-adjusted STC values, with P_{MPP} calculated from the adjusted I_{MPP} and V_{MPP} values. The results for the four modules are shown in Figure 5.8.

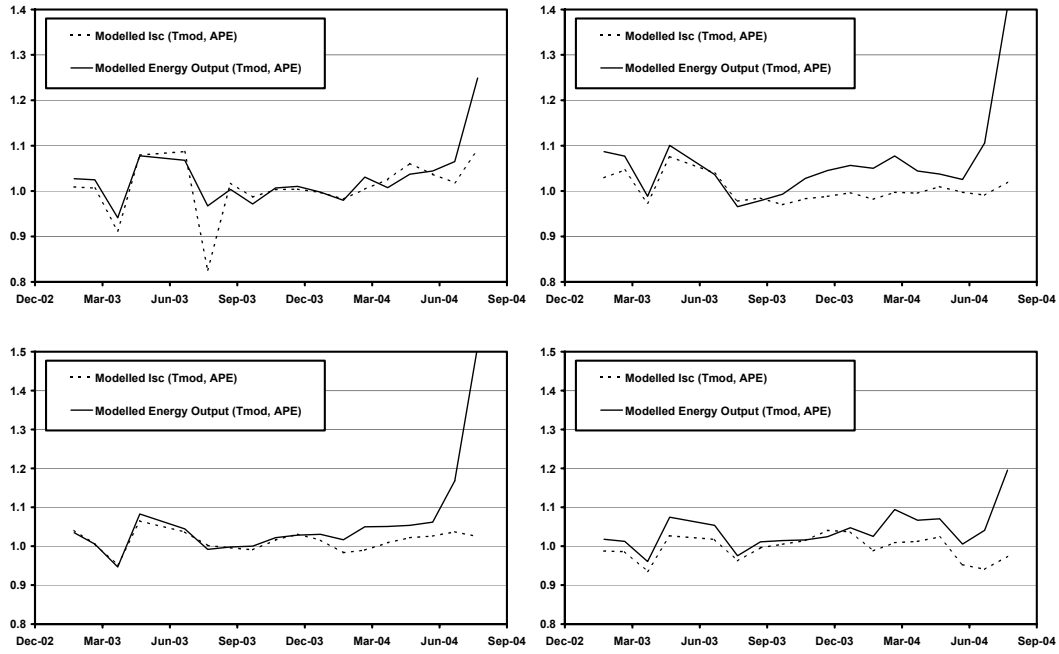

Figure 5.8: Modelling I_{SC}, V_{OC} and energy yield from empirical models of irradiance, module temperature and average photon energy (top-left to bottom-right: c-Si, a-Si, a-Si 2j, a-Si 3j)

The voltage has not been plotted, as the model is the same as that used in the previous section. The results for I_{SC} and energy yield (again from P_{MPP}) show some improvement over the temperature-only model. The increased winter error of the temperature model is completely removed by the addition of spectral information. The modelled short-circuit current is now within 5% of the measured value, with the exception of times associated with known thermopile measurement problems (notably summer 2003).

The energy yield calculation exhibits a larger error than the current (apparent in summer 2004 also). Given the good results for V_{OC}, V_{MPP} and I_{SC} and the timing of the error, it is possible that I_{MPP} is being reduced under high irradiance. This is compatible with irradiance effects on the parasitic resistances discussed in chapter 3, but not modelled here. Despite this, the error on the energy yield results is reduced overall by the order of 5% with the addition of spectral effects to the standard empirical model.

5.2.3 Parameterised Spectral Modelling

Having described the irradiance spectrum with the APE still leaves the problem of how to obtain this measure. Assessment of spectral irradiance models in chapter 4 shows this is one option, but having determined the cloud correction as a function of airmass and

atmospheric clearness, an investigation was made into the possibility of extrapolating this idea to the whole spectrum, through the APE. This would deliver a simpler method than total spectral modelling, with even fewer requirements regarding input data and may provide a useful rule-of-thumb tool for PV system installers.

The largest effects on the spectrum were previously found to be the airmass (AM) and clearness, the latter described with an AM-independent clearness index (k_T*). On this basis, an assessment was made to determine if there is a discernible, reliable relationship between the APE and these two parameters.

One year of concurrent irradiance and spectral data were extracted from the CREST database and the AM, k_T* and APE values calculated. The APE data was then averaged into bins of AM (width 0.5) and k_T* (width 0.1) as shown in Figure 5.9.

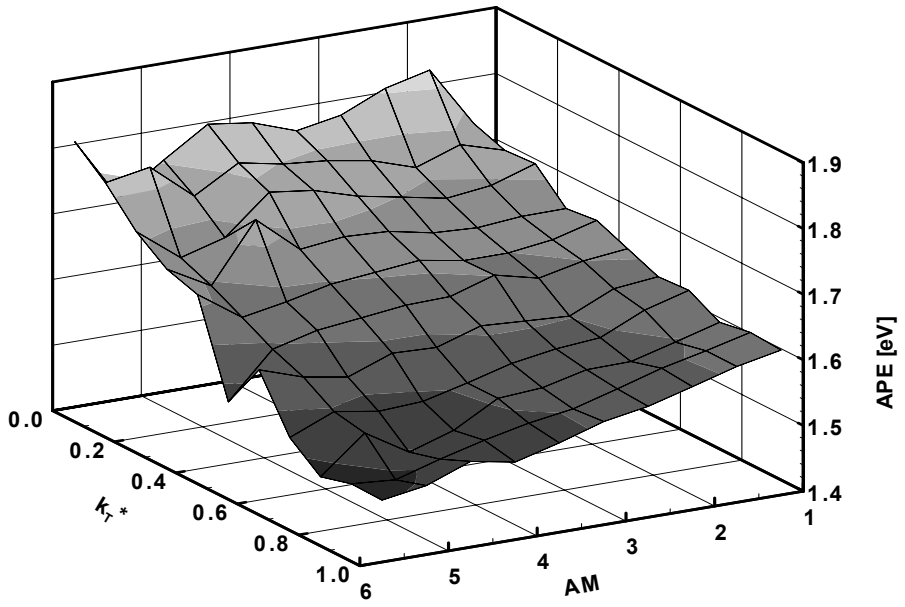

Figure 5.9: Measurements of the spectrum average photon energy binned by airmass and clearness index

The trends evident in the figure indeed show a similarity with those of the spectral cloud modifier of chapter 4. The roughly linear dependence of APE on airmass and slightly more sensitive relation to clearness is represented by the following simple parametric formula:

$$APE\left(AM, k_T^*\right) = a_0 + a_1 k_T^* + a_2 {k_T^*}^2 + AM \times \left(b_0 + b_1 k_T^* + b_2 {k_T^*}^2 \right) \quad (5.7)$$

Fitting the surface of Figure 5.9 yields the following values for the coefficients of equation (5.7), shown in
Table 5.1 and graphically in Figure 5.10:

a_0	1.719	b_0	-0.007
a_1	-0.116	b_1	-0.064
a_2	0.053	b_2	0.037

Table 5.1: Coefficients for APE model of airmass and clearness index

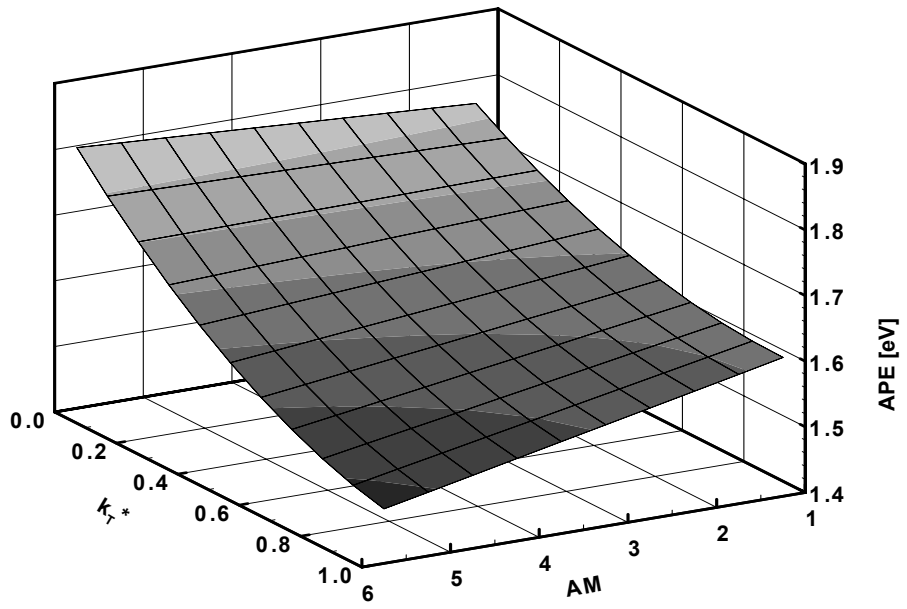

Figure 5.10: Average photon energy modelled as a function of airmass and clearness

Finally, values of APE modelled with equation (5.7) are substituted for those extracted from spectral irradiance measurement, in the procedure of section 5.2.2. The I_{SC} and energy yields thus modelled for the four modules are shown in Figure 5.11.

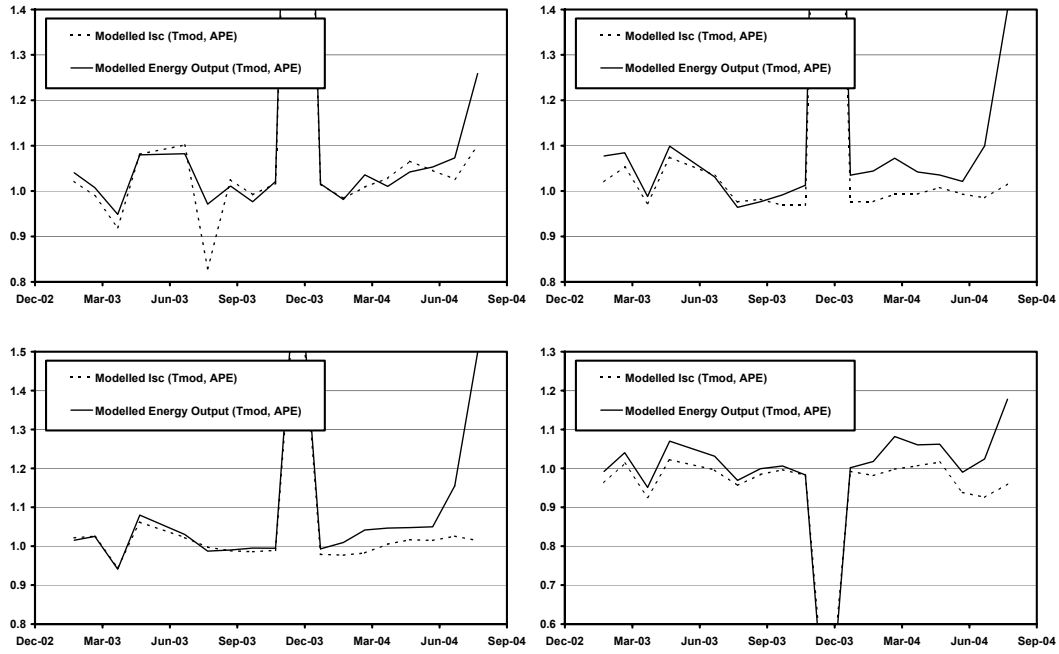

Figure 5.11: Modelling I_{SC}, V_{OC} and energy yield from empirical models of irradiance, module temperature and where APE (top-left to bottom-right: c-Si, a-Si, a-Si 2j, a-Si 3j)

Aside from the month of December 2003, the modelling results show only slightly increased errors compared to the spectral model with measured APE values. This slight increase however, is enough to make the approach of marginal benefit over the temperature-only model.

It is believed the main problems lie in an extra reliance on the irradiance measurements (used to calculate k_T*) and poor performance of the empirical APE model in the extremes of its underlying parameters. The device model then becomes unstable at low irradiances, due to increased error in the irradiance measurement and at high airmass, due to the approximate fitting of the APE surface of Figure 5.9. Where such conditions coincide, the error becomes unacceptable.

5.3 Conclusions

It has been demonstrated that one can model the short-circuit current of multi-junction a-Si devices from the product of spectral response and measured spectrum to a similar accuracy as for single-junction devices, provided spectral response data for each sub-cell is available.

The accuracy for all types of device is limited by a general lack of information of how the spectral response of a device changes with the operating environment (where temperature is thought to be the largest influence). This is the key knowledge gap to be closed, not only to allow modelling of such effects, but to fully separate the effects of temperature and spectrum on devices. This is a requirement to make further progress in modelling PV devices in realistic operation.

In the interim, the empirical methods currently in most widespread use for system modelling have been shown to benefit from the inclusion of a fitted dependence on the average photon energy. When extracted from spectral irradiance measurements, such a modification yields a reduction in error in both I_{SC} and power of ~5% absolute.

It is unrealistic to expect measured spectra to be widely available, which means the APE values for device modelling will need to be modelled themselves if such an approach is to be implemented generally. The ASPIRE all-sky spectral model has proved sufficiently accurate on the monthly timescale to meet this need, but may be too unwieldy from the installer perspective. Instead a rule-of-thumb method, itself empirical, has been suggested, requiring only site irradiance measurements. The concept of this method appears to be sound, but requires development to reap benefits over existing methods. It was also found that high quality measurements are essential for this process and to maintain model stability.

6 Thesis Conclusions

6.1 Outdoor Measurement Techniques

The outdoor measurement system at CREST has continued to evolve during the course of this work and represents a good standard in PV monitoring stations. The inclusion of spectral irradiance measurements adds a valuable resource for the research community and is presently matched by only one other system in the world, which has a narrower spectral response.

The limitations of the system have been considered in the use of the data and suggestions made for improvements. The priorities have been identified as further improvement to the accuracy of irradiance measurement under low light conditions and reduction in the time taken to measure spectra. As this thesis nears completion, both of these issues are being addressed in a new upgrade round for the CREST system.

6.2 Spectral Characterisation

The problems associated with simple characterisation of spectral irradiance for application to PV research have been discussed. A solution has been proposed through the use of the device-independent parameter of Average Photon Energy. This has allowed a single-number description of the spectrum to be used to discuss the spectral irradiance resource and its effect on PV devices.

Some limitations to the parameter have been identified also. It was found that the APE does not always uniquely describe spectral conditions, due to the different manner in which the spectrum changes in clear-sky and cloudy conditions. A better descriptor may be found to deal with this issue, but it is likely to cost practicality in deployment. An alternative solution has been found to consider these two conditions separately. Relatively simple methods have been shown to reliably split the dataset into clear and cloudy sub sets and within each of these, the APE measure appears unique for a given spectral distribution.

6.3 Spectral Irradiance Environment of the UK

Spectral irradiance conditions have been fully analysed for the UK midlands. The primary influences on the spectrum have been confirmed as airmass variation and cloud amount. Weaker variation due to measurement plane orientation has also been observed.

The CREST measurements show a significant seasonal variation due to the site latitude (affecting annual airmass variation) and maritime climate (containing considerably more water vapour and oceanic aerosols than the reference atmospheres used in the spectral standards for PV). A clear seasonal pattern extending from winter APE lows of 1.52 eV to summer highs of 1.66 eV is observed.

A comparison was made with the only other long-term spectral dataset, from NREL in the USA. This is a site with a slightly lower latitude and a very different climate to Loughborough. A significant difference was found between the spectral environments of each site, posing questions about the applicability of a single spectral standard.

6.4 Spectral Effects on Photovoltaic Devices

The first detailed investigation of the effects of spectral irradiance variation on the performance of PV devices using measured spectral data has been performed. This has focused on four modules of different materials and structures and considered the interaction of other environmental factors.

The main problem associated with the investigation of environmental effects on PV device performance in real operating conditions has been found to be the difficulty of their separation. Filtering the data to isolate different influences is not an option for analysis of outdoor data because of the strong correlation between the various drivers. By careful appraisal of all the influences on each electrical parameter, it was possible to present a case of evidence by viewing the data along different axes.

Assessment of the effects thus revealed minimal effect of angle of incidence on seasonal energy production for the CREST system and apparently significant irradiance effects at low light levels (although accurate quantification in this region is beyond the system limits).

Temperature effects were found to contribute a 2% summer enhancement of energy yield and a winter loss of 0-1% for all the module types tested.

Spectral effects vary considerably between PV technologies and seasons. Multi-junction devices were found to be the most sensitive to spectral variation, suffering energy yield losses of 18% from this cause in midwinter, compared to 7% for the single-junction a-Si device. The c-Si module exhibited a winter *gain* of 7%. Investigation of this apparent anomaly showed an even higher sensitivity of spectral influence to the detail of the spectral response than was anticipated and this value in fact seems plausible. All a-Si modules benefit from the spectral effect in summer, gaining 1-5% on the energy yields.

Within measurement accuracy, no direct influence of the spectrum on device parameters other than the short-circuit current was observed for the modules tested. There is an indirect influence on the open-circuit voltage, due to absolute change in I_{SC}. Other modules, not exhibiting the strong linearity of maximum power point current and I_{SC} seen in those in this study, may display further effects on the maximum power.

A route towards more definitive quantification of the various influences on device efficiency will combine carefully controlled indoor measurements to characterise modules with modelling approaches to separate the effects seen in the outdoor data.

6.5 Spectral modelling

The key challenges in spectral irradiance modelling have been identified, as well as those areas that may be considered only of secondary importance. For clear skies, it was found that air pressure and aerosol sub models have little influence on the spectral distribution and may be estimated without detriment to the overall modelling results.

Whilst critically important, it was found that airmass and water vapour influences are dealt with sufficiently well in existing approaches. The main concern is aerosol turbidity. Measurements of this quantity are indirect and require equipment that is non-standard as far as national meteorological networks are concerned and is also not available at CREST.

This shortcoming is compensated for by the empirical nature of the cloud cover modification made in the all-sky spectral irradiance model (ASPIRE) developed here. However, this may reduce the portability of the final model, which is yet to be tested.

Nonetheless, validation of ASPIRE against an independent set of spectral irradiance measurements from CREST has demonstrated a significant improvement over application of clear-sky spectral models. On a monthly basis, the worst case is still a halving of the error from these existing models. For much of the year, the error is within 0.01 eV and it is strongly believed that poorer winter performance will be improved with more accurate low light irradiance measurements.

6.6 Device modelling

An empirical method commonly used to correct for temperature effects has been extended to include the influence of the spectrum, using concurrent device and spectral irradiance measurements at CREST. This has been proven by reducing the monthly errors in I_{SC}, V_{OC} and energy yield from 10% with the temperature-only model, to 5% with the spectral addition, for the modules investigated.

An estimation method for the APE values required for this empirical approach has been suggested. Such an approach requires higher-quality measurements than are currently available, but offers a potential simplification to the alternative of full spectral irradiance modelling, which may be more palatable for widespread implementation.

A second device model, based on combining spectral response curves with measured or modelled spectra has been assessed with an extension to multi-junction devices. The validation of this model has shown an accuracy on a par with that of the empirical temperature model. It is thought that such an approach would prove more accurate (and physically meaningful) than the empirical modelling, if certain key issues are addressed.

These issues regard the spectral response curves used in the modelling. It was found in the earlier analysis of the spectral effect on the c-Si module, that the device behaviour is highly sensitive to the spectral response curve. The SR curves used in this modelling approach were from different devices in the case of the single-junction devices. For the multi-junctions, it is not known how representative the curves used are.

While it is thought the SR changes with a number of environmental and degradational influences, there has not yet been a thorough investigation of the sensitivity of the SR to such drivers. While the work of this thesis has contributed to the understanding of the spectral irradiance resource and the impact on photovoltaic devices, future research progress and more accurate models for performance analysis and energy yield prediction will require this detailed information on device spectral response. It is thus a recommendation arising from this work that research on spectral effects be concentrated in this area.

List of Publications and Presentations Arising Through This Work

Al-Buflasa, H., T. R. Betts, et al. (2004). Modelling the Effect of Spectral Variations on the Performance of Amorphous Silicon Solar Cells. Proceedings of the 19th Photovoltaic Solar Energy Conference, Paris.

Betts, T. R., R. Gottschalg, et al. (2001). Progress Towards Modelling Solar Spectral Radiation for Optimisation of Amorphous Silicon Photovoltaic Systems. REMIC 2001. Belfast May 2001., Oxford, UK-ISES.

Betts, T. R., R. Gottschalg, et al. (2002). Modelling Spectral Irradiation Effects of Single- and Multi-Junction Amorphous Silicon Photovoltaic Devices. Proceedings of the 29th IEEE Photovoltaic Specialists Conference, New York, IEEE.

Betts, T. R., R. Gottschalg, et al. (2003). Aspire - A Tool to Investigate Spectral Effects on PV Device Performance. Proceedings of the 3rd World Conference on Photovoltaic Energy Conversion, Osaka.

Betts, T. R., R. Gottschalg, et al. (2003). Aspire - All-Sky Spectral Irradiance Modelling for Photovoltaic Applications. Photovoltaic Science, Application and Technology, Oxford, UK-ISES.

Betts, T. R., R. Gottschalg, et al. (2004). Spectral Irradiance Correction for PV System Yield Calculations. Proceedings of the 19th Photovoltaic Solar Energy Conference, Paris.

Betts, T. R., C. Jardine, et al. (2004). "Spectral Dependence of Amorphous Silicon Photovoltaic Device Performance." Journal of Ambient Energy **25**(1): 26-32.

Betts, T. R., C. N. Jardine, et al. (2003). Impact of Spectral Effects on the Electrical Parameters of Multijunction Amorphous Silicon Cells. Proceedings of the 3rd World Conference on Photovoltaic Energy Conversion, Osaka.

Betts, T. R., C. N. Jardine, et al. (2003). Spectral Dependence of Amorphous Silicon Photovoltaic Device Performance. Photovoltaic Science, Application and Technology, Loughborough, Oxford, UK-ISES.

Beyer, H. G., R. Gottschalg, et al. (2003). Modellierung der Abhaengigkeit des Kurzschlusstromes und der MPP-Leistung von a-Si Modulen von der meteorologischen Situation. Proceedings of the 18th Symposium Photovoltaische Solarenergie, Staffelstein, OTTI.

Ekins-Daukes, N. J., Y. Kemmoku, et al. (2003). The Design Specification for a Multi-Junction Concentrator System Computer Model. Super High-Efficiency Research Center Meeting, Nagoya.

Ekins-Daukes, N. J., Y. Kemmoku, et al. (2003). The Design Specifications for Syracuse: A Multi-Junction Concentrator System Computer Model. Workshop for High-Efficiency Solar Cells & Systems, Kyoto.

Ekins-Daukes, N. J., Y. Kemmoku, et al. (2004). The Design Specifications for Syracuse; A Multi-Junction Concentrator System Computer Model. Proceedings of the 19th Photovoltaic Solar Energy Conference, Paris.

Gottschalg, R., T. R. Betts, et al. (2002). Experimental Investigation of Spectral Effects on Amorphous Silicon Devices in Outdoor Operation. Proceedings of the 29th IEEE Photovoltaic Specialists Conference, New York, IEEE.

Gottschalg, R., T. R. Betts, et al. (2003). Modelling the Performance of Amorphous Silicon Devices in the UK. Photovoltaic Science, Application and Technology, Oxford, UK-ISES.

Gottschalg, R., T. R. Betts, et al. (2004). "The Effect of Spectral Variations on the Performance Parameters of Single and Double Junction Amorphous Silicon Solar Cells." Solar Energy Materials and Solar Cells: in press.

Gottschalg, R., T. R. Betts, et al. (2004). "On the Importance of Considering the Incident Spectrum When Measuring the Outdoor Performance of Amorphous Silicon Photovoltaic Devices." Measurement Science and Technology **15**(2): 460-466.

Gottschalg, R., T. R. Betts, et al. (2004). "Energy Production of Amorphous Silicon Devices in a Maritime Climate - Technological and Physical Issues." Solar Energy: in press (invited paper).

Gottschalg, R., H.-G. Beyer, et al. (2003). Modelling the Realistic Short Circuit Current and MPP of A-Si Single and Multi-junction Devices. Proceedings of the 3rd World Conference on Photovoltaic Energy Conversion, Osaka, NN.

Gottschalg, R., J. A. del Cueto, et al. (2003). Investigating the Seasonal Performance of A-Si Single- and Multi-junction Modules. Proceedings of the 3rd World Conference on Photovoltaic Energy Conversion, Osaka.

Gottschalg, R., C. N. Jardine, et al. (2002). Performance of Amorphous Silicon Double Junction Photovoltaic Systems in Different Climatic Zones. Proceedings of the 29th IEEE Photovoltaic Specialists Conference, New York, IEEE.

Gottschalg, R., R. Rüther et al. (2001). Environmental Effects on the Performance of an Amorphous Silicon PV System. 17th European Photovoltaic Solar Energy Conference, Munich, M Mchen.

Jardine, C. N., R. Gottschalg, et al. (2002). Influence of Spectral Effects on the Performance of Multijunction Amorphous Silicon Cells. Proceedings Photovoltaic in Europe Conference, WIP.

Sabry, M., R. Gottschalg, et al. (2002). Optical Filtering of Solar Radiation to Increase Performance of Concentrator Systems. Proceedings of the 29th IEEE Photovoltaic Specialists Conference, Louisianna, New York, IEEE.

Sauter, D., T. R. Betts, et al. (2004). Performance of Amorphous Silicon Modules. Proceedings of the 19th Photovoltaic Solar Energy Conference, Paris.

Williams, S. R., T. R. Betts, et al. (2004). Modelling Real Annual Module Performance with Consideration to Spectral and Incidence Angle Effects. Proceedings of the 19th Photovoltaic Solar Energy Conference, Paris.

Williams, S. R., T. R. Betts, et al. (2003). Modelling Long-Term Module Performance Based On Realistic Reporting Conditions With Consideration to Spectral Effects. Proceedings of the 3rd World Conference on Photovoltaic Energy Conversion, Osaka.

References

[1] R. Gottschalg, D.G. Infield, and M.J. Kearney, Spectral Effects on the Performance of Thin Film Solar Cells at Loughborough, UK. Silver Jubilee conference: towards a renewable future; Conference C73 of the Solar Energy Society, Quality Hotel Brighton, 13-15 May 1999, (1999) 35.

[2] K. Boucher, http://www.lboro.ac.uk/departments/gy/climate/info.html, (2004)

[3] C.R. Osterwald, Calculated solar cell Isc sensitivity to atmospheric conditions under direct and global irradiance. Eighteenth IEEE Photovoltaic Specialists Conference, (1985) 951.

[4] D. Berman, D. Faiman, and B. Farhi, Sinusoidal spectral correction for high precision outdoor module characterization, Solar Energy Materials and Solar Cells 58 (1999) 253.

[5] Y. Hirata and T. Tani, Output variation of photovoltaic modules with environmental factors - I. The effect of spectral solar radiation on photovoltaic module output, Solar Energy 55 (1995) 463.

[6] C.R. Osterwald, et al., Extending the Spectral Range of Silicon-Based Direct-Beam Solar Spectral Radiometric Measurements, Conference Record of the Twentieth IEEE Photovoltaic Specialists Conference, (1988) 1246.

[7] J. Merten and J. Andreu, Clear separation of seasonal effects on the performance of amorphous silicon solar modules by outdoor I/V-measurements, Solar Energy Materials and Solar Cells 52 (1998) 11.

[8] R. Perez, et al., Modeling Daylight Availability and Irradiance Components from Direct and Global Irradiance, Solar Energy 44 (1990) 271.

[9] R. Ruther and J. Livingstone, Seasonal-Variations in Amorphous-Silicon Solar Module Outputs and Thin-Film Characteristics, Solar Energy Materials and Solar Cells 36 (1994) 29.

[10] P. Faine, et al., The Influence of Spectral Solar Irradiance Variations on the Performance of Selected Single-Junction and Multijunction Solar-Cells, Solar Cells 31 (1991) 259.

[11] A. Raicu, et al., Annual and Seasonal Energy Rating of Mono-Si, a-Si and Gaas Test Cells for the USA by the Rrc Method. Conference Record of the Twenty Second Iee Photovoltaic Specialists Conference - 1991, Vols 1 and 2, (1991) 744.

[12] K. Heidler, A. Raicu, and H.R. Wilson, A New Approach for the Performance Evaluation of Solar-Cells under Realistic Reporting Conditions, Conference Record of the Twenty First IEEE Photovoltaic Specialists Conference - 1990, Vols 1 and 2, (1990) 1017.

[13] H.R. Wilson and M. Hennies, Energetic Relevance of Solar Spectral Variation on Solar-Cell Short-Circuit Current, Solar Energy 42 (1989) 273.

[14] G. Kleiss, A. Raicu, and K. Bucher, Temperature-Dependent Influence of a-Si-H Cell Degradation on the Energy Delivered under Realistic Reporting Conditions, Conference Record of the Twenty Third IEEE Photovoltaic Specialists Conference - 1993, (1993) 896.

[15] K. Bucher, Site dependence of the energy collection of PV modules, Solar Energy Materials and Solar Cells 47 (1997) 85.

[16] S. Nann and K. Emery, Spectral Effects on PV-Device Rating, Solar Energy Materials and Solar Cells 27 (1992) 189.

[17] A. Parretta, A. Sarno, and L.R.M. Vicari, Effects of solar irradiation conditions on the outdoor performance of photovoltaic modules, Optics Communications 153 (1998) 153.

[18] D.L. King and P.E. Eckert, Characterizing (rating) the performance of large photovoltaic arrays for all operating conditions, Conference Record of the Twenty Fifth IEEE Photovoltaic Specialists Conference, (1996) 1385.

[19] I.E. Commission, 61853N Performance Testing and Energy Rating of Terrestrial Photovoltaic (PV) Modules - Working Draft, (2004)

[20] S.J. Ransome and J.H. Wohlgemuth, Predicting kWh/kWp performance for amorphous silicon thin film modules, Conference Record of the Twenty-Eighth IEEE Photovoltaic Specialists Conference - 2000, (2000) 1505.

[21] J.A. Eikelboom and M.J. Jansen, Characterisation of PV Modules of New Generations: Results of tests and simulations, (2000)

[22] K. Akhmad, et al., Outdoor performance of amorphous silicon and polycrystalline silicon PV modules, Solar Energy Materials & Solar Cells 46 (1997) 209.

[23] R. Gottschalg, et al., On the importance of considering the incident spectrum when measuring the outdoor performance of amorphous silicon photovoltaic devices, Measurement Science & Technology 15 (2004) 460.

[24] B. Kroposki, et al., Comparison of module performance characterization methods, Conference Record of the Twenty-Eighth IEEE Photovoltaic Specialists Conference - 2000, (2000) 1407.

[25] J.A. del Cueto and B. von Roedern, Temperature-induced changes in the performance of amorphous silicon multi-junction modules in controlled light-soaking, Progress in Photovoltaics 7 (1999) 101.

[26] N. Martin and J.M. Ruiz, Calculation of the PV modules angular losses under field conditions by means of an analytical model, Solar Energy Materials and Solar Cells 70 (2001) 25.

[27] H. Field and K. Emery, An Uncertainty Analysis of the Spectral Correction Factor, Conference Record of the Twenty Third IEEE Photovoltaic Specialists Conference, (1993) 1180.

[28] D. Crommelynck and A. Joukoff, A Simple Algorithm for the Estimation of the Spectral Radiation Distribution on a Horizontal Surface, Based on Global Radiation Measurements, Solar Energy 45 (1990) 131.

[29] S.A. Clough, et al., Fast Atmospheric Transmittance and Radiance Algorithm - Fascode, Journal of the Optical Society of America 68 (1978) 1424.

[30] L.S. Rothman, Atmospheric Propagation of Radiation - Microwave through Visible, Onde Electrique 72 (1992) 39.

[31] R.G. Isaacs, et al., Multiple-Scattering Lowtran and Fascode Models, Applied Optics 26 (1987) 1272.

[32] R.E. Bird, Terrestrial Solar Spectral Modeling, Solar Cells 7 (1982) 107.

[33] P. Moon, Proposed Standard Solar Radiation Curves for Engineering Use, Journal of the Franklin Institute 230 (1940) 583.

[34] D.M. Gates, Spectral Distribution of Solar Radiation at the Earth's Surface, Science 151 (1966) 523.

[35] B. Leckner, Spectral Distribution Of Solar Radiation At The Earth's Surface-Elements Of A Model, Sol Energy 20 (1978) 143.

[36] J.L. Hatfield, R.B. Giorgis, and R.G. Flocchini, A Simple Solar-Radiation Model for Computing Direct and Diffuse Spectral Fluxes, Solar Energy 27 (1981) 323.

[37] D.T. Brine and M. Iqbal, Diffuse and Global Solar Spectral Irradiance under Cloudless Skies, Solar Energy 30 (1983) 447.

[38] C.G. Justus and M.V. Paris, A Model for Solar Spectral Irradiance and Radiance at the Bottom and Top of a Cloudless Atmosphere, Journal of Climate and Applied Meteorology 24 (1985) 193.

[39] R.E. Bird and C. Riordan, Simple Solar Spectral Model for Direct and Diffuse Irradiance on Horizontal and Tilted Planes at the Earths Surface for Cloudless Atmospheres, Journal of Climate and Applied Meteorology 25 (1986) 87.

[40] C.P. Jacovides, et al., Application of SPCTRAL2 parametric model in estimating spectral solar irradiances over polluted Athens atmosphere, Renewable Energy 29 (2004) 1109.

[41] M.P. Utrillas, et al., A comparative study of SPECTRAL2 and SMARTS2 parameterised models based on spectral irradiance measurements at Valencia, Spain, Solar Energy 63 (1998) 161.

[42] C.A. Gueymard, SMARTS2, A Simple Model of the Atmospheric Radiative Transfer of Sunshine: Algorithms and performance assessment, (1995)

[43] C.A. Gueymard, Parameterized transmittance model for direct beam and circumsolar spectral irradiance, Solar Energy 71 (2001) 325.

[44] C.A. Gueymard, D. Myers, and K. Emery, Proposed reference irradiance spectra for solar energy systems testing, Solar Energy 73 (2002) 443.

[45] J.S. Bartlett, et al., The spectral effects of clouds on solar irradiance, Journal of Geophysical Research-Oceans 103 (1998) 31017.

[46] S. Nann, A Cloud Cover Modifier for Solar Spectral Irradiance Modelling. Congress of the International Solar Energy Society, Vol. 1 (1989) 422.

[47] S. Nann and C. Riordan, Solar Spectral Irradiance under Clear and Cloudy Skies - Measurements and a Semiempirical Model, Journal of Applied Meteorology 30 (1991) 447.

[48] B.Y.H. Liu and R.C. Jordan, Daily Insolation on Surfaces Tilted Toward the Equator, ASHRAE Journal (1961) 53.

[49] W.H. Press, et al., Numerical Recipes in PASCAL: The Art of Scientific Computing. 1990: Cambridge University Press. 781.

[50] B. Marion, A method for modeling the current-voltage curve of a PV module for outdoor conditions, Progress in Photovoltaics 10 (2002) 205.

[51] H. Schade and Z.E. Smith, Optical-Properties and Quantum Efficiency of a-Si1-Xcx-H/a-Si-H Solar-Cells, Journal of Applied Physics 57 (1985) 568.

[52] M. Skiba, M. Mohr, and H. Unger, Comparative Assessment and Validation of Models Estimating Diffuse Irradiation on Inclined Planes. Internationales Sonnenforum; EuroSun '96, (1996) 1568.

[53] M.K. Fuentes, A Simplified Thermal Model for Flat-Plate Photovoltaic Arrays, (1987)